Progress Report
Teilinstitut Nukleare
Festkörperphysik
1.6.1977-31.5.1978

Editor: K. Käfer
Institut für Angewandte Kernphysik

Kernforschungszentrum Karlsruhe

KERNFORSCHUNGSZENTRUM KARLSRUHE

Institut für Angewandte Kernphysik

KfK 2670

PROGRESS REPORT

Teilinstitut Nukleare Festkörperphysik

June 1, 1977 - May 31, 1978

Editor: K. Käfer

Kernforschungszentrum Karlsruhe GmbH, Karlsruhe

Abstract

This Progress Report of the Teilinstitut Nukleare Festkörperphysik covers
the work done at the Institute during the period from June 1, 1977 to May 31, 1978.

The main research areas presently under investigation are underlined by the
arrangement of the report: structure and dynamics of solids, electronic
structure and magnetism of solids, and the development and investigation of novel
materials. Some technical developments important in carrying out this
research are included as well.

Zusammenfassung

Dieser Progress Report des Teilinstituts Nukleare Festkörperphysik er-
faßt den Zeitraum vom 1. Juni 1977 - 31. Mai 1978. Die Darstellung be-
tont die Hauptforschungsgebiete, auf denen das Institut zur Zeit tätig
ist. Diese sind: Struktur und Dynamik von Festkörpern und Flüssigkeiten,
Elektronenstruktur und Magnetismus von Festkörpern und die Entwicklung
und Untersuchung neuartiger Materialien. Einige technische Entwicklungen,
die für diese Forschungsarbeiten wichtig sind, wurden ebenfalls in den
Bericht aufgenommen.

E D I T O R I A L

This Progress Report of the Teilinstitut Nukleare Festkörperphysik covers the work done at the Institute during the period from June 1, 1977 to May 31, 1978.

The main research areas presently under investigation are underlined by the arrangement of the report: structure and dynamics of solids, electronic structure and magnetism of solids, and the development and investigation of novel materials. Some technical developments important in carrying out this research are included as well.

Work submitted for publication or already published is accounted for in a short version or as an abstract. First results of current investigations are described more extensively. Neutron scattering work by guest groups, not related to the research area of this Institute, has not been included in the report. An account of it will be given in a separate report to be published soon (Kernforschungszentrum Karlsruhe GmbH, KfK 2719).

The report is supplemented by a list of the Institute's staff members, their publications in the period of reporting, and a list of the neutron spectrometers available in the research reactor FR2.

As a technical note we should mention that on January 1, 1978, the former name of "Gesellschaft für Kernforschung mbH" was changed into "Kernforschungszentrum Karlsruhe GmbH".

Finally, we would like to thank H. John † and J. Steigleder for their technical assistance in preparing this report.

P R E F A C E

The Teilinstitut Nukleare Festkörperphysik of the Institut für Ange-
wandte Kernphysik (IAK I) developed from the use of nuclear methods in
solid state research. Its special methods are elastic and inelastic neu-
tron scattering, Mössbauer-spectroscopy, and irradiation of solids with
ions from a 3 MV Van de Graaff accelerator. With the development of its
research program toward specific problems in solid state research, the
institute has supplemented its experimental equipment with facilities for
ion implantations, thin film preparation by sputtering and evaporation,
back-scattering and channeling, magnetization- and T_c-measurements, crystal
growing, X-ray diffraction, and dI/dU tunneling. This tendency toward non-
nuclear methods will get additional enhancement in the coming years, because
the Karlsruhe research reactor (FR2) will not be operated beyond 1981. Pre-
parations are in progress to transfer the most modern instruments now installed
at the FR2 to the French reactors Orphée in Saclay and Siloé and Mélusine at
Grenoble, which will allow continuation of part of the neutron scattering
activity. In addition, experimental facilities for electron spectroscopy,
X-ray studies on disordered crystals, and preparation of materials, especially
single crystals, will be built up in Karlsruhe. The Institute also plans to
transfer the ion implantation facility together with a 2 MV accelerator not
used at the moment to a new experimental hall near the 3 MV accelerator, which
allows irradiation with all three accelerators in common target stations.

The Institute has now (October 1978) 23 scientists as professional staff.
The fluctuating number of guest scientists, graduate and Ph.D. students is
about 12. The theoretical support was extended this year by an increase in the
theoretical staff to five scientists. IAK I shares with its sister institute
IAK II (Teilinstitut Kernphysik) a common infrastructure consisting of a
mechanical and an electronic workshop, a maintenance group for the 3 MV
accelerator, and a group responsible for experimental computers and data
processing. Development activitites of the latter two groups are included
in this progress report. For the experimental computers of the whole Institute
great emphasis is put on a unified modular system both in software and hardware.

In the Research & Development Program and in the Annual Report of the
Nuclear Research Center as a whole, the research program of IAK I is subdivided
into the following three topics (titles for 1979):

Keeping the tradition of this progress report, the list of contents
differs from the listing above by an extra chapter for Theory and the listing
of activities in Ion Implantation and Channeling together with those in
materials development under the common title Materials Research. There are
also the extra chapters Data Processing and Development of Measuring Devices
and Techniques.

The main effort of the IAK I research is concentrated on high T_c super-
conducting materials. This includes band structure calculations and theoretical
investigations in lattice dynamics and electron-phonon-coupling. Experimental
work is done in inelastic neutron scattering for the determination of phonon
dispersion and density of states, in preparation of bulk samples and (mostly
metastable) superconducting films or layers by sputtering, evaporation and ion
implantation, and in investigations of superconducting materials by backscatter-
ing, channeling, X-ray diffraction, and other methods mentioned in this report.

In the chapter Dynamics and Structure of Solids and Liquids the reader may
see some heterogeneity in research topics concerning the work in non-super-
conductors. This is due in part to the engaged collaboration of the IAK I staff
with external research groups from universities and other institutions. Another
reason is the interest in various research topics which are related to the
know-how of the Institute and might be extended in future. Investigations in
this direction are for example the studies on superionic conductors and the
characterization of steel samples by neutron diffraction.

The investigations under the heading Electronic Structure and Magnet-
ism are concentrated on alloys of transition and rare-earth metals which allow
Mößbauer-spectroscopy with ^{61}Ni, ^{155}Gd, and ^{151}Eu. This work aims at a better
understanding of local moment formation and magnetic coupling in metals. An
essential basis for part of it is the supply of short-living ^{61}Ni Mößbauer
sources from the Karlsruhe cyclotron. Magnetic neutron scattering is performed
after completion of the work above or in collaboration with external users of
the FR2.

W. Schmatz

C O N T E N T S

1. I N V E S T I G A T I O N S   O N   T H E   D Y N A-M I C S   O F   S O L I D S   A N D   L I Q U I D S

2. T H E O R Y

3.   E L E C T R O N I C   S T R U C T U R E   A N D
      M A G N E T I S M   O F   S O L I D S

5. DATA PROCESSING

6. DEVELOPMENT OF MEASURING DEVICES AND TECHNIQUES

1. INVESTIGATIONS ON THE DYNAMICS AND STRUCTURE OF SOLIDS AND LIQUIDS

1.1 Phonon Anomalies in LaS

W. Reichardt, P. Roedhammer[a], and F. Holtzberg[b]

[a]Fachbereich Physik, Universität Konstanz, D-7750 Konstanz

[b]IBM Thomas J. Watson Research Center, Yorktown Heights, New York 10598 U.S.A.

Like its homologue YS the monosulfide of La is metallic and superconducting and crystallizes in the B1 structure. The superconducting transition temperature T_c of 0.84 K reported in the literature /1/ is considerably lower than in YS (T_c = 2.8 K). Therefore it was expected that the pronounced phonon anomalies found in the LA branches of YS /2/ are considerably reduced for LaS.

Measurements of the phonon dispersion curves of LaS at 296 K were performed on the triple-axis-spectrometer TAS1 at the FR2. The sample consisted of four coaligned single crystals yielding a total volume of $\sim$ 0.6 cm^3.

The figure shows the experimental results in the three main symmetry directions. The dispersion curves of LaS resemble closely those of YS. In particular a similar - only slightly reduced - softening of the LA phonons occurs in certain regions of the Brillouin zone whereas the TA branches exhibit no anomalies. Furthermore a strong anisotropy in the elastic region is observed. We have measured only few optical phonons in order to determine the position of the optical band for model calculations. From analogy to YS we expect the optical branches of LaS to be rather flat.

The curves in the figure were calculated from an 11 parameter double shell model fitted to the experimental data. The model parameters are very similar to those of YS.

Considering the rather low T_c of LaS quoted above, the strength of the phonon anomalies in the LA branches is surprisingly large. It is well known that in the related refractory carbides and nitrides T_c depends strongly on the non-metal concentration /3/. A similar behaviour may also be found in LaS. Therefore further discussions about correlations between the magnitude of T_c and the sizes of the phonon anomalies in the transition metal chalcogenides have to be postponed until we have measured the T_c of our sample.
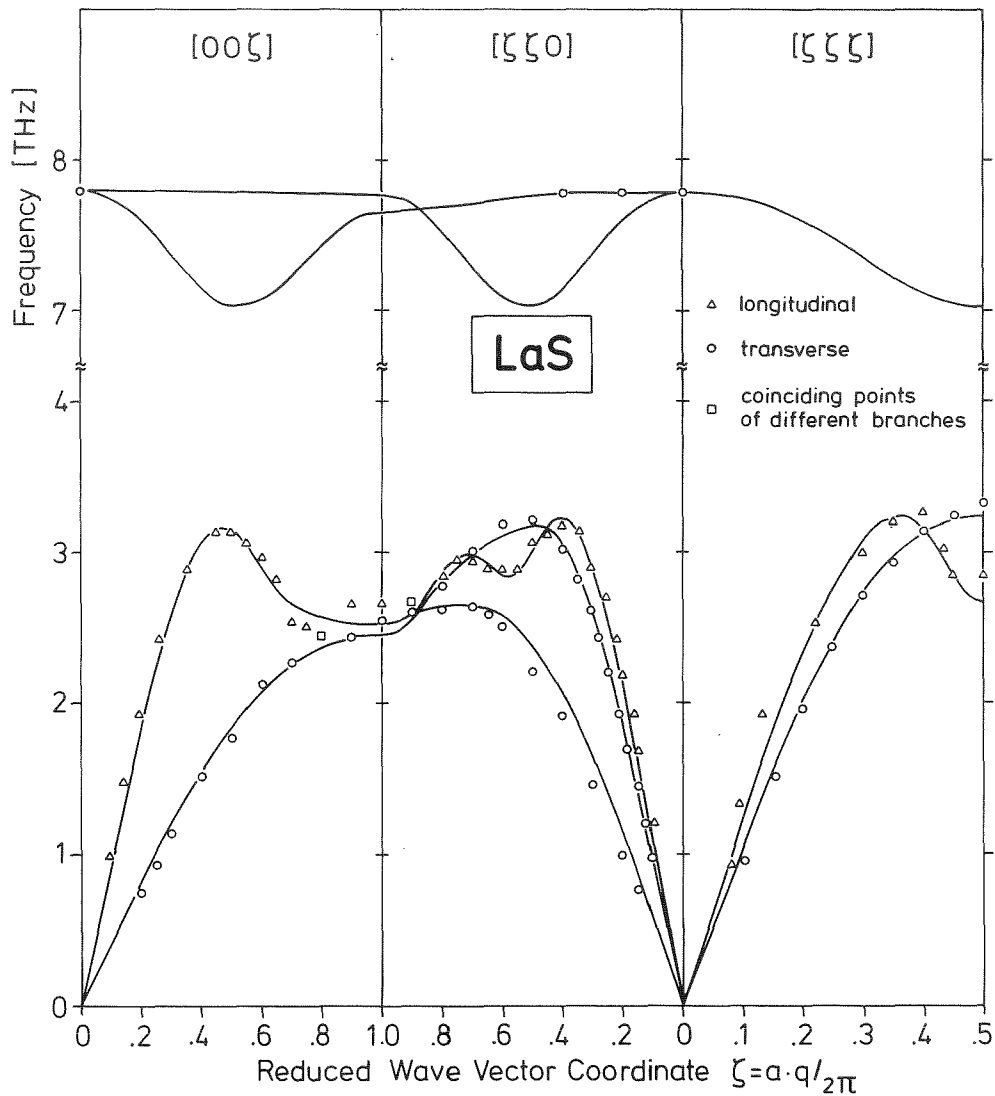
Fig.   Phonon dispersion of LaS at 296 K

References

/1/ B.W. Roberts, J. Phys. Chem. Ref. Data 5, No. 3 (1976)

/2/ P. Roedhammer, W. Reichardt, and F. Holtzberg, Phys. Rev. Lett. 40, 465 (1978)

/3/ L.E. Toth, Transition Metal Carbides and Nitrides, New York, 217 (1971)

1.2   Soft-mode Behaviour in the Phonon Dispersion of YS

P. Roedhammer[a], W. Reichardt, and F. Holtzberg[b]

[a]*Fachbereich Physik, Universität Konstanz, D-7750 Konstanz*

[b]*IBM Thomas J. Watson Research Center, Yorktown Heights, New York 10598, U.S.A.*

Abstract

We have measured the phonon dispersion of the superconducting transition metal chalcogenide YS by inelastic neutron scattering. The longitudinal branches exhibit well-defined soft-mode regions that closely resemble those found in the structural and electronic analogs NbC and TiN. In contrast no softening is observed in the transverse-acoustic (TA) branches. The experimental dispersion curves are well reproduced by calculations based on a double shell model.

1.3   Lattice Dynamics of Vanadium Nitride

Part I : Phonon Dispersion

L. Pintschovius, P. Roedhammer[a], A.N. Christensen[b], and W. Reichardt

[a]*Fachbereich Physik, Universität Konstanz, D-7750 Konstanz*

[b]*Institute of Inorganic Chemistry, University of Aarhus, Denmark*

In our previous studies of the phonon dispersion in $VN_{.86}$ /1/ the acoustic branches except the TA-branch in 100-direction could be followed only up to about the middle of the Brillouin zone. This was due to the fact that the scattering from the vanadium atoms is almost completely incoherent and the amplitudes of the nitrogen atoms get small for large q-vectors.

Our investigations have been continued by three measurements on the three-axis spectrometer IN8 at the HFR Grenoble. The coherent part has been separated from the high incoherent background by several series of constant energy scans covering very large regions in reciprocal space. The intensity contour maps computed from these data allow to determine phonon frequencies even for those q-values where the structure factor is not more than 10 % of the maximum structure factor at the Γ-point (an example of a contour map is given in Fig. 1). Thus we believe that we have really reached the limits of the experimental feasibility, except for the TA_1-branch in 110-direction.
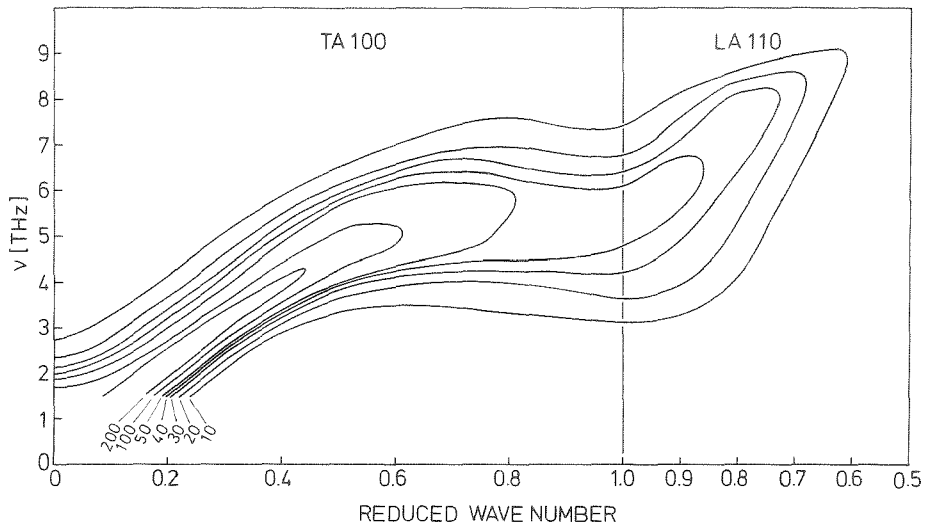
Fig. 1   Normalized intensity contours of the coherent part of the scattering
for the TA branch in 100-direction and the connecting part of the LA
branch in 110-direction.
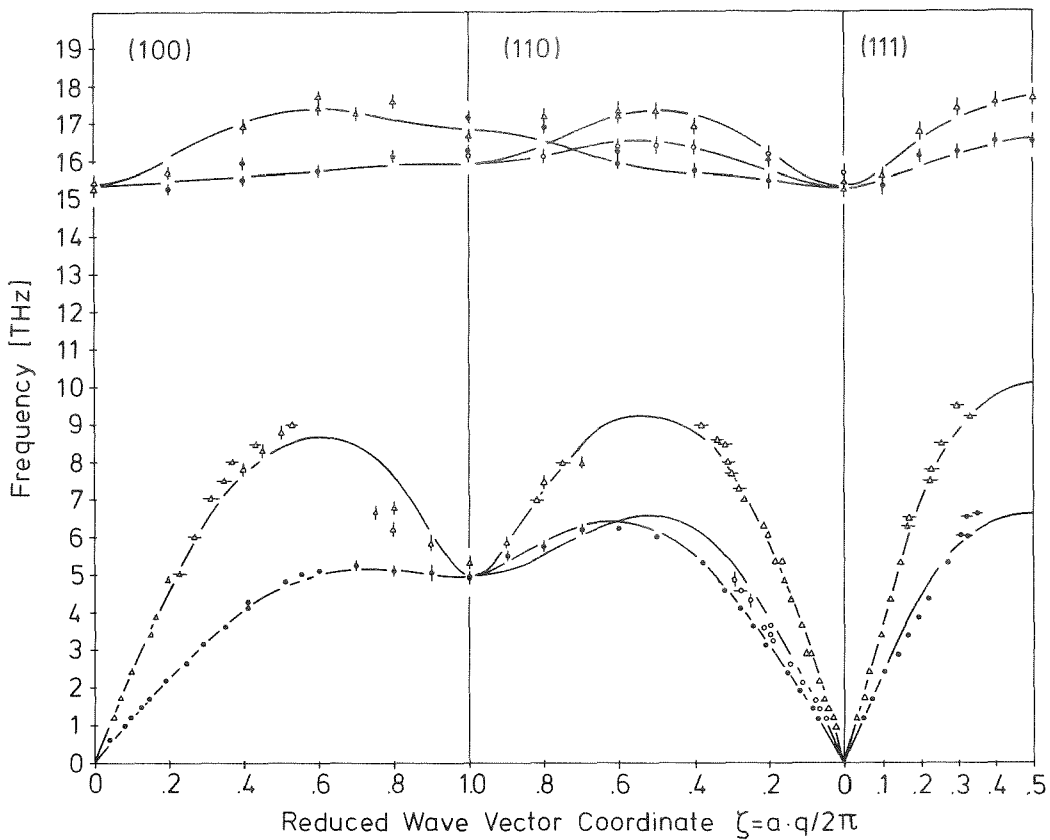
Fig. 2   Phonon dispersion in VN$_{.86}$. The lines are the results of a fit based
on the double shell model of Weber /4/.

The results are plotted in Fig. 2. The most important feature is the fact that there is a pronounced anomaly at the X-point and not, as in other superconducting transition metal compounds (TMC's), in the middle of the Brillouin zone. Similar results have recently been obtained for NbN /2/. This clearly confirms our idea /3/ that the lattice dynamics of TMC's with 10 valence electrons (VE) is quite different from that of the TMC's with 9 VE, e.g. NbC.

It is observed that the phonon linewidths are very large in the vicinity of the X-point, up to about 4 THz. Perhaps this is due to the high content of vacancies in the sample.

A fit based on the double shell model of Weber /4/ is satisfactory, although there are some discrepancies in the acoustic region (Fig. 2). We do not attach much physical significance to the parameters, but use the model just as an interpolation scheme for computing the density of states. Calculations based on a microscopic theory are currently made by W. Weber.

References

/1/ L. Pintschovius, P. Roedhammer, and A.N. Christensen, in Prog. Rep. Teil-
     inst. Nukl. Festkörperphysik, Ges. f. Kernforschung, KFK 2538, 8 (1977)

/2/ W. Reichardt, this report, p. 7

/3/ F. Gompf, L. Pintschovius, W. Reichardt, and B. Scheerer, in Proc. Conf.
     Neutron Scattering, Gatlinburg (USA), 129 (June 1976)

/4/ W. Weber, Phys. Rev. B8, 5082 (1973)

Part II : Determination of the Phonon Density of States

W. Reichardt, N. Nücker, and F. Gompf

In an previous report /1/ we have compared the phonon density of states that had been obtained from a model fitted to the experimental dispersion curves of $VN_{.86}$ at small wave vectors with results of scattering law experiments on powder samples. It was shown that there existed considerable discrepancies especially in the low frequency region.

Part of these discrepancies could be caused by differences in chemical composition and different amounts of impurity concentrations. Therefore we have determined the generalized phonon density of states $G(\hbar\omega)$ for the same sample of $VN_{.86}$ -consisting of two single crystals-that had been used previously for the phonon measurements. Experiments were performed on a time-of-flight

spectrometer (TOF3) at the FR2. In order to average over all sample orientations the two single crystals were continuously rotated around two mutually per- pendicular axes within an angular range of 360 and 45 degrees, respectively, during the course of the experiment.

The acoustic part of the generalized phonon density of states $G(\hbar\omega)$ extracted from this experiment is shown in the figure. It is compared with the former results for $VN_{1.0}$ and $VN_{.93}$. A considerable hardening of the spectra with increasing vacancy concentration is observed whereas the shapes are rather similar for all three distributions. In addition the figure shows $G(\hbar\omega)$ cal- culated from the model which has been described in Part I. The discrepancies between the experimental and calculated distribution can only partly be explained by the considerable broadening of the phonon groups near the zone boundary observed in the measurements of the dispersion curves. Therefore we have to conclude that the model does not predict correctly the dispersion surface in directions not covered by the experiment.
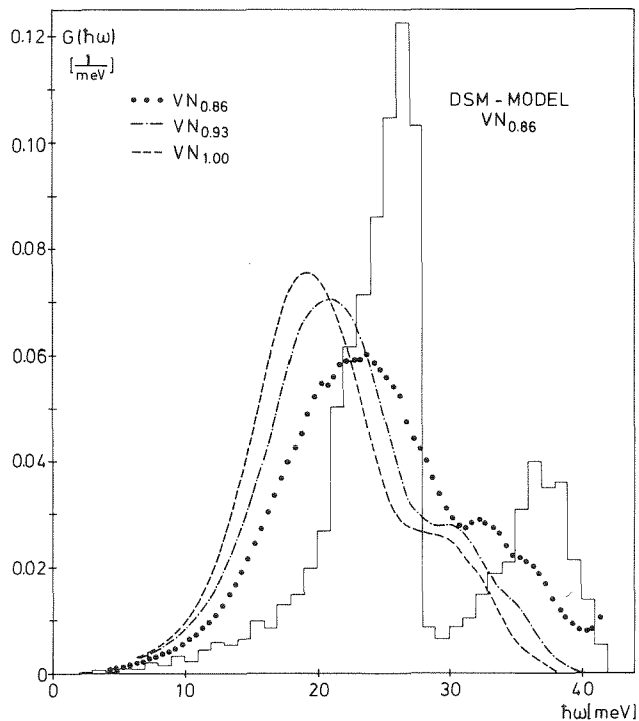
Fig.   Generalized phonon density of states of vanadium nitride as function
        of nitrogen concentration. Comparison with a model calculation.

Reference

/1/ W. Reichardt and F. Gompf, in Prog. Rep. Teilinst. Nukl. Festkörperphysik,
    Ges. f. Kernforschung, KFK 2538, 10 (1977)

1.4   Phonon Dispersion of Cubic δ-NbN$_{.83}$

W. Reichardt

Measurements of the phonon density of states of cubic δ-NbN /1/ led to the
indirect conclusion, that the dispersion curves are considerably different from
those of the superconducting transition metal compounds with 9 valence electrons
which show pronounced anomalies around the reduced wave-vector coordinate $q_x = .5$.
This conclusion was supported by incomplete measurements of the dispersion
curves of γ-NbN /1/, which is tetragonal with a deviation from the cubic symmetry
of about 1 %.

Recently it became possible to grow single crystals of the δ-phase with
sufficient size to allow measurements of the phonon dispersion curves /2/. Two
single crystals were coaligned to form a sample with a total volume of .2 cm^3.
Measurements on a high resolution neutron diffractometer showed that the crystals
were pure cubic δ-phase. From the lattice constant a chemical composition of
NbN$_{.83}$ was deduced.

Measurements of the dispersion curves were performed on the triple-axis-
spectrometer TAS1 at the FR2. The main data so far obtained are shown in the
figure. The most striking feature is the strong depression of the phonon
branches in the vicinity of the X-point, which has also been observed in VN
/3/ and which is quite different from the behavior of the phonon branches in
the superconducting refractory compounds with 9 valence electrons. In this region
the phonon shapes are extremely broad as is indicated by the bars in the figure
giving the FWHM of the experimental distributions after corrections for back-
ground, cross-section and spectrometer luminosity. In contrast no significant
softening of the phonons occurs at the L-point.

The dashed lines in the figure indicate our former results for tetragonal
γ-NbN. This comparison shows that the dispersion curves of the tetragonal and
the cubic phases are rather similar. However, for γ-NbN no broadening beyond
the experimental resolution has been observed in the [100] LA and [110] TA1
branches near the X-point.

So far no reliable information about the behavior of the LA branches in
the [100] and [110] directions around q = .5 could be obtained. This is partly
caused by the small dynamical structure factor in this region. In addition
there are indications of a considerable broadening of the phonon groups.

Although it is most likely that the extreme broadening of certain phonon groups is caused by the great number of N-vacancies in our non-stoichiometric sample this phenomenon is not yet well understood. Measurements of the phonon density of states as a function of N concentration /4/ suggest that this broadening persist also at smaller N vacancy concentrations whereas in the strongly non-stoichiometric γ-NbN the phonons appear to be much better defined. Therefore we must conclude that besides the N vacancies also defects in the Nb sublattice and ordering of the vacancies have to be considered for a satisfactory explanation of the phonon shapes in NbN.
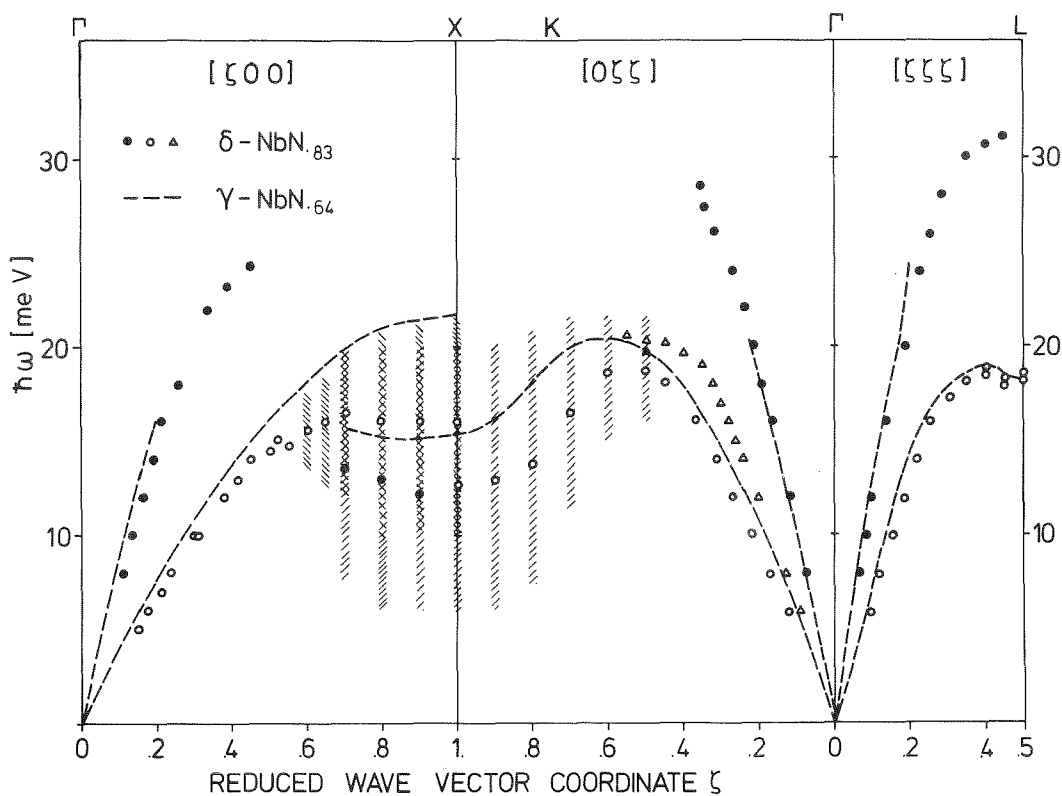
Fig.   Phonon-dispersion of δ-NbN$_{.83}$

References

/1/ F. Gompf, L. Pintschovius, W. Reichardt, and B. Scheerer, in Proc. Conf. NeutronScattering, Gatlinburg (USA), 129 (June 1976)

/2/ B. Scheerer and D. Ewert, this report, p. 112

/3/ L. Pintschovius, P. Roedhammer, A.N. Christensen, and W. Reichardt, this report, p. 3

/4/ F. Gompf, W. Reichardt, and A.N. Christensen, in Prog. Rep. Teilinst. Nukl. Festkörperphysik, Ges. f. Kernforschung, KFK 2357, 11 (1976)

1.5   Phonon Spectrum of Niobium Germanium with A15 Structure

N. Nücker and W. Reichardt

As an extension of former systematic studies on the phonon spectra of superconducting A15-compounds /1/ we measured the phonon density of states of non-stoichiometric niobium germanium containing 20 at.% of Ge. It is only at this composition that the pure A15 structure (A_3B) is obtained by chemical methods. Sample preparation is described in /2/. The superconducting transition temperature of our sample was 6.5 K. Neutron diffraction measurements showed that the material was almost pure A15 phase with traces (< 5 %) of Nb_5Ge_3. According to Geerk et al./3/ the chemical formular should be written as $Nb_3(Ge_{.8}Nb_{.2})$ because about 20 % of the B-sites are occupied by Nb-atoms.

Measurements have been performed on the multidetector time-of-flight spectrometer TOF1 at the FR2. The figure shows the generalized phonon density of states $G(\hbar\omega)$ of $Nb_3(Ge_{.8}Nb_{.2})$ at 296 K, which is defined as

$$G(\hbar\omega) = (\sum_i c_i \frac{\sigma_i}{M_i})^{-1} \cdot \sum_i c_i \frac{\sigma_i}{M_i} F_i(\hbar\omega)$$

where c_i, σ_i, M_i, $F_i(\hbar\omega)$ are the concentrations, scattering cross-section, atomic masses and partial phonon densities of states, respectively, of the two components. For comparison we also show the result of a similar experiment on Nb_3Sn (full line) and the distribution of the transition metal vibrations in the A15 structure as determined in /1/ (dashed line).

Although $Nb_3(Ge_{.8}Nb_{.2})$ is a defect structure our result fits rather well into the systematics found in the phonon spectra of superconducting A15 compounds /1/. This applies both to the average frequency and the detailed shape of the distribution function. The pronounced peak near 20 meV which we attribute to the Nb vibrations lies at the same position as in Nb_3Sn. The low frequency peak in Nb_3Sn caused mainly by the Sn vibrations is shifted towards higher frequencies in $Nb_3(Ge_{.8}Nb_{.2})$ due to the smaller mass of the B-atom and has almost completely merged into the main peak leaving only a slight indication of a shoulder as is marked by the shaded area. Under the assumption that the inter-atomic forces are identical in Nb_3Sn and $Nb_3(Ge_{.8}Nb_{.2})$ we predict $\sqrt{<\omega^2>}$ of $G(\hbar\omega)_{Nb_3(Ge_{.8}Nb_{.2})}$ to be 21.6 meV using the results of Nb_3Sn. The value calculated from our measurements is 20.7 meV.
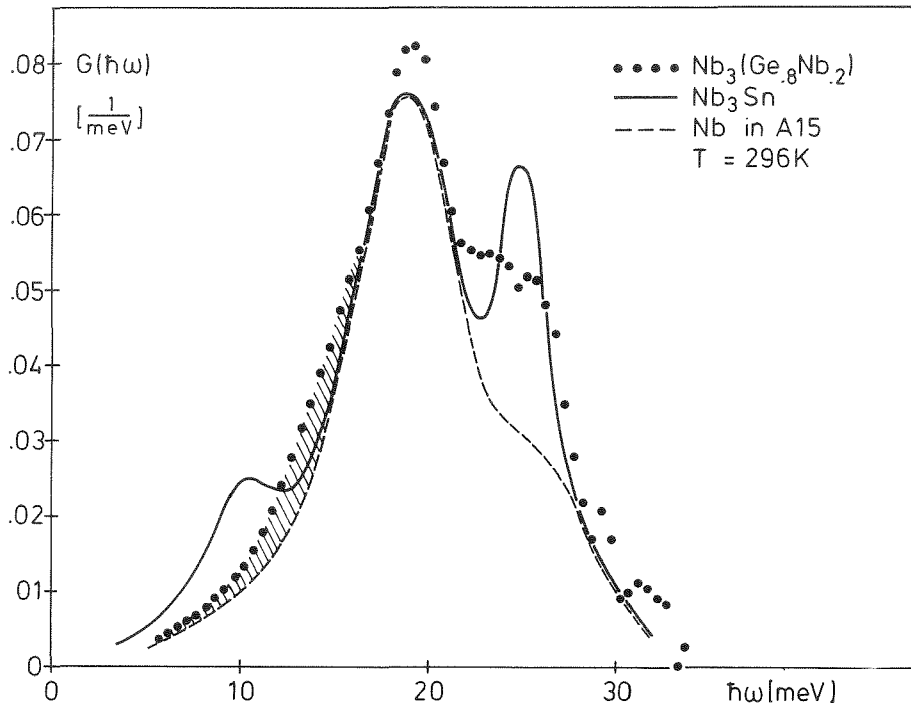
Fig. Generalized phonon density of states of $Nb_3(Ge_{.8}Nb_{.2})$ at 296 K

We believe that the phonon density of states $F(\hbar\omega)$ of Nb_3Ge at room temperature will not be very different from the present result of $G(\hbar\omega)$ for $Nb_3(Ge_{.8}Nb_{.2})$. This is caused by the fact that the weighting factor $\frac{\sigma}{M}$ in the equation above gives a stronger weight to the Ge-vibrations in $G(\hbar\omega)$ which is partly compensated by the lower Ge concentration. On the basis of the systematics given in /1/ we expect the second frequency moments of $G(\hbar\omega)_{Nb_3(Ge_{.8}Nb_{.2})}$ and $F(\hbar\omega)_{Nb_3Ge}$ to differ by only 2 %.

References

/1/ B.P. Schweiss, B. Renker, E. Schneider, and W. Reichardt, in Super-
   conductivity in d- and f-Band Metals, edited by D.H. Douglass,
   Plenum Press, New York, 189 (1976)

/2/ B. Scheerer and D. Ewert, this report, p. 112

/3/ J. Geerk, G. Linker, M. Kraatz, and B. Scheerer, this report, p. 104

1.6   Phonon Softening of V_3Si between 573 K and 295 K

B.P. Schweiss

For further information about the anomalous phonon softening in A15 compounds we extended our measurements of the phonon density of states /1/ to a temperature far above room temperature, e.g. 573 K.

The V_3Si sample used in this experiment was produced by high frequency melting of the elements under argon pressure. By X-ray analysis no other phases besides the A15 structure were detectable. The superconducting transition temperature was 16.7 K which corresponds to the transition temperature of the stoichiometric compound.

The scattering experiment was performed on the time-of-flight spectrometer TOF2 at the cold source of the FR2 in the energy gain mode with an incident energy of 5 meV. In this case the energy resolution is good only at low frequencies, contrary to the energy loss scattering mode of our previous experiments carried out at the IN4 TOF spectrometer at the HFR Grenoble with an incident energy of 60 meV. To facilitate the comparison of the spectrum measured at 573 K with the other spectra the room temperature measurement has been repeated on TOF2.

The figure shows the results of the two experiments. The peak at 42 meV which corresponds to the Si vibrations is slightly lower and broader than in the previously determined spectra /1/ which is due to the poorer resolution in the new experiment. The anomalous phonon softening with decreasing temperature - precursor of the cubic to tetragonal transformation near the superconducting transition temperature - outweighs the normal phonon softening with increasing temperature due to lattice expansion also in the temperature region above 295 K. But this effect is considerably smaller compared to the effect found between 295 K and 77 K and remains restricted to the range of the Vanadium vibrations. Between 573 K and 295 K the mean Vanadium frequency is lowered by about 2 % whereas the mean frequency of the whole V_3Si spectrum is changed by not more than half a percent.
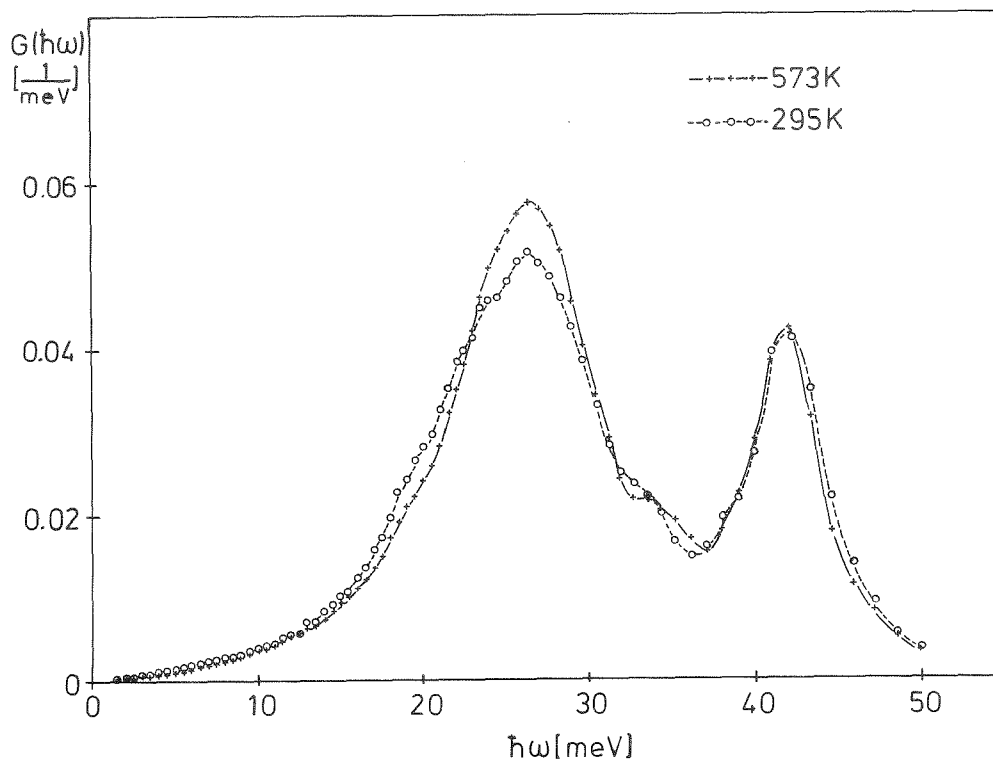
Fig. Comparison of the phonon density of states of V_3Si at 573 K and 295 K

Reference

/1/ B.P. Schweiss, in Prog. Rep. Teilinst. Nukl. Festkörperphysik, Ges. f. Kernforschung, KFK 2054, 12 (1974)

1.7 Investigations on the Partial Debye Waller Factors of Nb_3Sn

C. Geibel

Extending the investigations on the partial Debye Waller factors of Nb_3Sn /1/, we performed neutron diffraction measurements on Nb_3Sn powder samples at 77 K and 696 K. The Debye Waller factor is in the harmonic approximation given by $\exp\left(-\frac{1}{3} Q^2 <u^2>_i\right)$, where Q is the scattering vector and $<u^2>_i$ is the mean square displacement of the atom i. In the figure we have plotted the logarithm of the Debye Waller factor as a function of Q^2. A, B, C, D refer to the different structure factors we can observe in the A15 phase (see /1/).
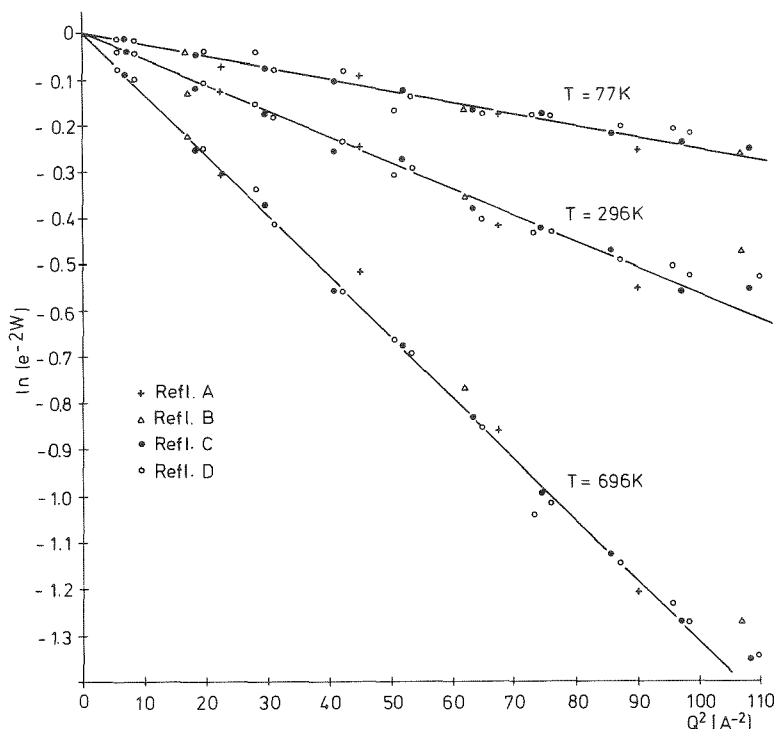
Fig.   Debye-Waller factor of Nb_3Sn

Our results are summarized in table 1. The data are corrected for thermal diffuse scattering. In the A15 phase the local symmetry at the Nb sites is $\bar{4}2m$. Therefore, we can distinguish the mean square displacement of a Nb atom perpendicular to the Nb chain $<u_{33}^2>$ from the corresponding value along the chain $<u_{11}^2>$. The ratios between $<u_{33}^2>$ and $<u_{11}^2>$ determined from our measurements are not very accurate, since they where obtained from powder samples. They are quite similar to the ratio found in V_3Si /3/. The decrease of the ratio at 77 K could be due to the influence of the martensitic transformation (T_m = 43 K) where the Nb atoms are shifted along the Nb chains.

From the mean square displacement $<u^2>_i$ we determined for each atomic species the inverse second frequency moment $<\omega^{-2}>_i$ and its Debye cutoff frequency $(\Theta_{-2})_i$. From these values we calculated the Debye cutoff frequency of the generalized phonon density of states $(\Theta_{-2})_g$ and compared it with the value determined directly from $G(\hbar\omega)$ (see following table).

T [K]	$<u^2>_{Sn}$	$<u^2>_{Nb}$	$\dfrac{u_{33}^2}{u_{11}^2}$	$\Theta_{-2\,Sn}$	$\Theta_{-2\,Nb}$	$(\Theta_{-2g})^{<u^2>}$	$(\Theta_{-2g})^{G(\hbar\omega)}$
696	4.00 (16)	4.00 (6)	1.16 (6)	254 (5)	287 (6)	280 (6)	(302)
296	1.63 (8)	1.74 (8)	1.15 (4)	262 (7)	286 (7)	282 (7)	(287)
77	0.694 (7)	0.761 (7)	1.00 (10)	223 (13)	245 (13)	241 (13)	(261)

The large decrease of the Debye cutoff frequency between 296 K and 77 K
is the consequence of the softening of the phonon spectrum which was already ob-
served in measurements of sound velocities, specific heat, and the phonon density
of states. In contrast to the phonon density of states measurements /2/ we did not
observe a phonon hardening between room temperature and 700 K.

Since the mean square displacements $<u^2>_i$ in V_3Si have already been
determined in X-ray experiments /3/ we calculated for both compounds the
product $(M\Theta^2_{-2})_i$ for T = 300 K:

	Nb	Sn	V	Si
$(M\Theta^2_{-2})_i$ [eV $Å^{-2}$]	0.345	0.370	0.385	0.369

This confirms the conclusions of Ref. /4/ that in the A15 compounds the
product $M_i<\omega^2>_i$ is nearly the same for both components and constant for a given
number of valence electrons.

References

/1/ C. Geibel, in Prog. Rep. Teilinst. Nukl. Festkörperphysik, Ges. f. Kern-
forschung, KFK 2538, 19 (1977)

/2/ N. Nücker and E. Schneider, in Prog. Rep. Teilinst. Nukl. Festkörperphysik,
Ges. f. Kernforschung, KFK 2538, 19 (1977)

/3/ J.L Staudenmann, P. Coppens, and J. Müller, Sol. State Commun. 19, 29 (1976)

/4/ B.P. Schweiss, B. Renker, E. Schneider, and W. Reichardt, in Superconductivity
in d- and f-Band Metals, edited by D.H. Douglass, Plenum, New York, 189 (1976)

1.8   Phonon Measurements on Molybdenum Chalcogenides

B.P. Schweiss, B. Renker, and R. Flükiger[a]

[a]*Département de Physique de la Matière Condensée, Université de Genève*

Phonon density of states measurements of chevrel phase superconductors
gave reveiling insights into the lattice dynamical properties of this class of
compounds. The essential results are a molecular crystal model by which parts
of the phonon spectra could be correlated to vibrations of different species of
particles /1/ and the observation of an anomalous temperature behaviour roughly
correlated to the superconducting transition temperature /2/.

Measurements of phonon branches on a single crystal provide additional information and allow to study in detail the general features outlined above. Recently small single crystals of $Cu_2Mo_6S_8$ and Mo_6Se_8 have become available /3/ and phonon measurements have been started at the Karlsruhe FR2 reactor. These investigations proved to be difficult since there are only a few lattice points with sufficiently good structure factors and since the size of the sample was rather small ($\sim$ .25 cm^3). Phonons have been measured along the trigonal axis and along the rhombohedral (OO1) and (11O) directions. The latter directions have been chosen since the rhombohedral cell differs only by the very small angular distortion of $\sim 1^\circ$ from the cubic one. Finally a larger experimental effort was taken for Mo_6Se_8 since for this system a pronounced anomalous temperature behaviour has been observed in the generalized phonon density of states $G(\hbar\omega)$ /2/.

Fig. 1a) and 1b) show the correlation between the singularities in the low energy part of $G(\hbar\omega)$ and extrapolated zone boundary energies of phonon branches.
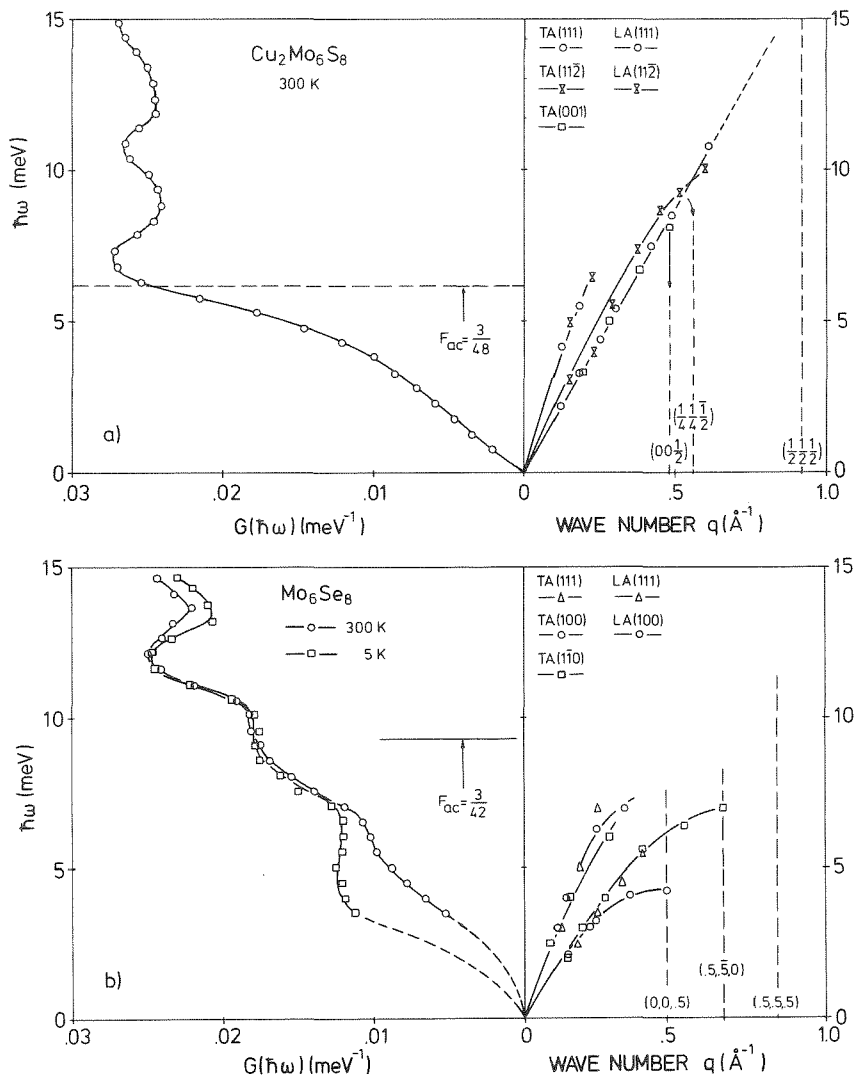
Fig. 1   Comparison of the low energy part of the generalized frequency distribution and acoustic phonon branches of $Cu_2Mo_6S_8$ (Fig. 1a)) and Mo_6Se_8 (Fig. 1b)), respectively

$F = \dfrac{3}{3N}$ (N = number of particles in the unit cell) marks that part of the total area of $G(\hbar\omega)$ which nominally accounts for the acoustical vibrations. The agreement between both sets of data is evident for Mo_6Se_8. For the ternary compounds the acoustical spectrum is much harder and extends clearly above the limit of 3/48 which proves the existence of low lying optical branches attributed to vibrations of the Cu atoms.

Fig. 2 gives the low temperature results obtained for Mo_6Se_8 up to now. Indications for a phonon softening appear for the TA branch in $(1\bar{1}0)$ direction polarized along (110). Unfortunately this branch could not be followed to the zone boundary for intensity reasons. A similar temperature dependence has not been observed for the other branches. Since for the Mo_6Se_8 sample a second slightly misorientated crystallite has been detected the above results still must be checked. In the cubic system a softening of that particular TA branch affects the difference $C_{11} - C_{12}$ of the elastic constants and is characteristic for a tetragonal distortion. For some rhombohedral chevrel phase compounds a transition into a orthorhombic phase has been reported /4/. The present temperature dependent investigations of phonon branches will be continued.
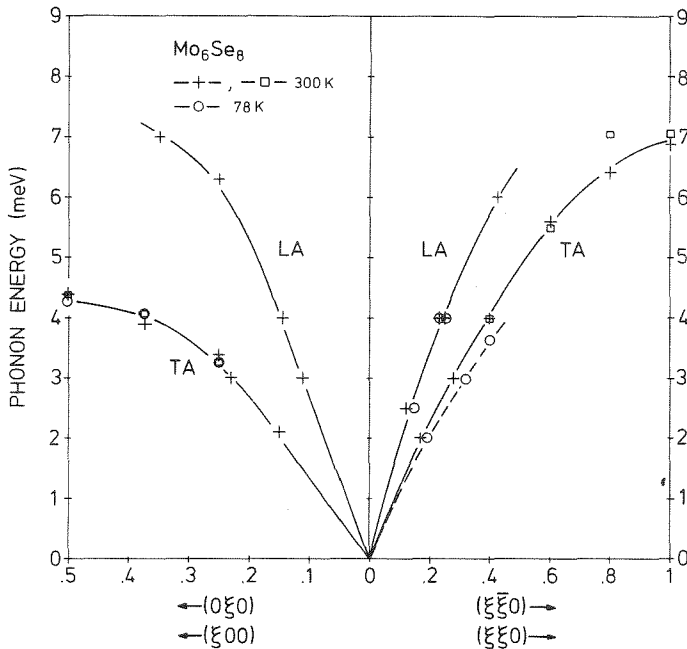
Fig. 2

Acoustic phonon dispersion of Mo_6Se_8 for room temperature and 78 K showing possibly a softening of the TA branch in (110) direction. Measuring points marked by squares (-□-) refer to the rhombohedral (100) and (110) directions, respectively

References

/1/ S.D. Bader, G.S. Knapp, S.K. Sinha, B.P. Schweiss, and B. Renker, Phys. Rev. Lett. 37, 344 (1976)

/2/ B.P. Schweiss and B. Renker, J. de Physique (1978), to be published

/3/ R. Flükiger, H. Devantay, J.L. Jorda, and J. Muller, IEEE Trans. Magn. 13, 818 (1977)

/4/ A.C. Lawson, Mat. Res. Bull. 7, 773 (1972)

1.9 Lattice Vibrations in the Superconducting Hexaborides of Lanthanum and

Yttrium

F. Gompf

The hexaborides of Y and La belong to a series of extremely hard, refractory and stable MB_6 materials characterized by strong covalent bonds /1/. Both compounds have a simple cubic lattice structure (space group Pm3m) with 7 atoms per unit cell. In Fig. 1 we show the three-dimensional framework of interlocked B_6 octahedra which form a cage around the metal atom. For both compounds the interatomic distances are rather similar. The lattice constants
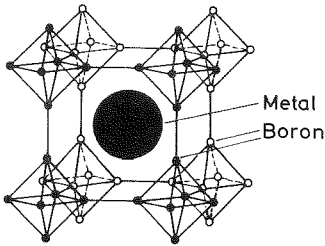
Fig. 1

The cubic metal
hexaboride structure

a_o (4.14 Å for LaB_6 and 4.09 Å for YB_6) are primarily determined by the boron framework structure and not by the size of the embedded metal atoms. LaB_6 and YB_6 display a metallic behaviour and are often referred to as "covalent metals". LaB_6 is for instance a good thermionic emitter and is currently successfully used as an electronic microscope cathode /2/. Both compounds are also superconductors, their T_c values, however, being strikingly different ($LaB_6:T_c$ = 0.45 K, $YB_6 : T_c$ = 7.1 K).

These interesting properties have recently given rise to several investigations /3, 4/. Walch et al. /3/ investigated the energy bands and bonding in LaB_6 and YB_6. They deduced the electronic density of states of LaB_6 and by comparing them concluded: « These results are sufficiently similar to apparently rule out the factor of ∿ 15 difference in T_c as due to simple density of states effects. It now appears desirable to consider the phonon spectra and/or lattice defect structure for further enlightenment ». For these compounds "soft" (transition-metal-based) phonon modes could play an important part and strongly affect the superconducting properties.

Even though it is very difficult to perform an inelastic neutron scattering experiment on these compounds due to the high absorption cross section of boron (about 700 barns at 25 meV), such measurements seem of interest in order to

      i) localize the predicted "soft" phonon modes and

     ii) try to correlate anomalous frequency shifts (if existing) with T_c.

On the FR2 we have performed preliminary inelastic neutron scattering experiments on polycrystalline LaB_6 and YB_6 using an incoming energy of 64.3 meV. Parts of the time-of-flight distributions as registered in the time-of-flight channels (background substracted) are shown in Fig. 2a and b. The spectra were measured in the energy loss mode. The position of the elastic line and the size of significant energy transfers are marked by indicators. For LaB_6 we measured a low frequency peak around 13 meV, which can only be attributed to La-based modes. The rest of the spectrum is uncertain due to additional strong background contributions from epithermal neutrons for which the energy dependent absorption cross section σ_{abs}. has become quite small and subsequently they are preferably scattered by the sample. For YB_6 which has similar interatomic forces the equivalent Y-based modes should peak around 16 meV due to the difference in mass. The experimental result shown in Fig. 2b displays a shift in the opposite direction and indicates the existence of energetically localized "soft" phonon modes in YB_6. The rest of the spectrum is too vague to the discussed due to the small signal to background ratio (note size of errobars for YB_6 after one week of measuring time).
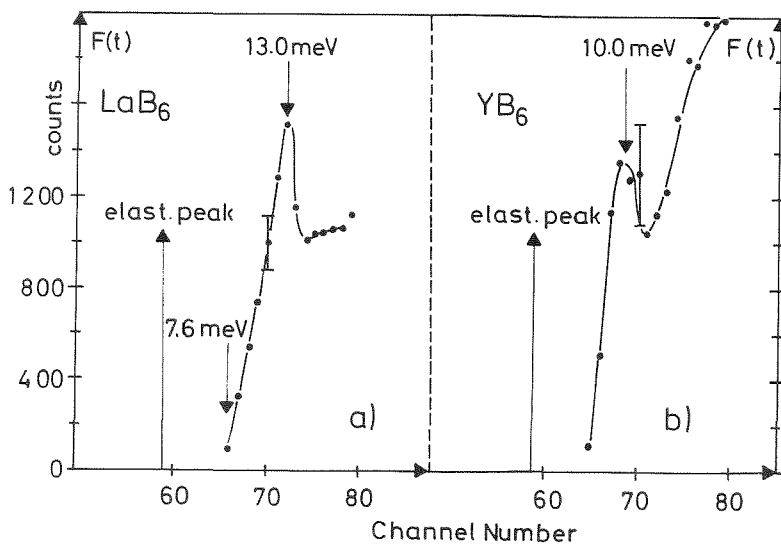
Fig. 2

Time-of-flight spectra of a) LaB_6 and b) YB_6 for small energy transfers. The experiment was performed at TOF1 with an incident energy of E_o = 64.3 meV.
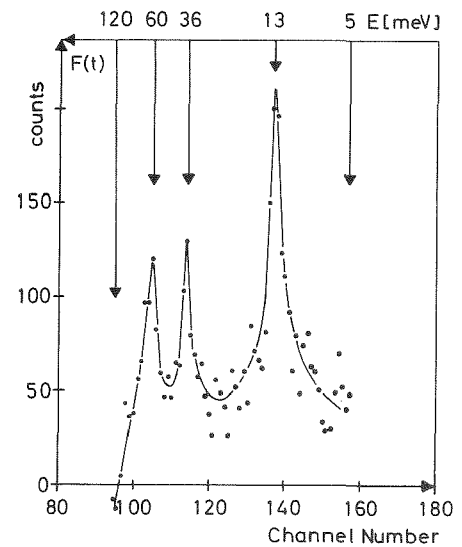
Fig. 3

Time-of-flight spectrum of LaB_6. The experiment was performed at TOF2 with an incident energy of E_o = 5 meV.

The background situation was less severe at TOF II, the multidetector time-of-flight spectrometer at the cold source. Even though boron has an absorption cross section of about 1600 barns for the incoming 5 meV neutrons, after a measuring time of 3 weeks we were able to deduce a well structured time-of-flight distribution which is shown (background subtracted) in Fig. 3. Again we found the pronounced peak at 13 meV plus two additional peaks at 36 and 60 meV. The frequency spectrum seems to end at around 120 meV. Whether higher frequencies exist cannot be concluded from this experiment. The statistical deviations are still too large to deduce a reliable phonon density of states from these data.

To improve the scattering power of the MB_6 compounds we are now trying to prepare them with B^{11} enriched Boron.

References

/1/ V.J. Matkovich, Boron and Refractory Borides, Springer-Verlag Berlin, Heidelberg, New York (1977)

/2/ H. Ahmed and A.N. Broers, J. Appl. Phys. 43, 2185 (1972)

/3/ P.F. Walch, D.E. Ellis, and F.M. Mueller, Phys. Rev. B15, 1859 (1977)

/4/ A. Hasegawa and A. Yanase, J. Phys. F.: Metal Phys. 7, 1245 (1977)

1.10 Investigations of the Polymeric Metal $(SN)_x$

Part I : Lattice Dynamics

L. Pintschovius, R. Currat[a], R. Pynn[a], and H. Wendel[b]

[a] Institut Laue-Langevin, F-38042 Grenoble, France
[b] Universität Ulm

The inelastic neutron scattering studies of $(SN)_x$ have been continued /1, 2/. The main emphasis has been laid on the search for Kohn anomalies. The results of two measurements at the ILL and at the FR2 have been published in the following publication.

L. Pintschovius, R. Currat, and H. Wendel

Abstract

The dispersion of acoustic phonons in $(SN)_x$ has been measured for small wavevectors parallel and in three directions perpendicular to the chain axis by means of inelastic neutron scattering. The longitudinal acoustic and a low optic branch in chain direction have been determined up to the zone boundary. The results are analysed on the basis of a valence force model. Optical data of Stolz et al. [1] for high optic modes are included in this analysis. It turns out that the strongest interchain force constants are by almost two orders of magnitude smaller than the largest intrachain force constant.

One of the goals of the measurements was the search for a Kohn anomaly in the longitudinal acoustic branch in chain direction. Two small dips have been found at $q = 0.14 \cdot 2\pi/b$ and $q = 0.25 \cdot 2\pi/b$, respectively. These values agree nicely with the predictions of a band structure calculation performed by Rudge and Grant [3].

The experiments mentioned in the above abstract have been carried out on a sample consisting of 14 crystals with a total volume of 0.5 cm^3. In order to further improve the experimental conditions we built a new sample holder which allowed to align 36 crystals. Thus the sample volume could be increased to 0.9 cm^3. This sample was used for measurements with improved resolution at room temperature and at 80 K which were carried out in Karlsruhe and in Grenoble, respectively. These investigations confirmed the occurrence of two small dips in the longitudinal acoustic branch in chain direction at $q = .15 \cdot 2\pi/b$ and $q = .25 \cdot 2\pi/b$ found in our previous experiments (Fig.). We think that these dips are most likely due to the Kohn effect: their positions correspond to the diameters of the electron and of the hole pocket in $(SN)_x$, respectively, as calculated by Rudge and Grant [3]. The dips are not enlarged on cooling which indicates that their size is not limited by the smearing but by the curvature of the Fermi surface which is consistent with the band structure calculations cited above.

It is intended to complete these experiments by measurements at other reciprocal lattice points to rule out other explanations for the dips.
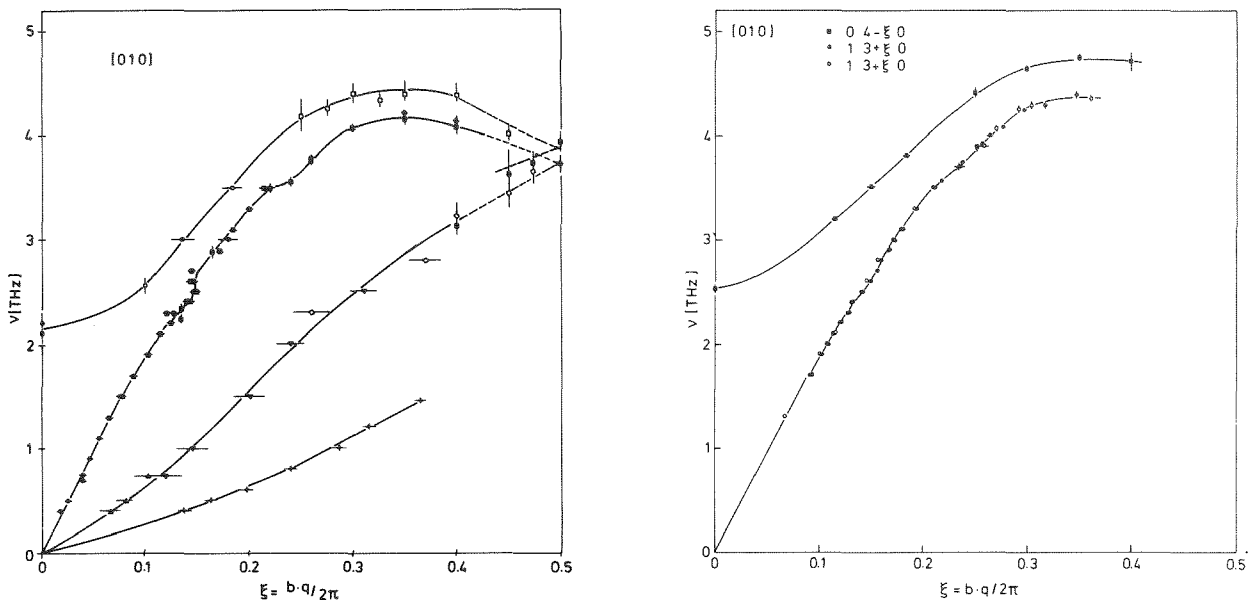
Fig. Dispersion relation of low frequency phonons traveling in chain direction at room temperature (left) and at 80 K (right). Different symbols refer to measurements at different reciprocal lattice points. Lines are a guide to the eye.

References

/1/ H.J. Stolz, H. Wendel, A. Otto, L. Pintschovius, and H. Kahlert, Phys. Stat. Sol. (b) 78, 277 (1976)

/2/ L. Pintschovius, H. Wendel, H.J. Stolz, A. Otto, H. Kahlert, and R. Currat, in Prog. Rep. Teilinst. Nukl. Festkörperphysik, Ges. f. Kernforschung, KFK 2538, 32 (1977)

/3/ W.E. Rudge and P.M. Grant, Phys. Rev. Lett. 35, 1799 (1975)

Part II : Superconductivity in Polymeric Sulfur Nitride (SN)$_x$ at
High Pressure

W.H.G. Müller[a], F. Baumann[a], G. Dammer[b], and L. Pintschovius

[a]Physikalisches Institut der Universität Karlsruhe
[b]Pädagogische Hochschule Karlsruhe

Abstract

Investigations of the pressure dependence of the superconducting transition temperature T_c up to 17 kbar, and of the normal conductivity up to 50 kbar are reported. It is observed that below 8 kbar, the value of T_c increases linearly with the pressure. In addition, there is a significant drop of T_c at about 9 kbar which may be due to a phase transition.

1.11 Acoustic Phonon Dispersion of UAl_2

B. Renker and J. Buerkin[a]

[a]*IMF I, Kernforschungszentrum Karlsruhe GmbH*

Extremely high values for the electronic contribution γ = 90 mJ/(K^2 mole) to the specific heat have been reported for UAl_2 /1/, a cubic Laves phase type compound (a = 7.744 Å). This large value of γ is equivalent to the very high density of states N(O) = 19.2 · eV^{-1} $atom^{-1}$ at the fermi level and indicates the presence of an extremely narrow band, presumably a 5f band. The second remarkable feature is a sharp upturn in C/T below 2O K which has been shown to be consistent with the assumption of spin fluctuations /2/. It might be expected that these unusual electronic properties could cause a strong re-normalization and an anomalous temperature behaviour of phonon frequencies.

We have obtained single crystalline pieces ($\sim$ .5 cm^3) of UAl_2 by con-trolled cooling down of the melt. Larger parts of LA and TA phonon branches could be measured along the (1OO) and (11O) symmetry directions within a (OO1) scattering plane at room and liquid nitrogen temperature (see figure).
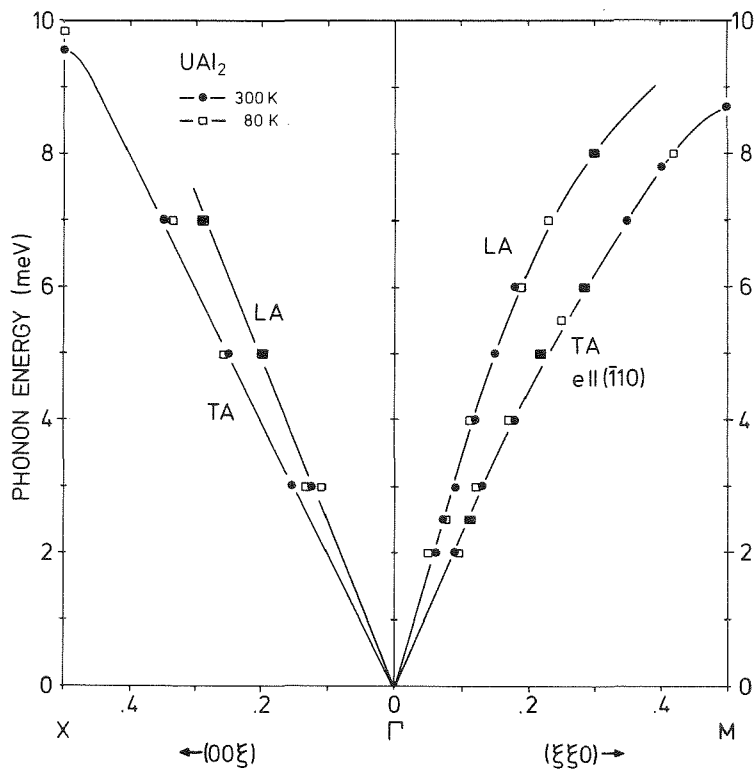
Fig. Acoustic phonon dispersion curves for UAl_2 at room temperature and 80 K.

Since for this orientation of the sample the measured slopes of the LA and TA branches at small wavevectors contain information about all three elastic constants c_{11}, c_{12}, and c_{44} of the cubic system the results are representative for all directions in the crystal.

Within the experimental error the present data do not show any anomalous temperature behaviour of phonon frequencies above 80 K. Typical values observed for the phonon linewidth are $\sim$ .8 meV and are fully consistent with the instrumental resolution. With the restriction that the present results are not complete and that measurements below 80 K have not been performed it seems that the anomalously high density of states N(O) is not reflected in the acoustic phonon branches.

References

/1/ R.J. Trainor, D.B. Brodsky, and H.V. Culbert, 22nd Conf. on Magnetism and Magnetic Materials, Pittsburg, Pennsylvania, June 15 - 18 (1976)

/2/ R.J. Trainor, D.B. Brodsky, and H.V. Culbert, Phys. Rev. Lett. 34, 1019 (1975)

1.12   Stress-Induced Changes in the Phonon Spectrum of Silicon

J. Estel[a], J. Kalus[a], R. Scherm[b], and L. Pintschovius

[a] Universität Bayreuth

[b] Institute Laue-Langevin, F-38042 Grenoble, France

Our investigations of the effect of uniaxial pressure on the phonon spectrum of silicon /1, 2/ have been continued. In the preceding experiment the TA-branch in the 100-direction was investigated. In the present experiment we intended to measure the energy shifts of the optical branches in the 100-direction. A first test was performed on the triple-axis-spectrometer at the FR2 in Karlsruhe, whereas the main part of the measurements were carried out on the IN8 triple-axis spectrometer at the HFR in Grenoble.

A preliminary evaluation yields the following results: both the TO- and LO-phonons are shifted to higher frequencies with pressure, in contrast to the TA-branch, which exhibits a negative energy shift near the zone boundary. The maximum frequency shift occurs in the TO-branch at $q \approx .2 \cdot 2\pi/a$, when the polarisation vector is parallel to the applied stress. In this case the shift amounts to $\Delta\omega/\omega = (8 \pm 2.5) \cdot 10^{-3}$ at $p = 8.5$ kbar.

It is intended to complete these measurements by investigating the LA-branch in the 100-direction.

References

/1/ J. Prechtel, J. Kalus, and L. Pintschovius, in Prog. Rep. Teilinst. Nukl. Festkörperphysik, Ges. f. Kernforschung, KFK 2183, 10 (1975)

/2/ J. Prechtel, Thesis, TU München (1976)

1.13 Lattice Dynamics of α-Calcium Formate

W. Dyck[a], B.P. Schweiss, H. Fuess[a], N. Burger[a,b], and H.D. Schuster[a]

[a]Institut für Kristallographie der Universität Frankfurt

[b]Institute Laue-Langevin, F-38042 Grenoble, France

The structure of α-Ca(HCOO)$_2$ (orthorhombic, space group Pcab /1/) consists of chains of Ca^{2+} ions parallel to the c-axis, laterally bound through formate groups. The elastic, dielectric, and thermal properties of this compound are largely anisotropic /2/.

The study of α-Ca(HCOO)$_2$ by X-N methods revealed the deformation density between Ca and the formate groups /3/. Neutron backscattering experiments have shown the inelastic contribution to the Bragg scattering to be highly anisotropic /3/.

For the interpretation of the experimental data we are developing a lattice dynamical model assuming the formate groups to be rigid molecules with translational and rotational degrees of freedom interacting via atom-pair potentials. Raman and infrared spectra /4, 5/ enable a suitable choice of the model parameters.

The phonon density of states reflects the contributions of lattice frequencies due to all wavevectors in the Brillouin-zone and provides additional data for the elaboration of the lattice dynamics model and the investigation of the thermal diffuse scattering. Experiments on undeuterated as well as on deuterated α-Ca(HCOO)$_2$ (Fig.) were carried out at room temperature with the rotating crystal TOF spectrometer at the cold source of the FR2 using an incident neutron energy E_o = 5.09 meV.

The pronounced differences between the two densities are due to the contribution of hydrogen especially to the high-frequency vibrations. Because the entire formate groups are involved in the external modes the observed lineshifts between the two spectra are not simply related to the mass difference between hydrogen and deuterium.
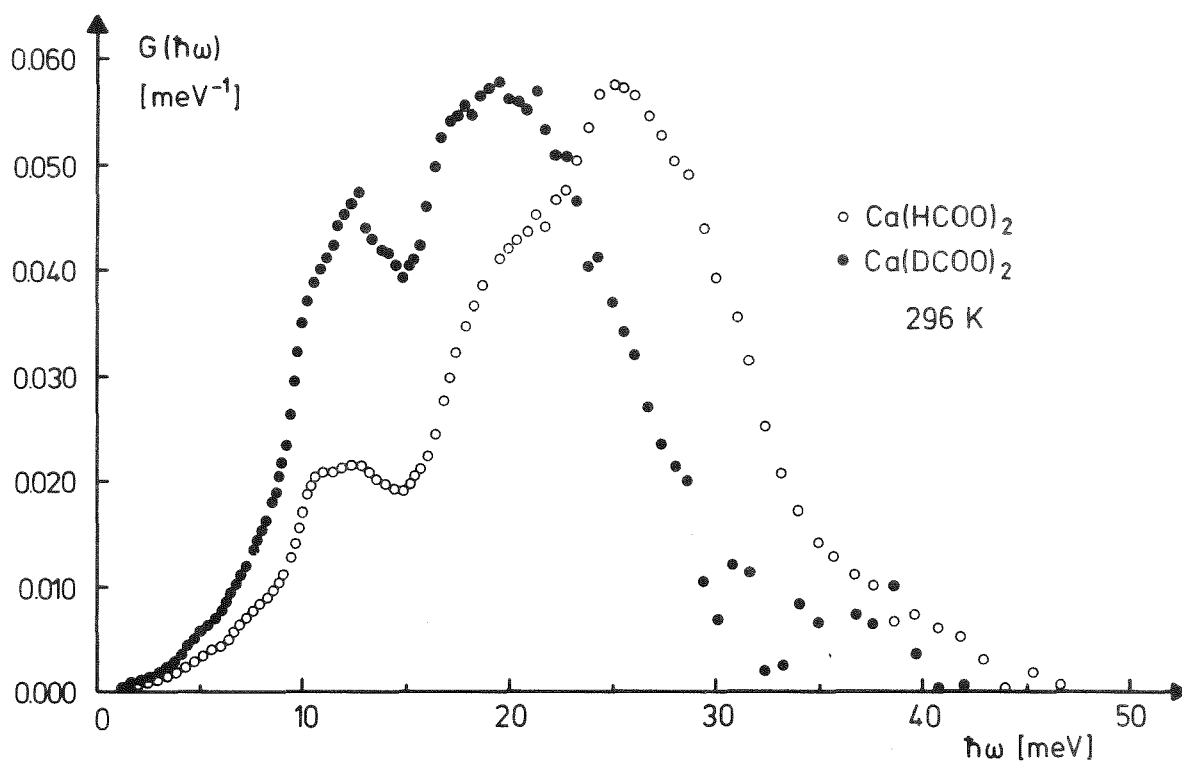
Fig.   Comparison of the amplitude weighted phonon density of states of normal and deuterated α-Calcium formate in the external modes region (the densities are normalized to unit area).

References

/1/ N. Burger, H. Fuess, and S.A. Mason, Acta Cryst. B33, 1969 - 1970 (1977)

/2/ L. Bohatý and S. Haussühl, Z. Kristallogr. 145, 172 - 176 (1977)

/3/ N. Burger and H. Fuess, unpublished results

/4/ R.S. Krishnan and P.S. Ramanujam, J. Raman Spectrosc. 1, 533 - 538 (1973)

/5/ K.B. Harvey, B.A. Marrow, and H.F. Shurvell, Can. J. Chem. 41, 1181 - 1187 (1963)

1.14 Inelastic Neutron Scattering Measurements on Melamine, $C_3N_6H_6$

(2,4,6-Triamino-1,3,5-triazine)

H.D. Schuster[a] *and B.P. Schweiss*

[a]*Institut für Kristallographie der Universität Frankfurt*

Melamine has four molecules per unit cell in general positions, the space group is $P2_1/a$. Its structure was determined by X-ray and neutron diffraction experiments /1, 2, 3/. The free molecule has $\bar{6}m2$ symmetry. In the crystal each molecule is linked to its neighbours by hydrogen bonds. Therefore melamine may serve as a model for the study of the dynamical behaviour of the nucleic acids in biochemistry.

Inelastic scattering measurements have been done on normal and deuterated polycrystalline melamine at room temperature with the rotating crystal TOF spectrometer at the cold source (E_0 = 5.05 meV) of the FR2 Karlsruhe. The figure shows the amplitude weighted phonon density of states of normal and deuterated melamine in the frequency range of 0 to 100 meV. In addition infrared and Raman frequencies /4, 5/ are indicated at the bottom of the figure.
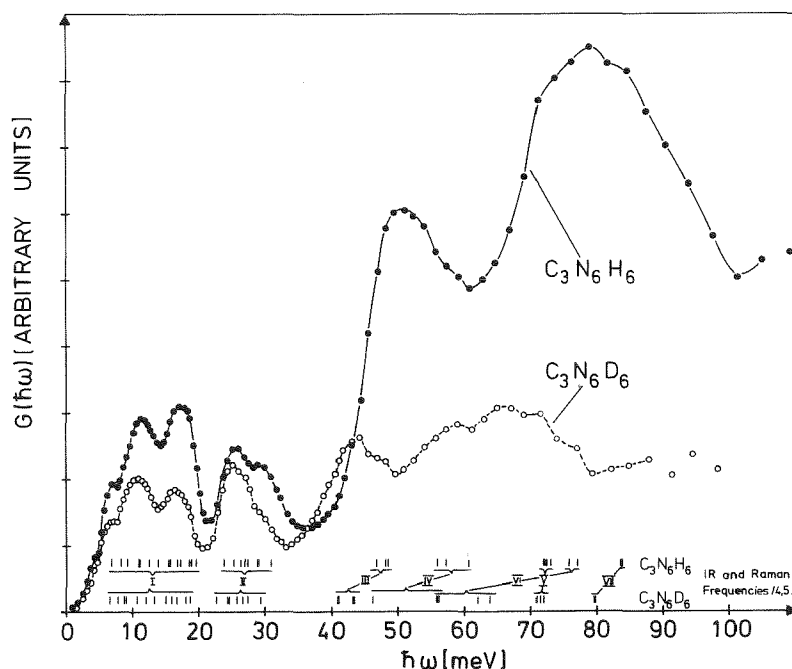
Fig. Comparison of the amplitude weighted phonon density of states of normal and deuterated melamine in the frequency range of 0 to 100 meV. Roman numerals refer to the tabulated vibration modes.

The normal coordinate analysis of melamine at wavevector q = O allows the selection of seven different types of vibration modes within the range of O - 85 meV (table). An extended lattice dynamical calculation is planned by us in the near future.

Table   Range of Frequencies (meV) in melamine

No.	undeut.	deut.	Vibration modes of Melamine
I	O - 20	O - 20	lattice vibrations
II	20 - 36	20 - 33	out of plane vibrations of NH_2 groups
III	45 - 50	40 - 45	in plane vibrations of NH_2 groups
IV	55 - 65	45 - 55	torsional vibrations of NH_2 groups
V	70 - 75	70 - 75	in plane vibrations of the triazine ring
VI	75 - 80	55 - 65	out of plane vibrations of H atoms
VII	80 - 85	75 - 80	out of plane vibrations of the triazine ring

References
/1/ E.W. Hughes, J. Amer. Chem. Soc., 63, 1737 (1941)
/2/ A.C. Larson, D.T. Cromer, J. Chem. Phys. 60, 185 (1974)
/3/ J.N. Varghese, A.M. O'Connell, and E.N. Maslen, Acta Cryst. B33, 2102 (1977)
/4/ J.R. Schneider and B. Schrader, J. Mol. Struct. 29, 1 (1975)
/5/ J.R. Schneider, B. Schrader, and P. Bleckmann, Ber. Bunsenges. Phys. Chem. 79, 1026 (1975)

1.15   Lattice Vibrations in Crystalline and Amorphous Selenium

F. Gompf

In extension of our investigations on trigonal and vitreous Se /1/ we performed an inelastic neutron scattering experiment on red amorphous Se using the multidetector time-of-flight spectrometer TOF II. The sample was prepared by reducing cooled (∿ 5° C) H_2SeO_3 with $[N_2H_6]SO_4$. The precipitated red amorphous Se was filtered out, washed with alcohol and ether and afterwards dried in U.H.V.. The structure was checked by X-ray diffraction.

As can be seen in the table the intrachain (or ring) distances of next (r_1) and second next (r_2) neigbors   remain nearly the same for all three modifications while the next neighbor interchain distances (r_3) increase going from the crystalline to the disordered states and are largest for the red amorphous modification.

	$r_1 [\overset{o}{A}]$	$r_2 [\overset{o}{A}]$	$r_3 [\overset{o}{A}]$
trigonal	2.31	3.69	3.46
vitreous	2.32	3.69	3.69
red amorphous	2.32	3.69	3.86

In Fig. 1 we compare the recently measured phonon density of states for red amorphous Se with those of the trigonal and vitreous modifications /1/. Up to 25 meV the spectrum is almost identical with vitreous Se. The higher optical frequencies, however, primarily made up by stretching modes, are shifted by about 1.5 meV to higher frequencies as expected when the molecule units approach one-dimensionality (see /1/).

Etchepare et al. /2/ used a generalized valence force field model (for the short range forces) and combined it with a bond charge model (for the long range coulombic forces) to fit the dispersion relations for trigonal Se of Teuchert /3/. With the help of this model they calculated the phonon density of states which is compared with our results in Fig. 1.
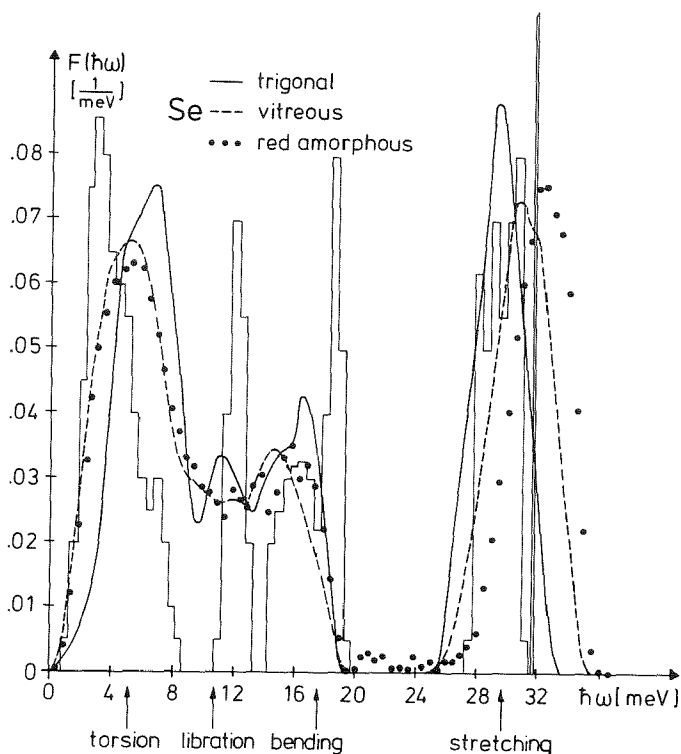
Fig. 1

Comparison of the phonon density of states of red amorphous Se with those of the trigonal and the vitreous modifications. The hystogram is a model calculation for trigonal Se by Etchepare et al. /2/.

The agreement with our F($\hbar\omega$) for trigonal Se is not very good but in both spectra we find four characteristic intensity maxima which are labeled at the bottom of the figure:

i) the low lying torsional modes which become softer for the disordered systems

ii) a peak caused by librations is found for the trigonal modification. These are rotational modes about the helical axis where the restoring forces are caused by neighboring chains. As to be expected this libration peak disappears for the disordered systems where the molecular units are further apart and the chains largely unmeshed.

iii) the bending modes which seem to remain the same for all three modifications except for a sharp peak around 17 meV for trigonal Se. The decrease of this peak for the disordered modifications could be interpreted with the help of a theoretical model by Meek /4/, who calculated vibrational spectra for amorphous Se for different dihedral angles ψ (Fig. 2).

For $\psi = 102^O$ ($\triangleq$ cryst. Se) the bending modes display an additional sharp peak at the upper limit of the lower frequency band. For $|\psi| = 102^O$, i.e. all dihedral angles having the crystalline magnitude but the sign variing randomly along the chain, he finds a very similar spectra for the bending modes except for a sharp decrease of this peak. If the sign of the dihedral angles ψ alternates we of course get the Se_8 puckered ring molecule.

Fig. 2   Local coordination
          of Se atoms in the
          chain.

iv) considering that our spectrum is only partially corrected for resolution, the agreement of the stretching modes is good. The sharp peak at the cutoff frequency of the calculation seems to be inherent to their model since their highest branch of the optic modes is flat and does not reproduce the dispersion observed by /3/.

From F($\hbar\omega$) we deduced the Debye temperature θ_D as a function of tempera-ture which is shown in Fig. 3 for the two disordered modifications. Between 10 and 20 K θ_D is practically identical, then gradually growing apart reaching at 298 K a θ_D of 307 K for red amorphous Se and $\theta_D \approx 296$ K for vitreous Se while
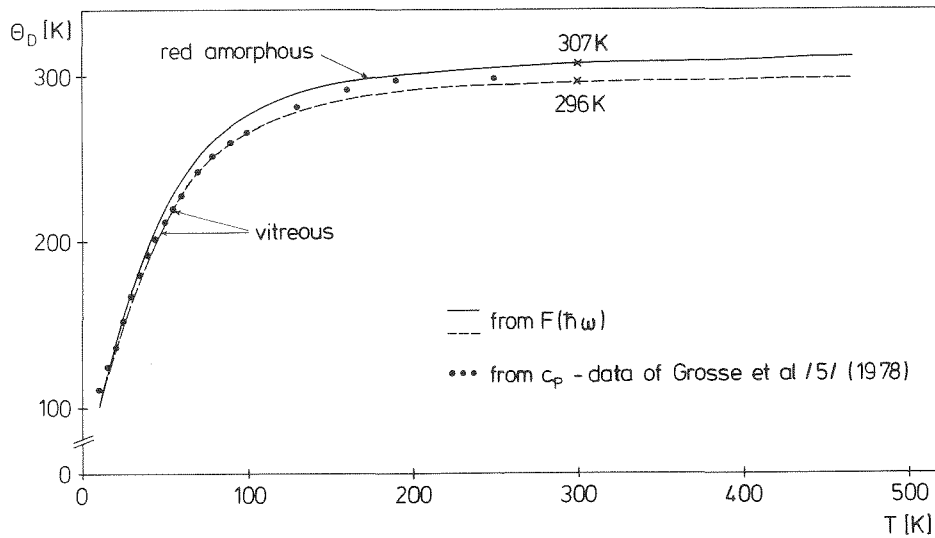
Fig. 3   Comparison of the Debye temperatures as a function of temperature for red amorphous Se with vitreous Se.

the trigonal modification yielded a room temperature value of 286 K. Grosse et al. /5/ have recently published specific heat data for vitreous Se, from which we calculated θ_D and compare it with our results. The agreement between 10 K and 130 K is excellent considering the sensitiveness of this comparison. The differences at higher temperatures (especially at 298 K) are to be expected since small errors in Cp give rise to large deviations in θ_D.

References

/1/ F. Gompf, in Prog. Rep. Teilinst. Nukl. Festkörperphysik, Ges. f. Kern-forschung, KFK 2538, 38 (1977)

/2/ Etchepare, P. Kaplan, and M. Merian, in Proc. Int. Conf. of Lattice Dynamics, Paris, 60 (1977)

/3/ W. Teuchert, Phonons in Trigonal Selenium, Dissertation, University of Würzburg (1975)

/4/ P.E. Meek, Phil. Mag. 34, 767 (1976)

/5/ R. Grosse, P. Krause, M. Meissner, and A. Tausend, J. Phys. C11, 45 (1978)

1.16 Critical Neutron Scattering from $(CD_3ND_3)_2MnCl_4$ near the Structural Phase Transition at T_c = 390 K

N. Lehner, R. Geick[a], K. Strobel[a], V. Wagner[b], and G. Heger

[a]*Physikalisches Institut der Universität Würzburg*

[b]*Institute Laue-Langevin, F-38042 Grenoble, France*

In $(CD_3ND_3)_2MnCl_4$ a continuous order-disorder phase transition takes place at T_c = 390 K. Above T_c, the CD_3ND_3-molecules and the $MnCl_6$-octahedra perform correlated jumps around the c-axis (which is perpendicular to the $MnCl_2$-layers) between different possible sites /1, 2/. Due to such fluctuations there arises strong critical scattering around T_c.

We have studied Bragg-scattering and quasielastic scattering of neutrons from a $(CD_3ND_3)_2MnCl_4$ single crystal in the range $T_c \pm$ 25 K. For these experiments we used the neutron diffractometer D10 at the HFR in Grenoble. The primary neutron energy was 12.5 THz, the energy resolution about 5 %. The measurements were performed near the reciprocal lattice point 3 0 10, which has by far the largest structure factor, scanning along q_x (inside the layers) and q_z (perpendicular to the layers).

In the ordered phase below T_c we observed Bragg-scattering at the superlattice point 3 0 10 in order to determine the experimental line shape function. From the temperature dependence of the intensity of the Bragg peak

$$I(3,0,10) \sim (T_c - T)^{2\beta}$$

we confirm the value β = 0.32 for the critical exponent as reported by Knorr et al. /3/.

Above T_c the q-dependence of the critical scattering near the reciprocal lattice point q_o = 3 0 10 may be described by the Lorentzian

$$I(q) = I(q_o) \cdot \frac{\kappa^2}{\kappa^2 + q^2}$$

where the peak intensity $I(q_o)$ and the linewidth κ near T_c are usually assumed to vary with the temperature as

$$I(q_o) \sim (T - T_c)^{-\gamma}$$

$$\kappa \sim (T - T_c)^{\nu}$$

At first, the background has to be subtracted from the experimental raw data. In addition to a constant contribution, we observed a temperature independent, broad and q-dependent ridge of scattered intensity along the q_z-axis. The origin of this background is not completely clarified, but very probably, it is due to thermal diffuse scattering. The remaining intensity could be described by a convolution of the above Lorentzian and the instrumental Gaussian. $I(q_o)$ and κ of the Lorentzian were the parameters of the fit procedure.
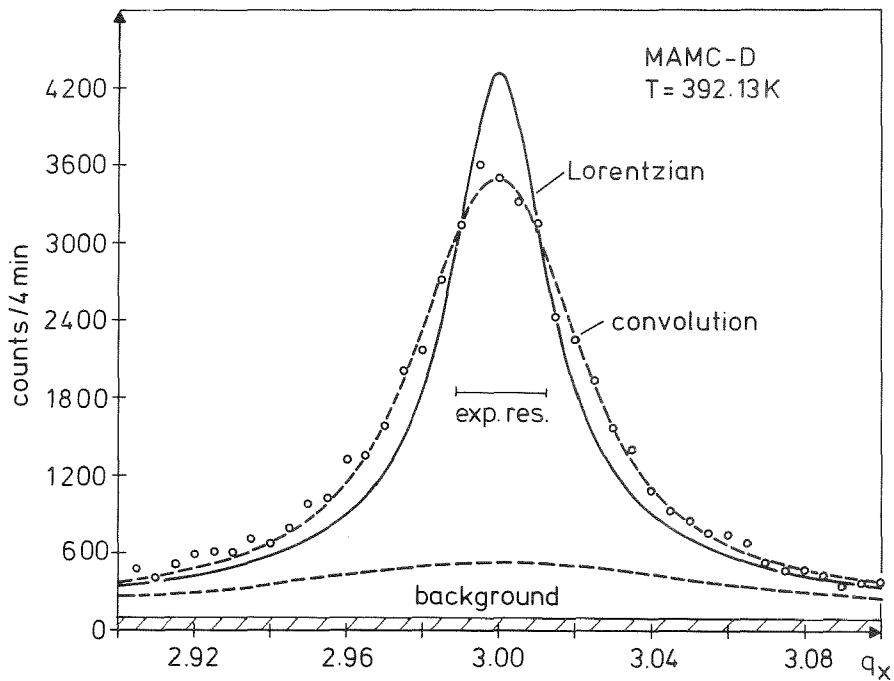
Fig. 1 q_x-scan above T_c : experimental data and the experimental background-contribution are shown as well as the convolution and the calculated Lorentzian.

From the two parameters κ and $I(q_o)$, κ is of most interest since it is the inverse of the correlation length which is finite in this temperature range. For our data the length of correlation within the layers ranges from 15 $\underline{a}$ to 116 $\underline{a}$, where $\underline{a} = 7.26\ \overset{o}{A}$ is the lattice constant. The correlation length perpendicular to the layers is smaller by a factor of 2.5, which is nearly independent of temperature, and ranges from 2 $\underline{c}$ to 10 $\underline{c}$ ($\underline{c} = 19.5\ \overset{o}{A}$) for our data. From the temperature dependence of $I(q_o)$ and κ we obtain values for the critical exponents $\gamma = 0.83 \pm 0.10$ and $\nu = 0.42 \pm 0.10$ for both q_x- and q_z-scans.
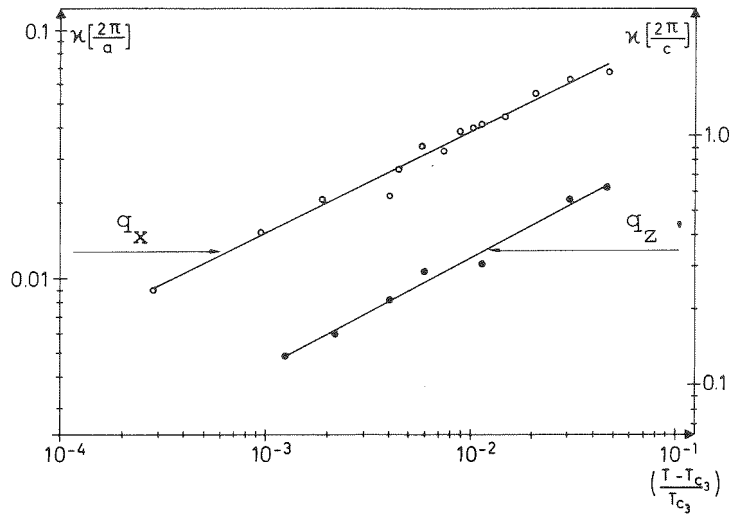
Fig. 2   Linewidths of the critical scattering above T_c as function of temperature. In the double-logarithmic scale one gets the critical exponent ν from the slope of the fitted line.

References

/1/ G. Heger, D. Mullen, and K. Knorr, Phys. stat. sol. (a) <u>31</u>, 455 (1975)

/2/ G. Heger, D. Mullen, and K. Knorr, Phys. stat. sol. (a) <u>35</u>, 627 (1976)

/3/ K. Knorr, I.R. Jahn, and G. Heger, Solid State Commun. <u>15</u>, 231 (1974)

1.17   The Structure Factor for ß-Arsenic

R. Block

The scattering intensities of amorphous ß-arsenic were measured in two experiments with different incident neutron energies (62.7 meV and 133.4 meV) at the FR2 in Karlsruhe. In the data reduction scattering from the sample container, absorption by the sample, and multiple and incoherent scattering and Placzek corrections were taken into account /1/. The data used in the analysis were σ_a = 4.3 b, σ_c = 5.92 b, σ_{inc} = 0.8 b and a density of ρ = 4.75 gr/cm^3. With the present sample geometry (cylinder, r = 0.732 cm, h = 7 cm) 15.5 % of the neutrons arriving at the sample were scattered. The contribution of multiply scattered neutrons was 11.4 %.

Fig. 1 shows the structure factor $S(Q)$ for ß-arsenic. Normalization of $S(Q)$ was achieved by a separate vanadium measurement. $S(Q)$ shows the same shape as it has been determined by other authors /2, 3/ for $Q \leqslant 7 \, \overset{\circ}{A}^{-1}$, which was the upper limit in the former experiments. Typical for this amorphous phase is the small peak at $Q = 1 \, \overset{\circ}{A}^{-1}$ with a width of $0.25 \, \overset{\circ}{A}^{-1}$. This corresponds to an interatomic distance of $2\pi/Q \approx 6 \, \overset{\circ}{A}$ and a correlation length of 25 $\overset{\circ}{A}$. In contrast to the structure factor of simple liquids, $S(Q)$ remains oscillating up to high values of Q.
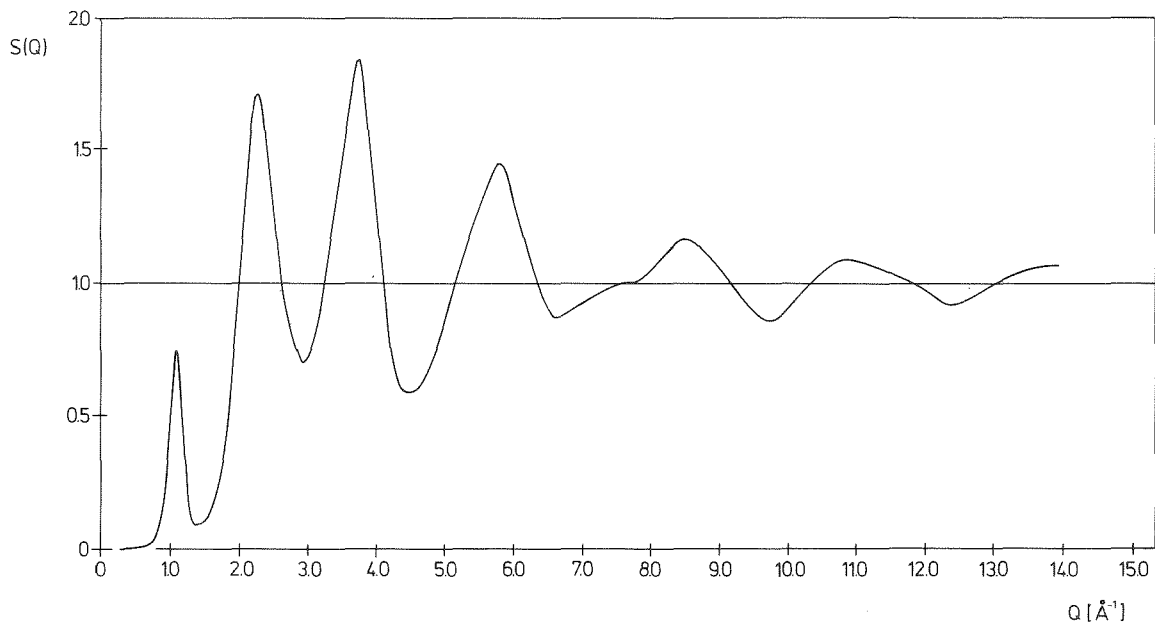
Fig. 1   Structure factor $S(Q)$ for ß-arsenic

Fig. 2 shows the pair correlation function $g(r)$ for two different upper limits in the Fourier transformation $(--- : Q_{max} = 6.3 \, \overset{\circ}{A}^{-1}, \, \underline{\quad} : Q_{max} = 13.5 \overset{\circ}{A}^{-1})$ of $S(Q)$. The $g(r)$ for $Q_{max} = 6.3 \, \overset{\circ}{A}^{-1}$ is very similar to that obtained in the X-ray experiment /3/. Expanding the range to higher Q clearly changes the height and the width of the first peak in $g(r)$. The first shell of neighbouring atoms becomes more localized; the peak is sharpened, whereas the other peaks are only weakly influenced by this procedure.

From $g(r)$ the pairpotential has been determined within the framework of the Percus-Yevick and the hypernetted-chain theories, respectively. The values, isotropic averages over the likely anisotropic pairpotential in ß-arsenic, differ quantitatively according to the approximation used.
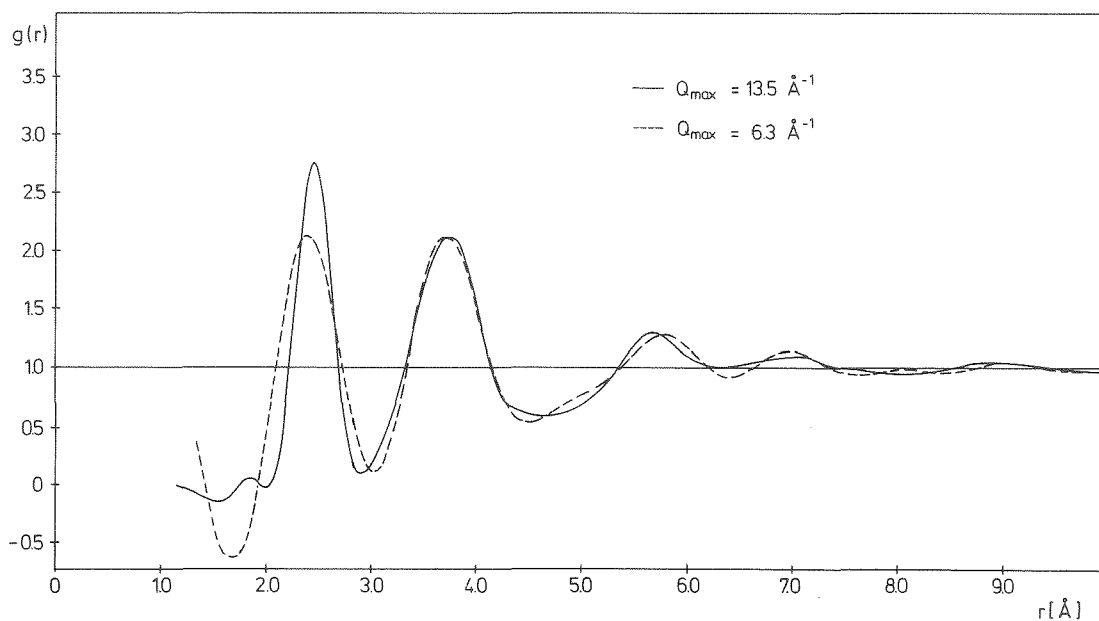
Fig. 2   Pair correlation function g(r) for ß-arsenic

References

/1/ R. Block, Kernforschungszentrum Karlsruhe, KfK 2488 (1978)

/2/ W. Reichardt, private communication

/3/ H. Krebs, F. Schultz-Gebhardt, Z. Anorg. Allg. Chem. 283, 263 (1956)

1.18   Structure Investigations of ß-Eucryptite by Means of Neutron Diffraction

H. Guth and G. Heger

ß-Eucryptite (LiAlSiO$_4$) is a good ionic conductor at high temperatures. At about 600°C total conductivities of $\sigma_{\perp} \approx 4 \cdot 10^{-4}$ (Ωcm)$^{-1}$ perpendicular and $\sigma_{\parallel} \approx 10^{-1}$ (Ωcm)$^{-1}$ parallel to the hexagonal c-axis were found (isotropic electric conductivity is several decades smaller) /1/. This pronounced one-dimensional ionic conductivity is due to the Li$^+$-ions, which are situated in "structure channels" running parallel c.

Above a phase transition at about 490°C ß-Eucryptite crystallizes in a structure similar to high quartz (space group $P6_222$ or $P6_422$) with half of the Si^{4+} being replaced by Al^{3+}. In $LiAlSiO_4$ the charge is balanced by the Li^+-ions. The alternate distribution of Si and Al in successive layers perpendicular to the c-axis causes a doubling of the c lattice constant.

Two models for the high temperature structure of ß-Eucryptite with different Li^+ distributions were proposed after X-ray analysis (Fig. 1a), 1b)). In the model of Pillars and Peacor /2/ only next nearest Li-sites in the structure channels are fully occupied ($z = 0$; 2/6; 4/6;). In the alternative model of Schulz and Tscherry /3/ the Li^+ are statistically distributed over all tetrahedral oxygen-coordinated sites ($z = 0$; 1/6; 2/6; 3/6; 4/6; 5/6);

According to the two electrons of the Li^+-ions their contribution to the scattered intensity in X-ray measurements is small. Therefore it is difficult to investigate the distribution of the Li^+-ions in ß-Eucryptite by means of X-ray studies, especially in the high temperature phase, where a partial Li^+-occupation at different sites is predicted. In order to clear up the actual high temperature structure of ß-Eucryptite we performed neutron diffraction measurements at 530°C using $^7LiAlSiO_4$ single crystals. The evaluation of a three-dimensional data set consisting of 161 symmetry independent reflection intensities confirmed the ordered distribution of Al and Si. The occupation probabilities of Li^+ were determined as (68 ± 5)% for Li(1) at $z = 0$; 2/6; 4/6; and (22 ± 3)% for Li(2) at $z = 1/6$; 3/6; 5/6;, respectively. The resulting deficiency of the total Li content (90 % instead of 100 %) may be explained by anharmonic effects and diffusion processes of the Li^+-ions. The structure parameters of Li(1) and Li(2) are summarized in Table 1a).

X-ray studies of the low temperature modification show the occurance of superstructure-reflections below 490°C which cause a doubling of the a-lattice constant with respect to the high temperature unit cell (Fig. 1c)). This means that the Li distributions in adjacent structure channels are no longer equivalent. It was further assumed that the hexagonal space group type $P6_222$ or $P6_422$ is conserved in the low temperature modification of ß-Eucryptite /2, 3/. In our neutron diffraction measurements at room temperature besides the ordinary reflections due to the space group $P6_222$ ($P6_422$) we observed (00ℓ)-reflections with $ℓ \neq 3n$, which should be systematically absent. These findings, were checked with several crystals. Recent X-ray studies have shown corresponding results. The appearance of these additional (00ℓ)-reflections means that the space group of the low temperature phase of $LiAlSiO_4$ must be of lower than hexagonal symmetry. On the other hand the observed intensity data - except for the (00ℓ)-reflections

with $\ell \neq 3n$ - show the relations due to the hexagonal space group. Therefore we have to assume a multi-domain, pseudo-hexagonal structure in the low temperature phase of ß-Eucryptite. A refinement for this averaged hexagonal structure shows no significant differences with the former X-ray results. The structure parameters of Li(1), Li(2) and Li(3) are summarized in Table 1b). A total Li^+ content of $(97 \pm 3)\%$ results. Compared with the high temperature results this increased occupation probability indicates a less mobile or more harmonic state of the Li^+-ions at room temperature.
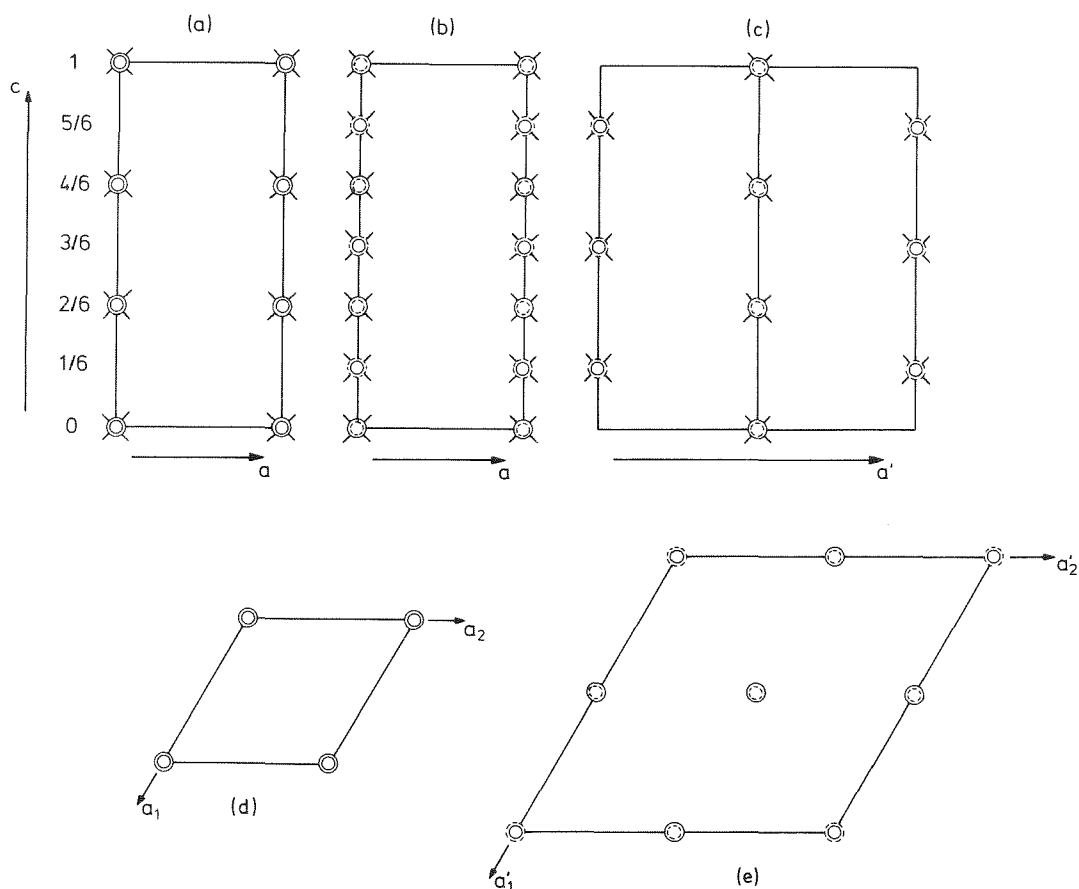
Fig. 1   Schematic representation of the Li distribution of ß-Eucryptite:

figures of the high temperature phase:
(a)   ordered Li-distribution in the a-c-plane according to the model of Pillars and Peacor /2/

(b)   statistical Li-distribution in the a-c-plane according to the model of Schulz and Tscherry /3/ (⊙ and ⊙ are nonequivalent sites)

(d)   projection on the basal $\underline{a}_1$-$\underline{a}_2$-plane of the unit cell showing equivalent "structure channels"

figures of the room temperature phase:
(c)   ordered Li distribution in the a'- c -plane

(e)   projection on the basal $\underline{a}_1'$ - $\underline{a}_2'$ -plane showing two different kinds of "structure channels"

Table 1   Structure parameters for Li of ß-Eucryptite
           a) high temperature phase,   b) room temperature phase

a)

	x	y	z	U11	U22	U33	U12	PP
Li(1)	0	0	0	3.8(8)	8(2)	10(2)	4(1)	0.68(5)
Li(2)	0	0	1/6	3(2)	1(1)	7(3)	2(1)	0.22(3)

b)

	x	y	z	U11	U22	U33	U12	PP
Li(1)	0	0	1/2	1.8(3)	3.0(4)	3.2(4)	1.5(2)	0.97(3)
Li(2)	1/2	0	0	2.1(4)	1.8(6)	3.7(5)	0.9(3)	0.95(3)
Li(3)	1/2	0	0.3274(6)	2.6(4)	2.7(4)	2.9(3)	1.8(3)	0.98(4)

The values of the mean square displacements UIJ are multiplied by a factor of 100 and have the dimension $\overset{o}{A}{}^2$.

References

/1/ U. v. Alpen, E. Schönherr, H. Schulz, and G.H. Talat, Electrochim. Acta 22, 805 (1977)

/2/ W.W. Pillars and D.R. Peacor, Amer. Mineral. 58, 681 (1973)

/3/ H. Schulz and V. Tscherry, Acta Cryst. B28, 2147 (1972)

1.19   Neutron Diffraction Study of the Cu^+-Ionic Conductor Cu_6PS_5Br
       at 293 K and 473 K

W.F. Kuhs[a] and G. Heger

[a]*Institut für Kristallographie der Universität Freiburg*

Recently a new family of structures with the general formula $A_{9-x} \square_x BChal_{6-z} Hal_z$ (A = Cd, Hg, Cu, Ag; B = Ga, Si, Ge, Sn, P, As; Chal = S, Se, Te; Hal = Cl, Br, I; $0 \le x \le 6$; $0 \le z \le 1$) has been synthesized and investigated /1/. In these compounds the anions form a framework of interpenetrating, centered icosahedra similar to the Laves-phase $MgCu_2$. At higher temperatures they crystallize in a cubic face-centered lattice (α-modification with the space group: F $\overline{4}$3m) with a disordered A-cation sublattice. For $Cu_6\square_3PS_5Hal$ (Hal = Cl, Br, I) the transition to the α-phase occurs already below room temperature: T_c = 247 K (Cl); T_c = 268 K (Br); T_c = 113 K (I). In their α-modification these compounds show a distinct conduction of the Cu^+-ions (for example at room temperature: σ_{ion} = 5 • 10^{-4} $(\Omega cm)^{-1}$ (Cl); σ_{ion} = 1.5 • 10^{-5} $(\Omega cm)^{-1}$ (Br); σ_{ion} = 6 • 10^{-6} $(\Omega cm)^{-1}$ (I) /2/).

To investigate the distribution of the Cu^+-ions and to study the thermal behaviour of the surrounding crystalline matrix, neutron diffraction measurements were performed at room temperature and 473 K on the bromine compound Cu_6PS_5Br in addition to former X-ray studies /3/. Sets of three-dimensional intensity data were collected on the automatic four-circle diffractometer P110 at the FR2 reactor. Details of experimental data are summarized in Table 1. To avoid extinction effects the sample crystal was quenched in liquid nitrogen.

Table 1   Experimental data for $Cu_6\square_3PS_5Br$; $Z = 4^*$

	293 K	473 K
a [Å]	9.745(4)	9.770(4)
λ_n [Å]	0.9219(5)	0.9219(5)
$(\sin\theta/\lambda)_{max}$ [Å^{-1}]	0.95	0.85
Number of reflections:		
total	971	698
symmetry-independent	204	149
sym.-ind. observed ($I_o > 2\sigma (I_o)$)	190	120
Number of variables	21	21
$R_F = \Sigma \|\|F_o\| - \|F_c\|\| / \Sigma \|F_o\|$	0.060	0.066

$^*Z = 4$: four formula units per unit cell.

The structure of the α-phase of Cu_6PS_5Br is stabilized by a scaffold of three-dimensional corner-sharing PS_4-tetrahedra, the S^{2-}-anions of which form the icosahedral framework already mentioned. The Cu^+ and the remaining S^{2-} and Br^--ions are located in structural cavities. The Cu^+-cations are distributed among two different partially occupied equipoints. Their structure parameters are given in Table 2. Cu(1) has a triangular and Cu(2) approximately a tetrahedral coordination. The remaining S^{2-} and Br^- are mostly connected to the Cu^+-ions. Their anion sites are partially occupied either by sulphur or bromine. The details of occupation probabilities and atomic parameters are also given in Table 2.

Table 2   Structure parameters for the Cu- and (S,Br)-sites of $Cu_6\square_3PS_5Br$

$Cu(S,Br)_4$		x	y	z	u_{11}*	u_{33}*	u_{12}*	u_{13}*	occup. probab.
Cu(1)	(RT)	.237(2)	.237(2)	.023(1)	3.8(8)	2.6(2)	1.5(8)	0.2(3)	0.269(3)
	(HT)	.235(1)	.235(1)	.024(1)	3.0(5)	3.3(3)	-1.0(5)	0.0(2)	0.251(3)
Cu(2)	(RT)	.192(1)	.192(1)	.020(1)	4.4(3)	3.6(4)	1.1(4)	0.4(3)	0.231(3)
	(HT)	.195(1)	.195(1)	.020(2)	5.5(5)	5.0(7)	0.7(6)	0.4(5)	0.249(3)
$Br_{0.87}S_{0.13}$(RT)		0	0	0	2.7(1)	2.7(1)	–	–	1
$Br_{0.83}S_{0.17}$(HT)		0	0	0	4.2(2)	4.2(2)	–	–	1
$S_{0.87}Br_{0.13}$(RT)		0.25	0.25	0.25	2.7(2)	2.7(2)	–	–	1
$S_{0.83}Br_{0.17}$(HT)		0.25	0.25	0.25	4.4(3)	4.4(3)	–	–	1

*The u_{ij}-values are multiplied by 100, their dimension is $\mathring{A}^2$

(RT) $\hat{=}$ room temperature and (HT)$\hat{=}$ 473 K

Comparing the results of the structure refinement for 293 K and 473 K there occur no drastic effects. The main difference is the strong increase of the temperature factors of the anions on the mixed populated sites (Br_xS_{1-x} and S_xBr_{1-x}) compared especially with those of the PS_4 tetraedra. We assume that the enhanced Cu^+ conduction at higher temperatures (at 473 K : $\sigma_{ion} = 2.5 \cdot 10^{-3}(\Omega cm)^{-1}$ for Cu_6PS_5Br) is directly connected to the higher thermal activation of their surroundings.

References

/1/ W.F. Kuhs, R. Nitsche, and K. Scheunemann, Mat. Res. Bull. 11, 1115 (1976)
   W.F. Kuhs, M. Schulte-Kellinghaus, V. Krämer, and R. Nitsche, Z. Naturforsch. 32b, 1100 (1977)

/2/ W.F. Kuhs, R. Nitsche, and K. Scheunemann, Verhandl. der DPG 6, 13, 168 (1978)

/3/ W.F. Kuhs, R. Nitsche, and K. Scheunemann, Acta Cryst. B34, 64 (1978)

/4/ J.M. Steward, Editor – Technical Report TR-446 of the Computer Science Center, University of Maryland (The numerical calculations were performed on the Univac 1100 of the Rechenzentrum der Universität Freiburg).

1.20 Structural Investigation of the Orthorhombic Phase of KCN under Uniaxial Pressure

G. Heger and A. Loidl[a]

[a]*Physikalisches Institut der Universität Mainz*

At room temperature KCN crystallizes in a cubic structure of the NaCl-type (space group: $F4/m\overline{3}2/m$). This high temperature modification is characterized by an orientational disorder of the $(CN)^-$ dumb-bell molecules with a dominant alignment of the C-N axes along [111] as has been shown by Rowe et al. /1/. Our neutron diffraction studies on single crystals at 293 and 185 K confirm these results.

Below 168 K it is assumed that the $(CN)^-$-molecules are frozen in with an uniform orientation along one of the face-diagonals [110]. In this low temperature modification KCN has on orthorhombic structure (space group: $I2/m\,2/m\,2/m$) /2/. By means of group-subgroup relations /3/ it can be shown (see figure) that the phase transformation at 168 K consists of two translationally equivalent transitions of index 3 and index 2, whereas the intermediate space group $I4/m\,2/m\,2/m$ belongs to a virtual phase. The reductions of symmetry associated with these transitions are compensated by the occurance of special domains.

$$F4/m\ \overline{3}\ 2/m\ (O_h^5)$$
(KCN at room temperature)

t3

$$F4/m\ 1\ 2/m \longrightarrow$$

| 4/m in [100]; |
| 1 in [111]; |
| 2/m in 110 |
| cubic notation |

with $a_1 \approx a_o/\sqrt{2}$; $c_1 \sim a_o$: $I4/m\ 2/m\ 2/m\ (D_{4h}^{17})$
(not represented)

| tetragonal notation |
| 4/m in [001]; |
| 2/m in [100]; |
| 2/m in [110] |

t2

$$I2/m\ 2/m\ 2/m\ (D_{2h}^{25}) \longrightarrow$$
(KCN at 120 K)

| orthorhombic notation |
| 2/m in [100]; |
| 2/m in [010]; |
| 2/m in [001] |
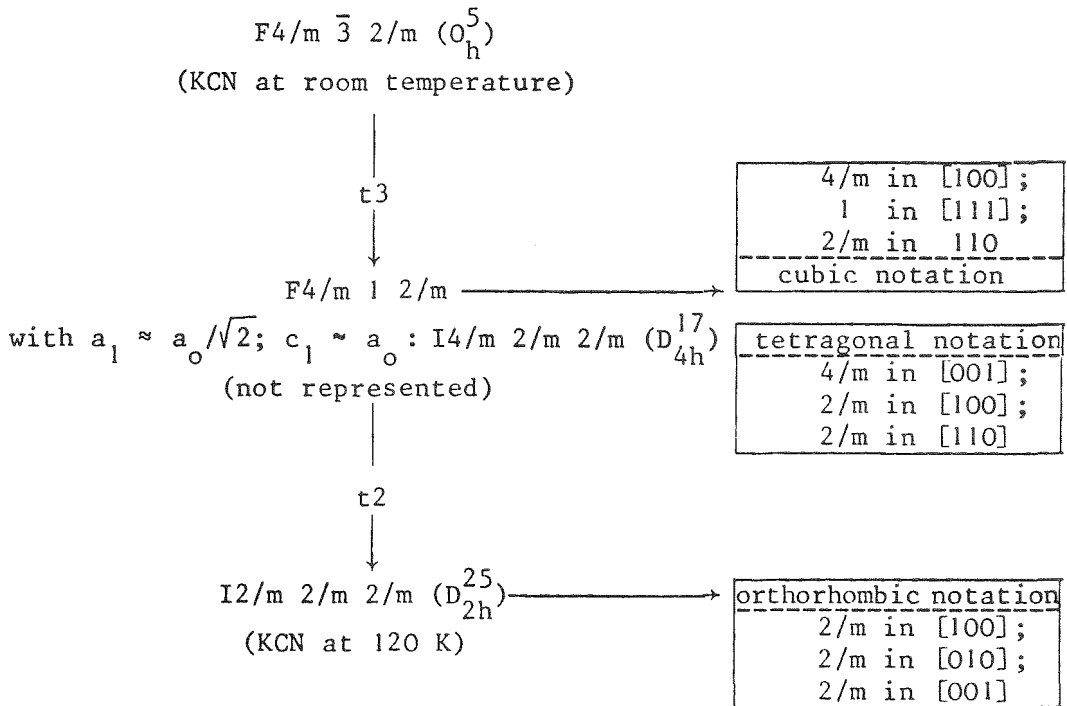
Fig.   Symmetry relations between the space groups of KCN

Corresponding to the product of the indices of symmetry reductions, up to 6 different oriented sections of a single crystal at higher temperatures may appear in the orthorhombic phase. Under uniaxial pressure in [OO1] the formation of domains due to F 4/m $\bar{3}$ 2/m $\overset{\rightarrow}{>}$ F 4/m 1 2/m can be suppressed. In this way only two domains (twins) remain in the orthorhombic modification of KCN. This prediction was confirmed by neutron diffraction measurements under uniaxial pressure at 120 K.

References

/1/ J.M. Rowe, D.G. Hinks, D.L. Price, S. Susman, and J.J. Rush, J. Chem. Phys. 58, 2039 (1973)

/2/ Structure Reports, 142 (1942 - 1944)

/3/ H. Bärnighausen, X. Int. Congr. Crystallography, (Amsterdam, 1975) Acta Cryst. A31, p. S3 (1975)

1.21 Untersuchung von Phasenumwandlungen in mit langsamem Zyklus zugdruckbe-
      lasteten Chrom-Nickel-Stahlproben mit Hilfe der Neutronenbeugung

      (Investigations on Phase-Transitions in Slow Cycle Tension-Compression
      Loaded Cr-Ni-Steel Specimens, Using Neutron Scattering)

V. Jung and K. Anderko[a]

[a] *IMF I, Kernforschungszentrum Karlsruhe GmbH*

Werden Chrom-Nickel-Stähle mit relativ niedrigem Ni-Gehalt (< 10 Gew.-%) einer sich langsam ändernden Zug-Druck-Belastung ausgesetzt, so treten unter bestimmten Bedingungen (z.B. Temperatur ca. 450°C, 1000 Lastwechsel, Verformungsgeschwindigkeit 10^{-5}/sec) Phasenumwandlungen von der austenitischen Phase (fcc) zur ferritischen α-Phase (bcc) auf. Daneben entsteht als Vorstufe die hexagonale ε-Phase /1/.

Bisher wurde bei 4 verschiedenen Proben nach den Reflexen der α-Phase gesucht. Bei einer Meßzeit von 1 - 3 Tagen pro Probe lag die Nachweisgrenze für den Gehalt an α-Phase bei 0.6 ‰. Die Ergebnisse sind in folgender Tabelle zusammengefaßt:

	Arbeitstemperatur	Verformungsgeschwindigkeit (sec^{-1})	Zahl der Lastwechsel	Konzentration der α-Phase
1. Probe M19	$550^{O}C$	$3 \cdot 10^{-5}$	300	$< 0.6 \cdot 10^{-3}$
2. Probe A141	$450^{O}C$	$3 \cdot 10^{-3}$	1500	$< 0.7 \cdot 10^{-3}$
3. Probe N8	$450^{O}C$	$3 \cdot 10^{-5}$	1000	$(1.3 \pm 0.6) \cdot 10^{-3}$
4. Probe A106	$20^{O}C$	$3 \cdot 10^{-3}$	3000	$< 0.7 \cdot 10^{-3}$

Anhand einer Probe mit 1000 Lastwechseln bei $450^{O}C$ und niedriger Verformungsgeschwindigkeit soll demnächst nach Umwandlungseffekten zur ε-Phase gesucht werden.

Literatur

/1/ D. Rousseau et al., Mémoires Scientifique Rev. Métallurg., LXVII, No. 5, 315 - 329 (1970)

1.22 Untersuchung von Gitterparameterabweichungen bei Stahl mit Hilfe der Neutronenbeugung

(Investigation on Lattice-Constant Variations in Steel Using Neutron Scattering)

V. Jung and W. Schmatz

Als Vorarbeiten zu Untersuchungen des Gitterparameters in Werkstücken aus Stahl in Abhängigkeit von der Materialtiefe wurden mit Hilfe eines Pulverspektrometers massive Proben verschiedener Stähle untersucht. Neben Unterschieden in den Gitterparametern ($\frac{\Delta a_O}{a_O} \approx 10^{-4}$), die wir auf unterschiedliche Legierungsbestandteile zurückzuführen, konnten bei einer oberflächengehärteten Probe Linienformveränderungen festgestellt werden, die auf Materialverspannungen in der gehärteten Schicht schließen lassen.

Der nächst Schritt der Arbeiten wird die Untersuchung einer im ganzen Volumen gehärteten Probe sein.

1.23 The Structure Factor and Pairpotential of Liquid Rubidium between 450 K
      and 1400 K

R. Block

Abstract

The structure factor $S(Q)$ of liquid rubidium has been measured for temperatures between 450 K and 1400 K and pressures up to 200 atm. The corresponding densities varied between 1.42 and 0.98 g cm^{-3}. The incident energy of the neutrons was 3.4 meV, the momentum transfer Q being $0.2 - 2.5$ Å^{-1}. A significant change in the order of the liquid has been registrated. Compressibility and electrical conductivity were derived from the structure factors and compared with the direct measured quantities, showing a good agreement. Further interpretation of the data was done by means of a hard core and a square well potential. Using these models it was already possible to get some information about the interaction between the rubidium atoms. A more exact calculation with a modified STLS model and a pseudopotential leads to a good description of the measured $S(Q)$. In order to describe at high temperatures $S(Q)$ for smaller values a new term had to be added to the pseudopotential.

2. T H E O R Y

2.1 Current-Current Correlations in α-AgI

W. Schommers

In a previous paper /1/ a vibrating-ion model was proposed for the description of correlations in space and time in superionic conductors. Molecular-dynamics calculations for α-AgI showed that this model gives a good description of structural and dynamical properties (structure factor and diffusion constant) in that solid. Furthermore, it was shown that (i) the vibrations of the I^--ions are clearly reflected in the structure and dynamics of the Ag^+ subsystem and, (ii) contrary to monoatomic liquids in α-AgI, relatively strong systematic correlations exist between the velocities of different ions. However, the single-particle motion (studied by the velocity autocorrelation function and the mean-square displacement) is in the first approximation similar to that in monoatomic liquids.

In this paper (see also Ref. 2) molecular-dynamics results of high accuracy will be presented for the current-current correlation function

$$\phi(t) = \frac{1}{e^2} \langle \vec{J}(o) \cdot \vec{J}(t) \rangle, \qquad (1)$$

where $\vec{J}(t)$ is the current of the system and e the ionic charge. $\phi(t)$ is an important quantity because it fully determines the frequency-dependent conductivity $\sigma(\omega)$, and we can learn something about the lifetime of correlations between the velocities of pairs of ions by means of current-current correlations. The figure shows $\phi(t)$ as a function of time.
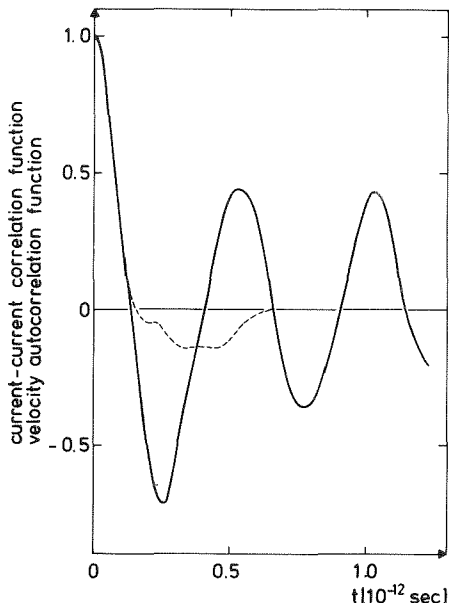
Fig.

Current-current correlation function and velocity autocorrelation function. Solid line: $\phi(t)/\phi(O)$; dashed line: $\psi_+(t)/\psi_+(O)$.

$\phi(t)$ has been calculated within the framework of the vibrating-ion-model (see Ref. 1). The statistical error in the calculation is less than 2.5 %. $\phi(t)$ and the velocity autocorrelation function for the Ag^+ subsystem

$$\psi_+(t) = \langle \vec{u}(o) \cdot \vec{u}(t) \rangle / \langle \vec{u}(o)^2 \rangle \tag{2}$$

agree well for $0 \le t \le 10^{-13}$ sec. For times greater than 10^{-13} sec, there is no point of similarity between the two curves. It can be seen that the oscillatory behaviour is less pronounced in $\psi_+(t)$ than in $\phi(t)$. This means that the forces acting on single ions are less important than those tending to reverse the total momentum of an ionic species. This effect reflects the tendency for local charge equilibrium to be maintained. Furthermore, the figure shows that the lifetime of velocity correlations is much shorter than that of current correlations, showing that there exist relatively long-lived correlations between the velocities of pairs of ions in α-AgI.

To obtain the frequency dependent conductivity $\sigma(\omega)$, we have to know $\phi(t)$ for much longer times than were possible to calculate; $\sigma(\omega)$ cannot be determined reliably from the molecular-dynamics results alone. In order to calculate $\sigma(\omega)$ by means of Eq. (1), we have to extrapolate the results for $t \ge 1.25 \cdot 10^{-12}$ sec. This cannot be made without additional assumptions on $\phi(t)$. Since the long-time behaviour is too uncertain, we were not able to draw $\sigma(\omega)$ from the molecular-dynamics results. The solution of this problem is to use very large systems. In the future, with larger computer memories and speeds, it will become possible to have precise numerical data to solve this question.

It should be mentioned that Hansen and McDonald performed molecular-dynamics calculations on molten NaCl /3/. They found that in molten NaCl the correlations between the velocities of pairs of ions are short lived. The reason why these correlations in α-AgI are long lived seems to be that the I^--subsystem is ordered (bcc lattice) and the iodine ions cannot diffuse. In molten NaCl both subsystem are disordered and all ions are mobile.

References

/1/ W. Schommers, Phys. Rev. Lett. 38, 1536 (1977)
/2/ W. Schommers, Phys. Rev. B17, 2057 (1978)
/3/ J.-P. Hansen, J.R. McDonald, J. Phys. C7, L384 (1975)

2.2   Extraction of Pair Potentials from the Pair Correlation Function:
      A Study for Liquid Gallium

W. Schommers

The determination of the effective inter-particle pair potential from
the observed pair correlation function g(r) is of considerable importance in
the theory of liquids. There are several theoretical attempts (selfconsistent
method /1/, Born-Green, Percus-Yevick, method by Ailawadi and Naghizadeh /2/,
etc.) to extract information about the pair potential from the knowledge
of g(r). In contrast to the simple-metal pseudopotential theory all these
methods are applicable without modifications to transition metals. We started
to test these methods for liquid gallium at 305 K using a structure factor
which has been measured with high accuracy by Narten /3/.

References

/1/ W. Schommers, Phys. Lett. A$\underline{43}$, 157 (1973)
/2/ N.K. Ailawadi and J. Naghizadeh, Solid State Commun. $\underline{20}$, 45 (1976)
/3/ A.H. Narten, J. Chem. Phys. $\underline{56}$, 1185 (1972)

2.3   A Non-Local Extension of the Gaspari-Gyorffy Theory for Superconductors

H. Rietschel

Abstract

We present a theory which extends the Gaspari-Gyorffy theory to include
non-local corrections within the framework of the spherical rigid muffin tin
approximation. We thereby construct an on-Fermi-sphere pseudopotential similar
to that of the simple free electron metals. We apply our theory to Al and NbC
for which $\alpha^2(\omega)$ and T_c are calculated. It turns out that for NbN the local
approximation works well whereas for Al non-local corrections are important.

2.4   Calculation of the Superconducting Transition Temperature in Refractory
      Compounds

H. Rietschel, W. Reichardt, G. Ries[a], and H. Winter[a]

[a]*Institut für Technische Physik, KfK*

Much theoretical effort has been undertaken to clarify the origins of high
T_c superconductivity in the refractory compounds (RC). In particular, interest
has focussed on the empirically found correlation between high T_c-values and
the observation of phonon anomalies /1, 2/. In order to calculate T_c, several
authors applied the Gaspari-Gyorffy (GG)-theory to the RC, thereby attaining
rather good agreement between theory and experiment /3, 4/. In these papers the
GG-theory has been used in local approximation providing λ in the form

$$\lambda = \sum_\alpha \frac{\eta_\alpha}{M_\alpha <\omega^2>}$$ (1)

In Eq. (1) η_α denotes the scattering power of the α-th atom in the unit
cell and $<\omega^2>$ is a mean squared phonon frequency. Whereas the electronic quan-
tities η_α nowadays are calculated with considerable care usually rather crude
estimates are used for $<\omega^2>$. Since T_c depends exponentially on λ the un-
certainty in $<\omega^2>$ renders any quantitative result based upon this approach
dubious.

Here we present calculations of T_c for the compounds ZrC, YS, NbC and NbN
where the phonons are treated on the same level of accuracy as the electrons.
To this end we used a non-local extension of the GG-theory /5/ to calculate the
Eliashberg function $\alpha^2(\omega)F(\omega)$. T_c was determined by solving the Eliashberg
equations numerically using the program of /6/. For all examples the Coulomb
repulsion μ^* was assumed to be 0.13.

As a model for the lattice dynamics we chose the double shell model of
Weber /7/ which presently provides the most reliable phonon frequencies and
amplitudes in the RC. The electronic quantities were obtained using a cluster
approach based on the Lloyd formalism. A short outline of it can be found in
/8/ where it has been applied to Th_4H_{15}.

In the table our theoretical values for T_c are given together with λ
decomposed in acoustical and optical contributions. References for the shell

	T_c^{th}	T_c^{exp}	T_c^{ac}	λ	λ_{ac}	λ_{opt}	Ref.
ZrC	0	0	0	.24	.12	.12	[7]
YS	4.1	3	1.5	.61	.49	.12	[11]
NbC	8.6	11	2.1	.64	.47	.17	[7]
NbN	15.4	16	7.8	.98	.78	.20	[12]

model used are given in the last line. The deviations of the theoretical T_c's from experiment are of the order of 30 % or less. For a superconductor with $\lambda \sim 0.7$, $\mu^* \sim 0.13$ and $T_c \sim 10$ K (e.g. NbC) this can be traced back to an uncertainty in λ of about 10 %. This is as good as can be expected in view of the arbitrariness in fixing μ^* and in view of possible computational inaccuracies. Within these error limits our theoretical T_c-values may lie systematically to low as a consequence of the omission of the resonance mechanism proposed in /2/. On the other hand it is evident that coupling of electrons to optical phonons plays an important role for T_c in the RC, a fact which already has been stated in /9/. This is clearly shown by the third column of the table which lists the T_c-values obtained by omitting the optical parts in $\alpha^2(\omega)F(\omega)$. Thus, we believe that the key to the high T_c of some of the RC lies in their increased atomic density resulting in additional vibrational degrees of freedom and an overall increase of the η_α. (For free electrons η can be shown to be $\eta \sim V^{-4/3}$, where V is the atomic volume. For transition metals, this relation is preserved as a trend /10/.) Our assumption is supported by the results for YS. The volume of the unit cell in YS is about twice that in NbC. In spite of its pronounced phonon anomalies /11/, YS has a low T_c (~ 3 K).

References

/1/ H.G. Smith, W. Gläser, Phys. Rev. Lett. 29, 353 (1972)

/2/ W. Hanke, J. Hafner, H. Bilz, Phys. Rev. Lett. 37, 1560 (1976)

/3/ B.M. Klein, D.A. Papaconstantopoulos, L.L. Boyer, Proc. of the Sec. Roch. Conf., Plenum, N.Y. (1976)

/4/ K. Schwarz, P. Weinberger, J. Phys. C8, L573 (1975)

/5/ H. Rietschel, in Prog. Rep. Teilinst. Nukl. Festkörperphysik, Ges. f. Kernforschung, KFK 2538 , 74 (1977); Z. Physik, in print

/6/ G. Bergmann, D. Rainer, Z. Phys. 143, 59 (1973)

/7/ W. Weber, Phys. Rev. B8, 5093 (1973)

/8/ H. Winter, G. Ries, Z. Phys. B24, 279 (1976)

/9/ H. Rietschel, Z. Phys. B22, 133 (1975)

/10/ W.H. Butler, Phys. Rev. B15, 5267 (1977)

/11/ P. Roedhammer, W. Reichardt, F. Holtzberg, Phys. Rev. Lett. 40, 465 (1978)

/12/ W. Reichardt, private communication

2.5   Electronic Densities of States and Superconductivity in YB_6

G. Schell, G. Ries[a], and H. Winter[a]

[a]*Institut für Technische Physik, KfK*

The hexaborides of La and Y have been found to be superconductors with critical temperatures T_c of .45 and 7.1 K, respectively /1/. This great discrepancy in the T_c's cannot be accounted for by considering only the differences in the values of electronic quantities emerging from the band structure calculation of /2/ which makes use of a variation method.

It therefore seems desirable to evaluate electronic properties by means of the cluster method /3/ which is able to give all the electronic quantities needed in /4/ to calculate the Eliashberg function $\alpha^2(\omega) \cdot F(\omega)$, the electron mass enhancement factor λ, and, from these, T_c. Furthermore this method is more appropriate to include the coupling to the lattice vibrations.

In a first step we have calculated phaseshifts and partial densities of states in YB_6, the potential of which has been approximated by that of a cluster containing up to 27 Y-atoms and 120 B-atoms; a local exchange term has been used. Our density of states differs significantly from that obtained by /2/. This difference is due to three facts:

i)   /2/ use only a limited set of basis functions built up from atomic orbitals, whereas we use a linear combination of angular momentum eigenfunctions within the muffin-tin-radii, the corresponding radial part of the wavefunctions being calculated exactly. The values of the phaseshifts indicate that it is sufficient to consider only angular momenta up to $l = 1$ (B) and $l = 2$ (Y).

ii)   The bandstructure of /2/ is calculated at only 18 inequivalent k-points within the Brillouin zone, which results in an error in the density of states, whereas we obtain the density of states in configuration space directly.

iii)   /2/ use an aspherical potential obtained by superposition of spherical atomic potentials but do no selfconsistent calculations. We consider the effects caused by nonspherical contributions to the potential negligible in comparison with effects resulting from a fully self-consistent calculation, since a charge transfer from the Y-atoms to

the sublattice of the B-atoms is expected /5/ and found in our calculations with a corresponding shift of the energy levels.

In the selfconsistent calculations we started from a spherical superposition of atomic potentials. Within the muffin-tin-radii we obtained the partial densities of states which, via the Poisson-equation, yielded a new potential. After mixing a certain fraction ($\sim$ .4) of the new potential to the old one the whole procedure was repeated. The algorithm needed typically 8 iterations until convergence was reached, that means the input and output potentials were then the same within less than 1 per cent. Making use of the full rotational symmetry of YB_6 (cubic-O_h) we were able to reduce the CPU-time per iteration to 10 min on the IBM 370-168, dealing with the forementioned cluster size.

In order to account better for the low lying energy levels we now take care of the atoms outside the cluster by embedding the cluster in a surrounding medium with constant negative potential. This improvement is now being added to our program, the results of which are expected to give electronic quantities with sufficient accuracy in order to describe well the superconducting properties of YB_6.

References

/1/ J.M. Vandenberg, B.T. Matthias, E. Corenzwit, H. Barz, Mat. Res. Bull. 10 889 (1975)

/2/ P.F. Walch, D.E. Ellis, F.M. Mueller, Phys. Rev. B15, 1859 (1977)

/3/ B.L. Gyorffy, M. Stott, Proc. of the Internat. Conf. of Band Structure Spectroscopy of Metals and Alloys, London (1968)

H. Winter, G. Ries, Z. Phys. B24, 279 (1976)

G. Ries, H. Winter, to be published

/4/ I.R. Gomersall, B.L. Gyorffy, J. Phys. F4, 1204 (1974)

H. Rietschel, Z. Phys., in print

/5/ H.C. Longuet-Higgins, M. de V. Roberts, Proc. Roy. Soc. (London) A224, 336 (1954)

2.6 Interchain Ordering and Phonon-Anomaly in a Peierls-System

K. Käfer

Let us consider a quasi-one-dimensional system of Peierls-distorted chains. The background charge density is given by

$$\rho(\underline{r}) = \sum_{R_\perp} \delta(r_\perp - R_\perp) \ \rho_0\{1 + \delta\sin(2k_F z + \phi_{R_\perp})\}$$

$R_\perp$ is the chain-position vector. δ is the relative amplitude of the charge-density wave, $2k_F$ its period, and $\phi_{R_\perp}$ denotes the phase of the Peierls-superstructure on chain $R_\perp$. (By $r_\perp$ etc. we denote 2-vectors (r_x, r_y) etc..) As is well-known /1/, such quasi-one-dimensional systems tend to develop a pronounced $2k_F$ phonon-anomaly. Our aim is to investigate what influence the distribution of super-structure phases $\phi_{R_\perp}$ has on this anomaly. We used the random-phase approximation. A typical polarization diagram appearing in the phonon renormalization series is shown in Fig. 1.

With the electronic wave-function ($k_z > 0$)

$$\psi_{\underline{k}}(\underline{r}) = \frac{1}{\sqrt{N_\perp}} \sum_{R_\perp} \{A_{k_z} e^{ik_z z} + B_{k_z} e^{-i\phi_{R_\perp}} e^{i(k_z - 2k_F)z}\} e^{ik_\perp R_\perp} L(|r_\perp - R_\perp|)$$

where $L(|r_\perp - R_\perp|)$ describes the localization of the electrons to the vicinity of the $N_\perp$ chains, and A_{k_z}, B_{k_z} are k_z-dependent mixing coefficients due to the Peierls-superstructure, such a diagram can be written as
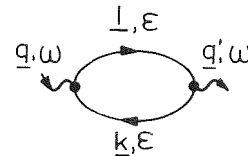
Fig. 1

RPA-polarization diagram

$$\Pi(\underline{q}, \underline{q}') = \pi(q_z, q_z') \cdot H(\underline{q} - \underline{q}'), \qquad \text{with}$$

$$H(\underline{q} - \underline{q}') = \frac{1}{N_\perp} \sum_{R_\perp} e^{i(q_\perp - q_\perp')R_\perp} e^{i\frac{q_z' - q_z}{2k_F}\phi_{R_\perp}}$$

$\pi(q_z, q_z')$ contains the polarizability of the one-dimensional electron gas. q_z' can take the values $q_z \pm \mu 2k_F$, $\mu = 0, 1, 2$. The normal diagram ($q_z' = q_z$) leads to the giant Kohn-anomaly at $q_z = \pm 2k_F$ /1/. The anomalous diagrams $q_z' = q_z - 4k_F \ \text{sign} \ q_z$ and $q_z' = q_z - 2k_F \ \text{sign} \ q_z$ lead at $q_z = \pm 2k_F$ to a gap in the phonon-dispersion and to infrared-activity of the phase-mode, respectively /2/. The second, ϕ-dependent factor $H(\underline{q} - \underline{q}')$ determines the $q_\perp'$-selection rules.

We consider two limiting cases

a) Perfect ordering of superstructure-phases: for $\phi_{R_\perp} = Q_\perp R_\perp \equiv Q_x R_y + Q_y R_y$
we get

$$\Pi(\underline{q},\underline{q}') = \pi(q_z,q_z') \, \delta_{\underline{q}',\underline{q} \pm \mu(Q_x,Q_y,2k_F)} \quad ; \qquad \mu = 0, 1, 2$$

Normal and anomalous diagrams contribute fully and we have the dispersion shown in Fig. 2a) /2/.

b) Statistical distribution of superstructure-phases: we make the following simplifying Ansatz:

$$P_\phi(R_\perp) = \frac{1}{\sqrt{\pi}\,\sigma\,R_\perp} \; e^{-\frac{\phi^2}{\sigma^2 R_\perp^2}}$$

The deviation ϕ of the phase on a given chain from its ordered value (taken here as $\phi_{R_\perp} \equiv 0$ for all chains) obeys a probability distribution whose width depends on the chain's distance from a reference chain at the origin. In an averaged typical RPA-diagram every pair bubble is then associated with

$$\langle H(\underline{q}-\underline{q}')\rangle = \frac{1}{N_\perp} \sum_{R_\perp} e^{i(q_\perp - q_\perp')R_\perp} \; e^{-\frac{\sigma^2}{4}\left(\frac{q_z'-q_z}{2k_F}\right)^2 R_\perp^2}$$

While normal processes ($q_z' = q_z$) are independent of the degree of ordering the anomalous terms vanish as we approach complete randomness in the phase-distribution ($\sigma \to \infty$). This means a) the gap in the phonon-dispersion should disappear (Fig. 2b)), b) the infrared-activity of the phase-mode should vanish.
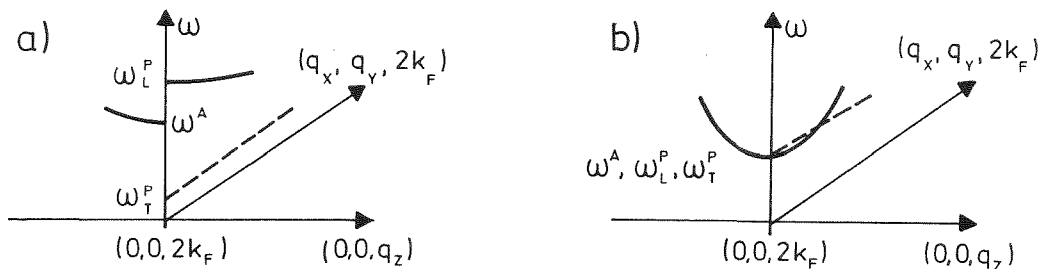
Fig. 2 Phonon dispersion a) with b) without contributions from anomalous diagrams
(ω_T^P, ω_L^P: "transversal" and "longitudinal" phase-mode, respectively; ω^A: amplitude-mode)

This demonstrates that the transition from ordered to random superstructure-phases has a profound effect on the $2k_F$-phonons. We find that the phonons themselves are changed, not only the relative weight with which they enter the neutron scattering law, as was stated elsewhere /3/, and we do not expect infrared-activity from the phase mode for a random phase-distribution either.

Optical /4/ and neutron scattering /5/ experiments on the quasi-one-dimensional substance KCP, where the Peierls-phases are randomly distributed at room temperature and correlated with a typical length of 5 to 8 interchain distances for T < 80 K /6/, are in good agreement with the above theoretical results /7/.

References

/1/ W. Kohn, Phys. Rev. Lett. 2, 393 (1959)

/2/ P.A. Lee, T.M. Rice, and P.W. Anderson, Solid State Commun. 14, 703 (1974)

/3/ P.A. Lee and H. Fukuyama, Phys. Rev. B17, 542 (1978)

/4/ P. Brüesch, S. Strässler, and H.R. Zeller, Phys. Rev. B12, 219 (1975)

/5/ B. Renker, private communication

/6/ J.W. Lynn, M. Iizumi, G. Shirane, S.A. Werner, and R.B. Saillant, Phys. Rev. B12, 1154 (1975)

/7/ K. Käfer, Kernforschungszentrum Karlsruhe, KFK 2630 (1978), and to be published

2.7 On the Electronic Structure of $Ti_{10}Te_8$

H. Nohl

Using the linear muffin-tin-orbital method in the atomic-sphere approximation, we started to calculate the electronic bands of $Ti_{10}Te_8$, which belongs to an extensive class of compounds with the same or similar structure /1/. In a sense, the crystal structure of $M_{10}X_8$ (M = Ti, Nb, Mo, Ta, W and X = Se, Te, As, Sb) resembles that of Chevrel-phase high-critical-field superconductors /2/: it can be discussed in terms of well-known M_6X_8 building blocks forming a chain of corner-linked M octahedra, where the M atoms are placed near the face centers of an approximately cubic arrangement of X atoms. Furthermore, the chains are parallel and ordered such that the M atoms of each octahedron basis get an additional X-ligand from neighbouring chains. In order to get more insight into the stability of the M octahedra preliminary non-selfconsistent bandstructure calcula-

tions for a Ti_5Te_8 chain were performed. This chain is a Ti_5-octahedron-chain surrounded by its nearest neighbours. As a first step we computed the Ti 3d bands, neglecting the mixing with all other bands, and found the 25 Ti d sub-bands are seperated into a number of narrow bands. This indicates a weak in-trachain d-d coupling. Simple analytical expressions can be given for the wavefunctions in the middle of the Brillouin-zone and the bands in the tight-binding approximation. The effect of hybridization with the Ti 4s states and the covalent mixing with the 5s and 5p states of the intra- and interchain Te atoms is studied for a wide range of energy dependent potential functions describing the outgoing scattering of the spherically symmetric part of the potentials. We found the 8 Te s and 24 Te p bands placed below the Ti d bands, four of the Ti s bands are well above the top of the d bands and a strong hybridized broad Ti s band crosses the d-bands. In contrast to the electronic structure of the Chevrel-phase /3/ no gap was found in the transition metal d band, which in the former compounds is responsible for the binding of the isolated octahedra. With the assumption that Te acts as a divalent anion, the number of bonding electrons per Ti_5Te_4 unit is 12 and the Fermi level is placed below a pronounced peak in the density of states. Further selfconsistent cal-culations are under progress.

References

/1/ F. Gvønvold, A. Kjekshus, and F. Raaum, Acta Cryst. 14, 930 (1961)
    H. Schaefer and H.G. v. Schnering, Angew. Chem. 20, 833 (1964)

/2/ R. Chevrel, M. Sergent, and J. Prigent, J. Solid State Chem. 3, 515 (1971)

/3/ O.K. Andersen, W. Klose, and H. Nohl, Phys. Rev. B17, 1209 (1978)

3. ELECTRONIC STRUCTURE AND MAGNETISM OF SOLIDS

3.1 On the Origin of the Large Positive Hyperfine Field at ^{61}Ni-Nuclei in PdNi and PdNiFe Alloys

J. Fink, G. Czjzek, H. Schmidt, and F.E. Obenshain[a]

[a]*Oak Ridge National Laboratory, Oak Ridge, Tenn. 37830, U.S.A.*

Magnetic hyperfine fields at Co and Ni nuclei in dilute PdNi alloys have large positive values, $\sim + 260$ kOe   and $\sim + 180$ kOe respectively, whereas Fe in Pd as well as Fe and Co in Pt experience negative magnetic hyperfine fields. The origin of the large exceptional positive hyperfine fields is not well understood. In several investigations /1/ devoted to this problem this large positive hyperfine field was ascribed to the existence of large orbital moments ($\sim 0.5 \mu_B$) at the Co and Ni atoms in a Pd-matrix.

We have measured the magnetic hyperfine field at Ni nuclei in dilute $Pd_{1-x}Ni_x$ alloys in the range $0.005 \leq x \leq 0.1$ and in a $Pd_{.983}Ni_{.015}Fe_{0.002}$ alloy by ^{61}Ni-Mössbauer spectroscopy in external fields up to 50 kOe and in the temperature range 1.1 to 140 K. In addition, we have measured the magnetic susceptibility of the samples in the same temperature range and in magnetic fields up to 60 kOe using a Faraday balance.

At all concentrations we see a distribution of hyperfine fields and not a single component. To compare our hyperfine fields with the bulk magnetization, we take the averages of this distribution. In the figure we show the average Knight shift $(<H_{hf}> - H_{ext})/H_{ext}$ in dependence of the local susceptibility of the Ni-atoms $\Delta\chi = \chi_{alloy} - \chi_{Pd}$, extracted from the bulk magnetization measurements. The concentration and the temperature are inherent parameters in this representation. The data clearly show that the Knight-shift is not proportional to the local susceptibility at the Ni atoms. At high temperatures, corresponding to low local susceptibilities, a Knight-shift of 20 % remains, which can be attributed to the hyperfine field caused by neighbouring Pd-atoms magnetized by the external field. From the known susceptibility of Pd, a hyperfine field constant $H_{hf}/\mu_{Pd} = 2000$ kOe/μ_B can be calculated. Thus our data show that the magnetization of Pd-atoms in the neighbourhood of Ni atoms leads to a positive

hyperfine field at the Ni nuclei. With increasing local susceptibility of the Ni atoms the Knight-shift is also increasing and we obtain a hyperfine constant of H_{hf}/μ_{Ni} = 50 kOe/μ_B. As we know that the Pd atoms in the first coordination shell give a positive H_{hf}, this positive Knight-shift is the result of Pd-atoms which are polarized by the field-induced Ni-moments. From neutron scattering experiments we can extract that a Ni moment of 1 μ_B leads to a Pd polarization of about 0.03 μ_B in the first coordination shell, and this leads with H_{hf}/μ_{Pd} = 2000 kOe/μ_B to a hyperfine constant H_{hf}/μ_{Ni} = 60 kOe/μ_B. This result is quite close to the experimental value 50 kOe/μ_B. Small differences may be explained by a negative contribution to the hyperfine field caused by the core polarization due to the induced 3d moment in Ni.

There are additional informations from our measurements which confirm our interpretation of the large positive magnetic hyperfine fields at the Ni nuclei in PdNi alloys: if there were an orbital moment of 0.5 μ_B at the nickel atom, we should find a quadrupole interaction between the nuclear quadrupole moment Q and the electric field gradient V_{zz} : $eQV_{zz} \approx 1 \cdot 10^{-7}$ eV. In the Mössbauer spectra, we do not find any indication of a quadrupole interaction. The upper limit of the value compatible with our spectra is $eQV_{zz} \approx 5 \cdot 10^{-9}$ eV. Finally, the distribution of the magnetic hyperfine fields is not independent of the Ni concentration, as quoted by /1/. In the paramagnetic range, our spectra can be described by two components with different magnetic hyperfine fields. The high field component results from those Ni atoms, which are in the polarization clouds of magnetic clusters with at least 3 Ni atoms. In the $Pd_{0.983}Ni_{0.015}Fe_{0.02}$
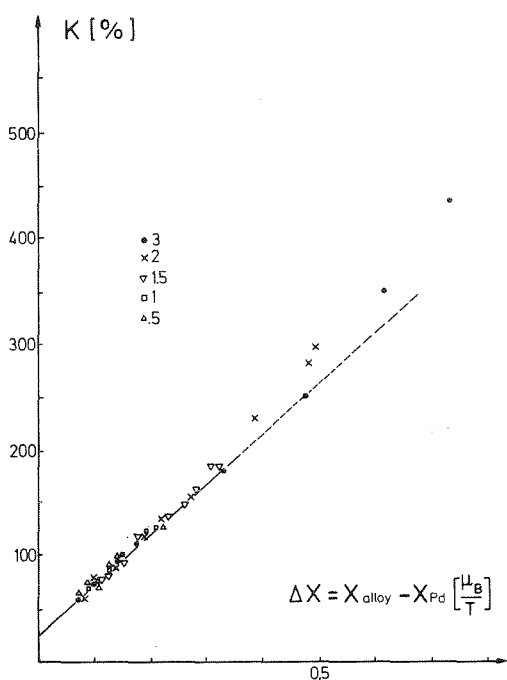
Fig.

Knight shift at ^{61}Ni nuclei in $\underline{Pd}$Ni alloys with c_{Ni} = .5, 1, 1.5, 2, and 3 at% in dependence of the susceptibility per Ni atom $\Delta\chi = \chi_{alloy} - \chi_{Pd}$

- 58 -

alloy we find a similar result. There the high field component is due to Ni-atoms inside the polarisation cloud of an Fe atom. Thus the information deduced from the distribution of magnetic hyperfine fields also shows that the Pd magnetization in giant moments leads to large positive magnetic hyperfine fields.

Reference

/1/ M. Katayama, K. Kumagai, T. Kohara, K. Asayama, I.A. Campbell, N. Sano, S. Kobayashi, Journ. Phys. Soc. Japan 40, 429 (1976)

Le Dang Khoi, P. Veillet, and I.A. Campbell, J. Phys. F6, L197 (1976)

3.2   Magnon Dispersion in Ordered $Ni_{0.75}Mn_{0.25}$

P.v.Blanckenhagen and B. Scheerer

The nickel manganese system provides a good example for studying the effects of atomic order-disorder on the magnetic properties /1/. The saturation moment of the ferromagnetic disordered alloys rises from that of pure Ni with increasing Mn concentration up to a maximum of 0.8 μ_B per atom at about 10 % Mn, then it decreases very rapidly to about 0.1 μ_B per atom at about 25 % Mn. By annealing treatment of alloys near the composition Ni_3Mn the saturation moment may be increased up to 1.1 μ_B and the Curie temperature from about 100 K to 723 K. In the disordered ferromagnetic alloy atomic and magnetic short range order has been detected by neutron scattering experiments /2/, /3/. Two types of models have been developed for the description of the magnetic properties of these alloys: Heisenberg models with localized moments and band models /4/. Detailed information on the effects of the electronic structure on the magnetic properties can be derived from the spin wave stiffness constant D /5/.
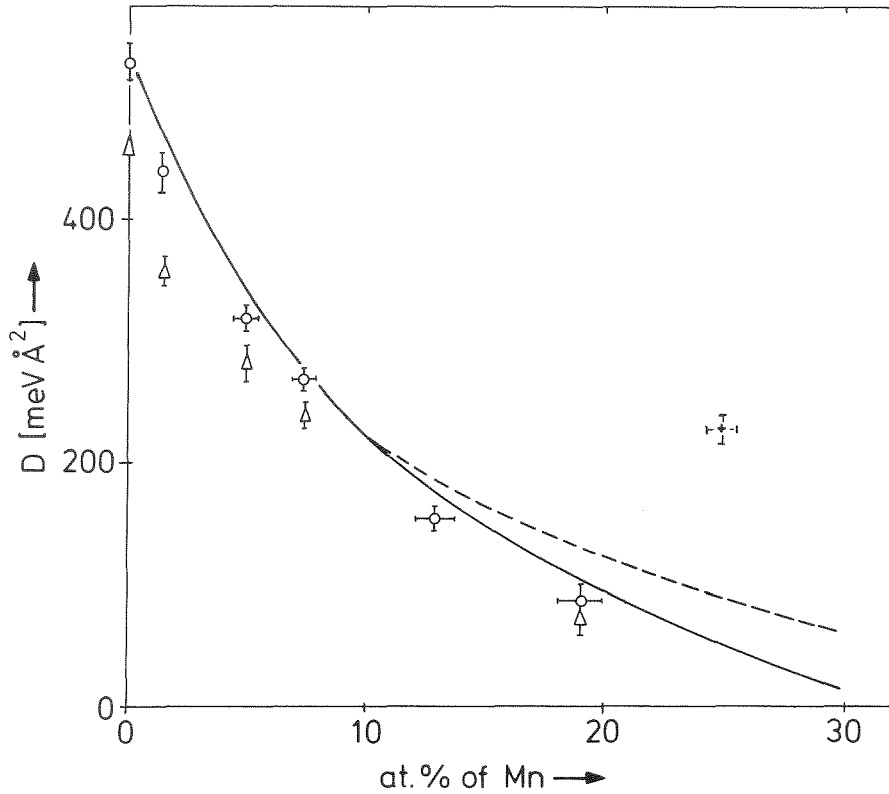
Fig. 1 Concentration dependence of the spin wave stiffness constant D of NiMn alloys

+ D for annealed $Ni_{0.75}Mn_{0.25}$

△ at room temperature

o at 4.2 K

Calculated D in a CPA-model with (——) and without (---) local environment effect.
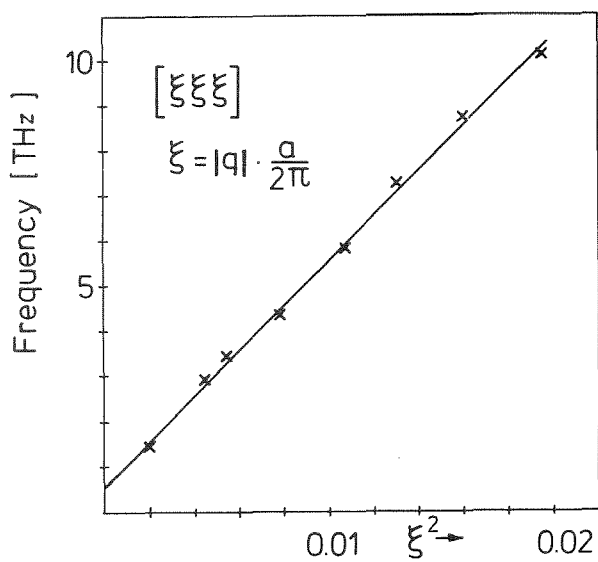
Fig. 2 Magnon dispersion relation measured in [111] direction in a $Ni_{0.75}Mn_{0.25}$-crystal at room temperature

In previous work D was measured for a disordered crystal with 13 % Mn
in cooporation with B. Hennion and coworkers (CEN-Saclay) /4/. For the
disordered alloys D decreases monotonously with increasing Mn-content /4/
(Fig. 1). A description of this concentration dependence of D as well as
of the saturation moment was possible by a CPA-band model under consideration
of local environment effects /4/.

To study the effect of the disorder-order transition on the stiffness
constant we have now determined the magnon dispersion relation for a
partially ordered $Ni_{0.75}Mn_{0.25}$ crystal. The crystal was grown by annealing
a polycrystalline sample near the melting point /6/. Partial ordering (long range
order parameter S $\sim$ O.8) was achieved by annealing the sample for 250 hours at 689 K.

The measurements of the magnon dispersion curve were made at room tem-
perature on the triple-axis-spectrometer TAS1 at the FR2 Karlsruhe. The di-
spersion relation is shown in Fig. 2, it may be described by a quadratic law
with a stiffness constant D = (225 ± 13) meV $Å^2$ and a gap at q = O of
approximately 2 meV. The value for D is larger by a factor of about 4 than
the value expected for this concentration in the disordered state (Fig. 1).

References

/1/ J.S. Kouvel in "Magnetism and Metallurgy", Vol. 2, 523 (1969)

/2/ J.W. Cable and H.R. Child, Phys. Rev. B10, 4607 (1974)

/3/ P.v.Blanckenhagen and Chr. v. Platen, in Prog. Rep. Teilinst. Nukl. Fest-
körperphysik, Ges. f. Kernforschung, KFK 2183, 51 (1975)

/4/ B. Hennion et al., in Proc. of the IAEA Conference on Inelastic Neutron
Scattering, Vienna (1977)

/5/ D.M. Edwards and D.J. Hill, J. Phys. F6, 607 (1976)

/6/ B. Scheerer in Prog. Rep. Teilinst. Nukl. Festkörperphysik, Ges. f.
Kernforschung, KFK 2183, 51 (1975)

3.3   Spin Relaxation in Manganese Aluminosilicate Glass

W. Nägele[a] and P.v.Blanckenhagen

[a]Institut für Kristallographie, Universität Tübingen

Manganese aluminosilicate glass of the chemical composition $Al_2Mn_3Si_3O_{12}$
has spin glass properties at low temperatures: the ac-susceptibility exhibits
a cusp at 2.4 K, whereas there is only a small hump in the specific heat.

The susceptibility cusp is smoothed by application of an external magnetic
field of some hundred oersteds /1, 2, 3/.   The magnetic properties of
these garnet glasses are due to direct Heisenberg-exchange and superexchange
interactions. Due to these interactions magnetic short range order exists
even at relatively high temperature /4/. The magnetic structure factor at
different temperatures can be described in terms of a shell model in which
one reference spin is correlated with the spins of two or three neighbour
shells /4/.

To get informations about the spin-dynamics in this glass we have performed
inelastic neutron scattering experiments. The measurements were done on the MAG2
spectrometer at the FR2 with a primary neutron energy of 3.55 meV and at tempera-
tures between 5.8 and 295 K. We observed quasi-elastic scattered intensity below
the elastic line (Fig. 1) but no peaks in the inelastic region of the spectra as
an indication for collective magnetic excitations. The scattering law $S(Q,\omega)$ at
constant Q may be interpreted in terms of an elastic Gaussian line (coherent
scattering due to static nuclear and magnetic correlations and nuclear incoherent
scattering) and a Lorentzian line which indicates spin relaxation processes
(Fig. 1). This Lorentzian $f(Q,\omega) = \Gamma/\pi \cdot (\Gamma^2 + \omega^2)^{-1}$ involves the relaxation time
$\tau = 1/\Gamma$. In lowering the temperature from 295 K to 5.8 K, we observed an increase
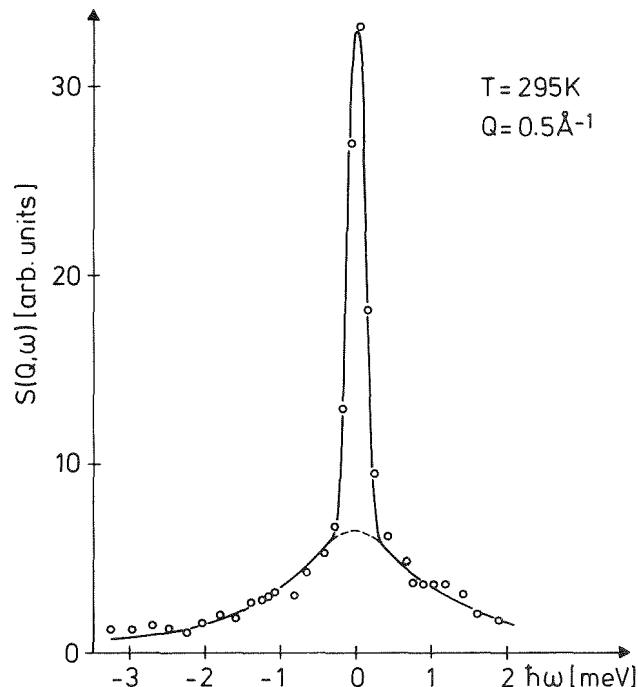
Fig. 1   Measured magnetic and nuclear scattering law at constant Q (ooo) and
          result of a least square fit (———).

of the relaxation time. At high temperatures the linewidth behaves as $\Gamma = \Lambda Q^2$
(Λ = spin diffusion constant) for small Q and it is independent of Q at large
Q (Fig. 2). At low temperatures the linewidth shows no significant Q dependence.
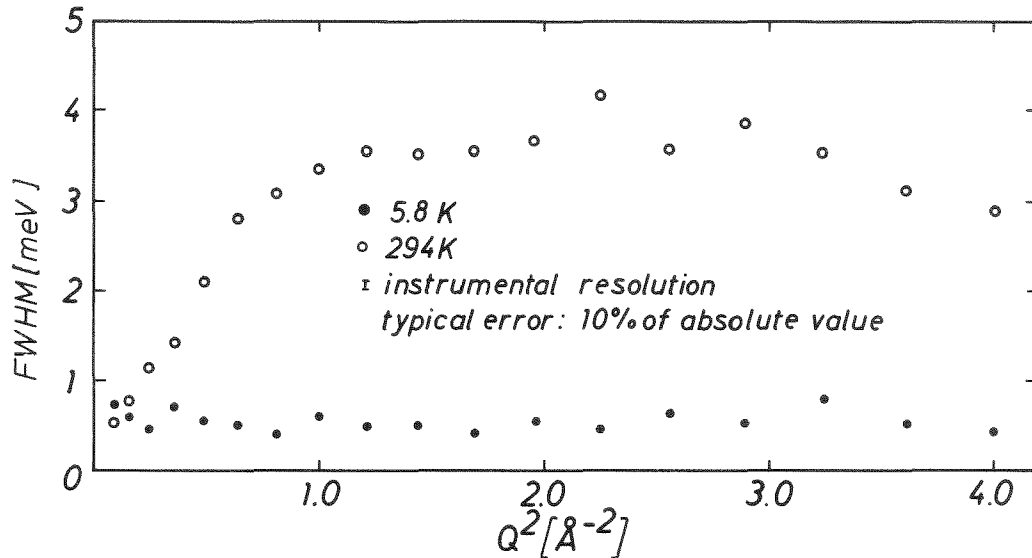
Fig. 2   Q-dependence of the linewidth ($\hat{=} 2 \, \Gamma$)

References

/1/ R.A. Verhelst, R.W. Kline, A.M. de Graaf, and H.G. Hooper, Phys. Rev. B11,
    4427 (1975)

/2/ R.W. Kline, A.M. de Graaf, L.E. Wenger, and P.H. Keesom, AIP Conference
    Proceedings 29, 169 (1975)

/3/ J.-P. Renard, J. Pommier, J. Ferre, and K. Knorr, to be published

/4/ W. Nägele, K. Knorr, W. Prandl, P. Convert, and J.L. Buevou, J. Phys. C,
    in press

3.4 Investigation of the Magnetic Phase Diagram of the Intermetallic System
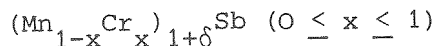
$(Mn_{1-x}Cr_x)_{1+\delta}Sb$ $(0 \leq x \leq 1)$

W. Reimers[a], E. Hellner[a], W. Treutmann[a], and G. Heger

[a]Fachbereich Geowissenschaften der Universität Marburg

The magnetic phase diagram of the system $(Mn_{1-x}Cr_x)_{1+\delta}Sb$ $(0 \leq x \leq 1)$ - proposed from neutron powder diffraction studies /1/ - has been reinvestigated with single crystals. The main interest was to study the transition from ferro- magnetic (MnSb) to antiferromagnetic (CrSb) behaviour of the pure end members. $(Mn_{1-x}Cr_x)_{1+\delta}Sb$ $(\delta \lesssim 0.1)$ crystallizes in a NiAs-type structure (space group $P6_3/mmc$ - Fig. 1). Single crystals of the intermetallic compounds were grown by the Bridgman-Stockbarger-method /2/. The samples were characterized by means of combined X-ray and neutron diffraction /2/. The evaluation of the X-ray data yields the 2(a) and 2(c) site occupancies (δ_{2a}, δ_{2c}-values). The Cr:Mn ratios of the individual crystals were determined from neutron diffraction analyses at high temperatures in the paramagnetic region. The overall compositions so obtained were checked for selected samples by means of atomic absorption spectra.
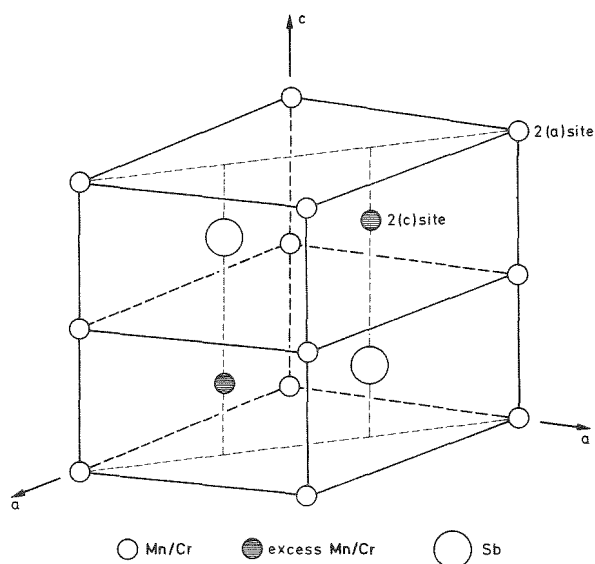
Fig. 1   Unit cell of NiAs-type structure

By temperature dependent neutron diffraction the various magnetic arrangements and transition temperatures have been studied for selected compositions. In Fig. 2 our results so far are added to the magnetic phase diagram for MnSb-CrSb given by Takei, Cox and Shirane /1/. The magnetic system $(Mn_{1-x}Cr_x)_{1+\delta}Sb$ ($0 \le x \le 1$) seems to be completely mixable in contradiction to $(Cr_{1-x}Fe_x)_{1+\delta}Sb$ ($0 \le x \le 1$), where an intermediate phase of spin glass type was found /3/. Between the regions with pure ferromagnetic (MnSb) and antiferromagnetic interactions (CrSb) there exists an intermediate phase characterized by canted moment orientation.
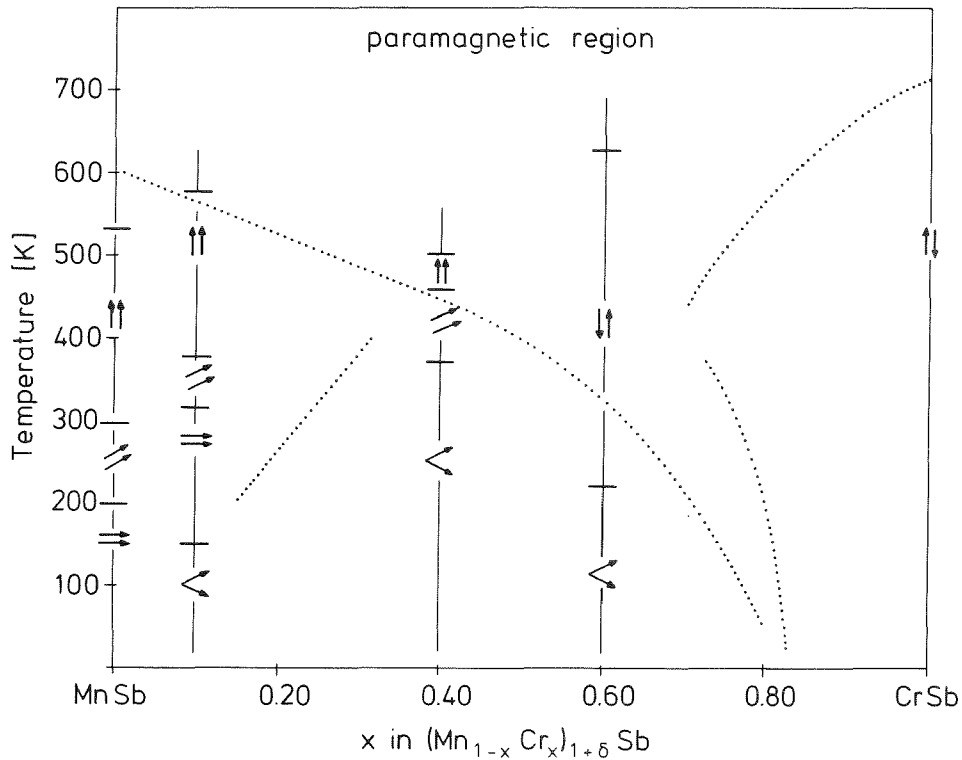
Fig. 2   Magnetic phase diagram of MnSb - CrSb

The dotted lines show the transition temperatures given by Takei et al. /1/

The magnetic ordering from our single crystal studies on $(Mn_{1-x}Cr_x)_{1+\delta}Sb$ with c = 0.0;0.10;0.40;0.60 is characterized by:

↑↑ - ferromagnetism, spin orientation ‖ c
⤢ - ferromagnetism, spin direction turned out of c
⇄ - ferromagnetism, spin-orientation ⊥ c
⦛ - weak ferromagnetism, canted spin arrangement
↓↑ - antiferromagnetism, spin orientation ‖ c

References

/1/ W.J. Takei, D.E. Cox, and G. Shirane, Phys. Rev. 129, 2008 - 2018 (1963)

/2/ G. Heger, E. Hellner, D. Mullen, and W. Treutmann, Conference on Neutron Scattering, Gatlinburg 1, 71 (1976)

/3/ J. Nösselt, unpublished results

3.5   Magnetic Interactions in Pr:Eu

F. Götz, G. Czjzek, J. Fink, H. Schmidt, and P. Fulde[a]

[a]*Max-Planck-Institut für Festkörperforschung, D-7000 Stuttgart*

The rare earth metal Pr is a Van Vleck paramagnet with a singlet crystal field ground state for both lattice positions of its dhcp structure. The ratio of indirect exchange interactions and crystal field splitting is close to critical (0.95 /1/). As small changes of the exchange interactions may push the Pr ion over the polarization instability, magnetic impurities are expected to induce a long range magnetic polarization leading to magnetic ordering at low concentration.

We have studied dilute Pr:Eu alloys (0.6 at% $\lesssim c_{Eu} \lesssim$ 6 at%) be measurements of bulk magnetization and by ^{151}Eu Mößbauer spectroscopy. The results of bulk magnetization measurements were similar to those found for Pr:Nd /1/ where Lebech et al. observed a modulated antiferromagnetic structure. As in the case of Pr:Nd, no indication of magnetic order is found from bulk magnetization. The difference between the magnetization of the alloy and that of pure praseodymium is shown in the figure. At low temperatures it is positive in fields $\leq$ 10 kOe; the negative value at higher fields leads to the conclusion that the Eu-moment couples antiferromagnetically to the Pr-moments induced by the external field.
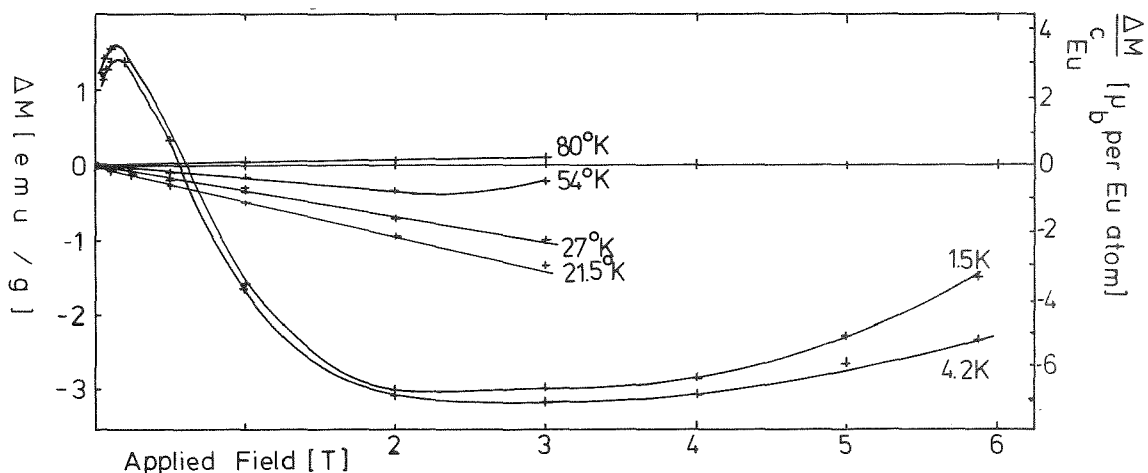
Fig.   Difference of magnetization of Pr$_{.988}$Eu$_{.012}$ and Pr-metal, $\Delta M = M_{PrEu} - 0.988 M_{Pr}$. The right-hand scale gives the resulting moment per Eu atom.

For low Eu concentrations ($c_{Eu} \lesssim 1.5$ %) magnetic hyperfine splitting of the Mößbauer spectra is observed below about 10 K. In the temperature range between 4 and 10 K the spectra are best described by a superposition of a broad single line and a split component, similar to spectra observed in the case of slow electronic relaxation /2/. At 1.5 K the spectrum is fully split corresponding to a unique hyperfine field.

At higher Eu concentrations ($c_{Eu} \gtrsim 4$ at%) the Mößbauer spectra consist of two subspectra with different isomeric shifts. The intensities of the two components are nearly equal. One of the subspectra is identical with the spectrum found at lower concentrations ($c_{Eu} \lesssim 1.5$ %); the other component is magnetically split at least up to room temperature for $c_{Eu} \sim 6$ %. As the ordering temperatures are quite different for different concentrations, this second spectrum probably is not caused by an unwanted phase admixture like Eu metal or an intermetallic Pr-Eu compound.

References

/1/ B. Lebech, K.A. McEwen, and P.A. Lingard, J. Phys. C8, 1684 (1975)

/2/ W. Wiedemann and W. Zinn, Phys. Lett. A24, 506 (1967)

3.6   A Mössbauer Study of Magnetic Interactions in GdBe$_{13}$

G. Czjzek, J. Fink, F. Götz, H. Schmidt, M.J. Besnus[a], and A. Meyer[a]

[a]Laboratoire Pierre Weiss, Université de Strasbourg, F-67 Strasbourg, France

The rare earth beryllides RBe$_{13}$ crystallize with a cubic structure (NaZn$_{13}$-type) in which the rare earth sites form a simple cubic lattice with a cube edge near 5 Å. For this large distance between rare earth neighbours, direct exchange interactions are expected to be negligible, and the magnetic properties should be determined primarily by the indirect interaction viy conduction electrons. These compounds may be regarded as simple model systems similar to diluted alloys, but with periodic spacing of the magnetic "impurities". Measurements of their magnetic properties /1,2,3/ yielded a variety of different magnetization curves and other interesting phenomena which in some cases can be attributed to effects of crystal fields and local anisotropy of the rare earth ions. The simplest behaviour is expected for the isotropic S-state ion Gd^{3+} in GdBe$_{13}$, a compound with antiferromagnetic order below about 25 K. In this paper we present results obtained by ^{155}Gd Mössbauer spectroscopy and magnetization measurements with polycrystalline GdBe$_{13}$.

From the Mössbauer spectra we can derive information both on the values
of the magnetic moments from the hyperfine fields and on their direction from
the intensities of absorption lines corresponding to $\Delta M = 0$ relative to those
for $\Delta M = \pm 1$ (in the spectrum all lines with $\Delta M = 0$ are grouped in the center.
Their intensity is proportional to $<\sin^2\theta>$ where θ is the angle between the
magnetic field acting on the nucleus and the direction of observation. The
intensities of the other lines are proportional to $1 + <\cos^2\theta>)$. From the
spectra taken in a magnetic field applied parallel to the direction of
observation at 4.2 K (Fig. 1). we deduce that the Gd moments rotate gradually
from random orientation ($<\sin^2\theta> = 2/3$ for $B_{appl} \leq 0.1$ T) into a direction
nearly perpencidular to $\vec{B}_{appl}$ ($<\sin^2\theta> \sim 1$ for $B_{appl} \sim 1$ T). Larger fields
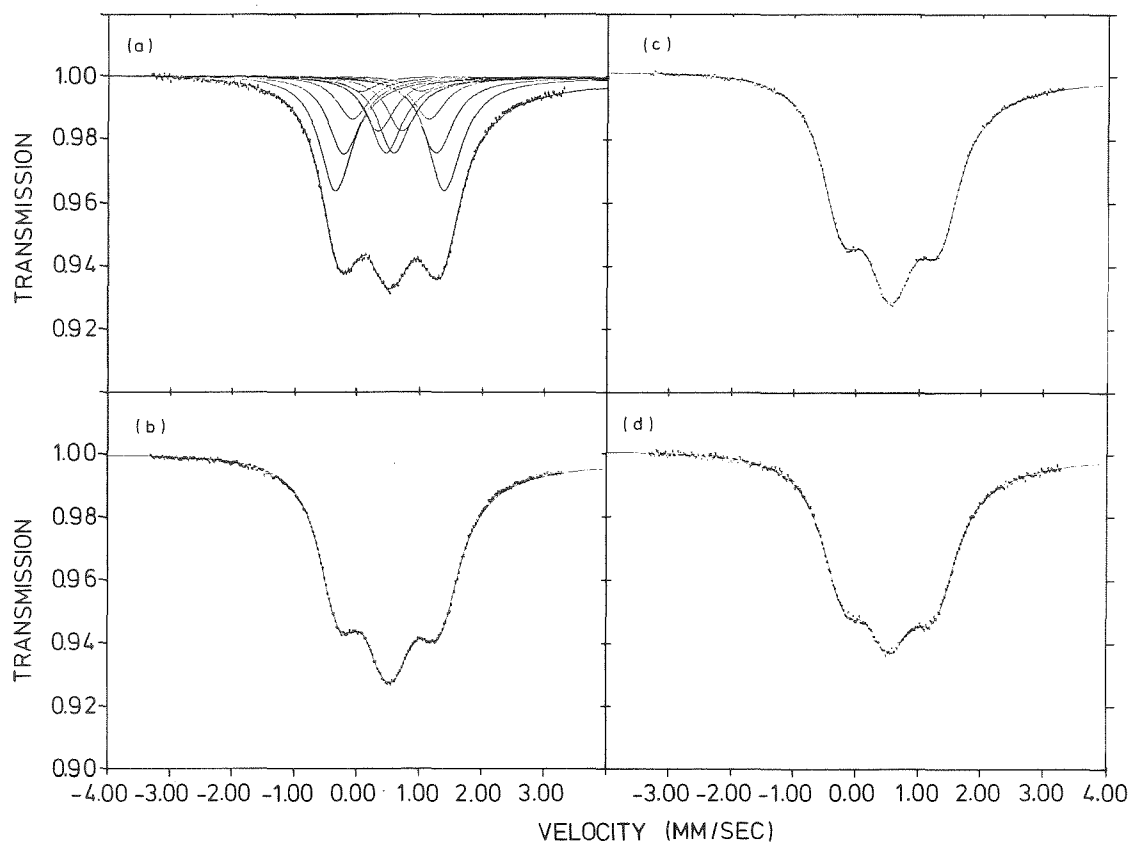
Fig. 1   Examples for Mössbauer spectra of ^{155}Gd in GdBe$_{13}$ at 4.2 K. Applied
field: (a) 0, (b) 1 T, (c) 3 T, (d) 5 T.
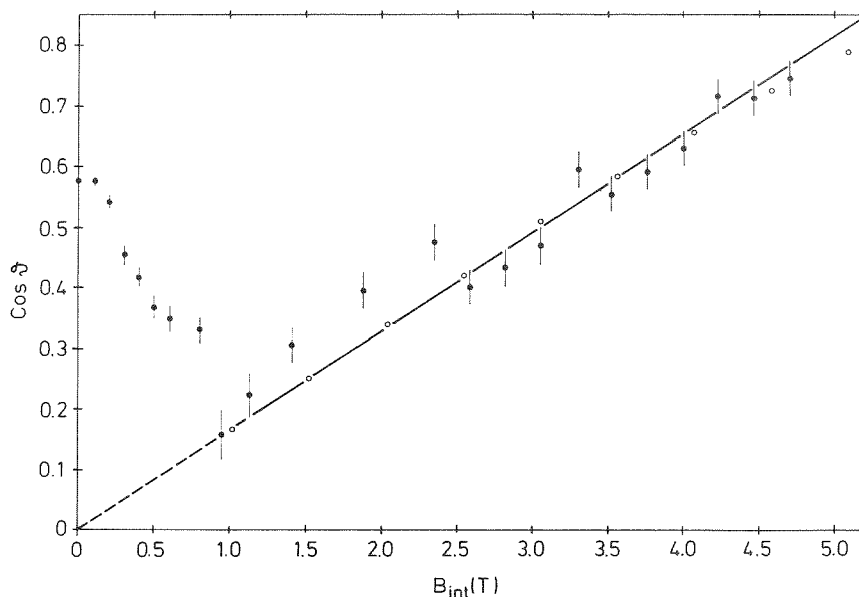
Fig. 2   Experimental results for cosθ as a function of the internal field
(= applied field plus Lorentz field minus demagnetizing field).
θ is the angle between the direction of the magnetic moments and
that of the applied field, ● derived from Mössbauer spectra, o
from magnetization measurements. For B < 1 T (i.e. in the region
of transition from random orientation to a direction perpendicular
to the applied field - the "spin-flop") the values shown are those
for $(< \cos^2\theta >)^{1/2}$.
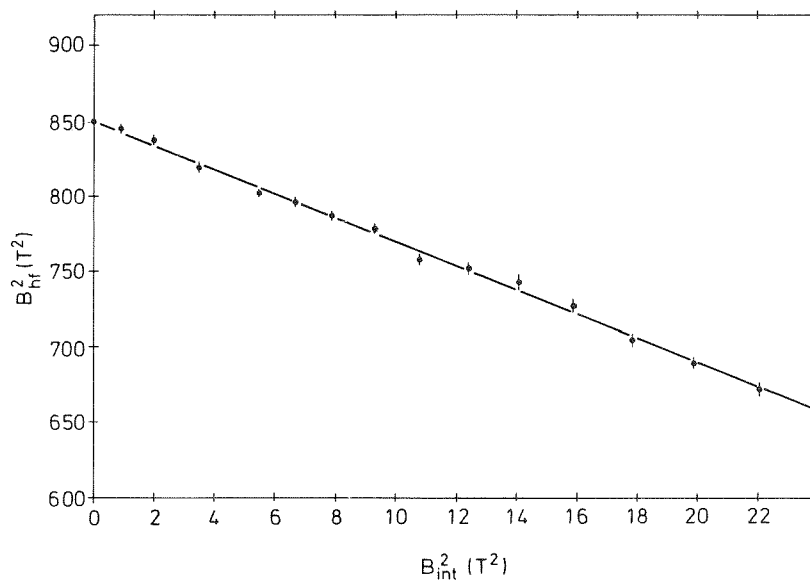
Fig. 3   Square of the field acting on the nuclei (vector sum of local,
transferred, dipole, and applied field) as a function of the square
of the applied field (corrected for demagnetization and Lorentz field)

force the moments ro rotate towards the direction of the magnetic field (Fig. 2).
These results are in good agreement with those of magnetization measurements and
are easily interpreted in terms of molecular field theory. From the observed
slope of $\cos\theta$ vs. B_{appl} and from the Néel temperature $T_N = (27 \pm 1)$ K a para-
magnetic Curie-Weiss temperature for the high-temperature susceptibility
($\chi = C/(T - \theta_P)$) of $\theta_P^{MF} = 15$ K is calculated in resonable agreement with the
experimental value $\theta_P^{exp} = 25$ K /1/. In a simple molecular field model including
exchange interactions between first and second neighbours these results are
compatible only with a magnetic order of the first kind (ferromagnetic (001)
planes with alternating sign). This magnetic structure has tetragonal symmetry,
thus dipole-dipole interactions must be taken into account. We find that these
interactions favour a direction of the moments within the ferromagnetic (001)-
planes. The difference between the dipole field for this direction and that
for an orientation along [001] is about 0.8 T, in good agreement with the field
required for complete spin-flop. From the variation of the hyperfine field with
applied field (Fig. 3) we can separately deduce the contributions due to atoms
on the two sublattices. We find: $B_{\uparrow\uparrow} = -(29.49 \pm 0.03)$T, $B_{\uparrow\downarrow} = -(0.10 \pm 0.03)$T.

References

/1/ E. Bucher, J.P. Maita, G.W. Hull, R.C. Fulton, and A.S. Cooper, Phys. Rev.
B11, 440 (1975)

/2/ A. Herr, M.J. Besnus, and A.J.P. Meyer, Colloques Internat. CNRS No. 242,
Grenoble, 47 (1974)

/3/ P. Meriel, A. Herr, and A. Meyer, Phys. Stat. Sol. (a) 46, K35 (1978)

3.7   Crystal Fields in $(Y,Er)Al_2$ and $(La,Er)Al_2$

P.v.Blanckenhagen, H. Happel[a], and K. Knorr[b]

[a]Hochschule der Bundeswehr München

[b]Institut für Physik der Universität Mainz

The point charge model predicts the crystal electric field (CEF) to be
the same for all $REAl_2$, $(Y,RE)Al_2$, and $(La,RE)Al_2$ compounds - apart from effects
of slight changes of the lattice constants -, since the diluents Y and La have the
same valences as the RE-ions. However, from measurements of physical properties
of these compounds which are influenced by the CEF, like magnetization, suscepti-
bility, EPR, specific heat, CEF-parameters were deduced which differed not only

in magnitude but even in sign (see, e.g., ref. /1/). In order to elucidate
the situation we recently started a systematic investigation of the $REAl_2$-
compounds by neutron spectroscopy in the paramagnetic region and could uniquely
determine the CEF-parameters of $ErAl_2$ and $TmAl_2$ /1, 2/. In this report inelastic
neutron scattering measurements on $Y_{0.92}Er_{0.08}Al_2$ are presented which will be
compared to the previous results on $ErAl_2$ and $La_{0.9}Er_{0.1}Al_2$ /1/.

The neutron scattering experiments were carried out on the MAG1 time-
of-flight spectrometer at the FR2 in Karlsruhe. The observed excitation
energies of $Y_{0.92}Er_{0.08}Al_2$ and their temperature dependence are very similar
to those of $ErAl_2$ /1/ with the only difference that in the latter compounds the
low temperature peak was located at 7.0 meV rather than at 6.3 meV. Thus one
expects two closely related level schemes with slightly shifted energies.
Analyzing the corresponding tables of ref. /3/ and the matrix elements given
in ref. /4/ we find as unique solution for $Y_{0.92}Er_{0.08}Al_2$ the CEF-parameters
x = +0.36 ± 0.02 and W = -0.046 ± 0.002 meV. With these parameters and the
characteristics of the spectrometer theoretical TOF-spectra were calculated
in good agreement with the experimental data.

In the table we have summarized the CEF-parameters x, W and A_4, A_6 of $ErAl_2$
and $Y_{1-c}Er_cAl_2$ deduced from our neutron data. The sixth order term of the
potential A_6 is altered by about 20 % when Er is substituted by Y, whereas /A_4/
is enhanced by a factor of 3. This may be understood qualitatively by arguments
discussed by Devine /5/.

With this background we have reconsidered neutron TOF-spectra of $La_{0.9}Er_{0.1}Al_2$
/1/ where only one transition has been observed hitherto. For this system we
propose the CEF-parameters given in the table which are able to describe the
neutron result, though this solution is not unique and additional neutron
scattering experiments should be performed.

Table   Crystal-field parameters deduced from inelastic neutron scattering data.
Values for $La_{0.9}Er_{0.1}Al_2$ are estimated as described in the text.

	x	W/meV	A_4/meV	A_6/meV
$ErAl_2$	0.16	-0.030	-1.6	-0.22
$Y_{0.92}Er_{0.08}Al_2$	0.36	-0.046	-5.5	-0.26
$La_{0.9}Er_{0.1}Al_2$	(0.50)	(-0.057)	(-9.4)	(-0.25)

References

/1/ K. Knorr, P.v.Blanckenhagen, and H. Happel, Solid State Commun. (in press)

/2/ H. Happel, P.v.Blanckenhagen, K. Knorr, and A. Murani, in: Crystal Field
    Effects in Metals and Alloys, ed. by A. Furrer, Plenum Press, New York
    and London, 273 (1977)

/3/ K.R. Lea, M.J.M. Leask, and W.P. Wolf, J. Phys. Chem. Solids $\underline{23}$, 1381 (1962)

/4/ R.J. Birgeneau, J. Phys. Chem. Solids $\underline{33}$, 59 (1972)

/5/ R.A.B. Devine, J. Phys. C$\underline{7}$, L71 (1974)

3.8   Analysis of Corrosion Layers on INCOLOY Alloy 800 by Conversion Electron
       Mössbauer Spectroscopy

J. Fink, H. Schmidt, G. Czjzek, and I. Michael[a]

[a]*IRB, Kernforschungszentrum Karlsruhe GmbH*

Conversion electron Mössbauer spectroscopy provides a method complementary
to others such as Auger electron spectroscopy, photoelectron spectroscopy, etc.
for in-situ investigations of thin corrosion layers on metals and alloys, as the
conversion electrons emitted after resonance absorption of γ-rays by specific
nuclei emerge only from a small depth range below the surface. In the case of
^{57}Fe the maximum depth is about 500 nm, and corrosion layers with a thickness
of more than about 10 nm can be analyzed.

    We have applied this method to two samples of INCOLOY alloy 800 ($\sim$ 50 % Fe,
$\sim$ 30 % Ni, $\sim$ 20 % Cr) which had been corroded at 342°C in pressurized water
(150 bar) with 5 ppm O_2 (sample 1) and 0.5 ppm O_2 (sample 2) respectively.
Fig. 1a) shows the spectrum obtained with sample 1, dominated by the strong
line due to the nonmagnetic alloy. This line, which is broadened by distributions
of isomer shifts and quadrupole interactions in the random alloy, makes the analysis
difficult. It can be removed by subtracting the spectrum of an uncorroded steel
sample. The resulting spectra are shown in Fig. 1b) and c). This procedure leaves
a small uncertainty for the intensities in a velocity range of about $\pm$ 1 mm/sec
around the center of the line due to the steel substrate.
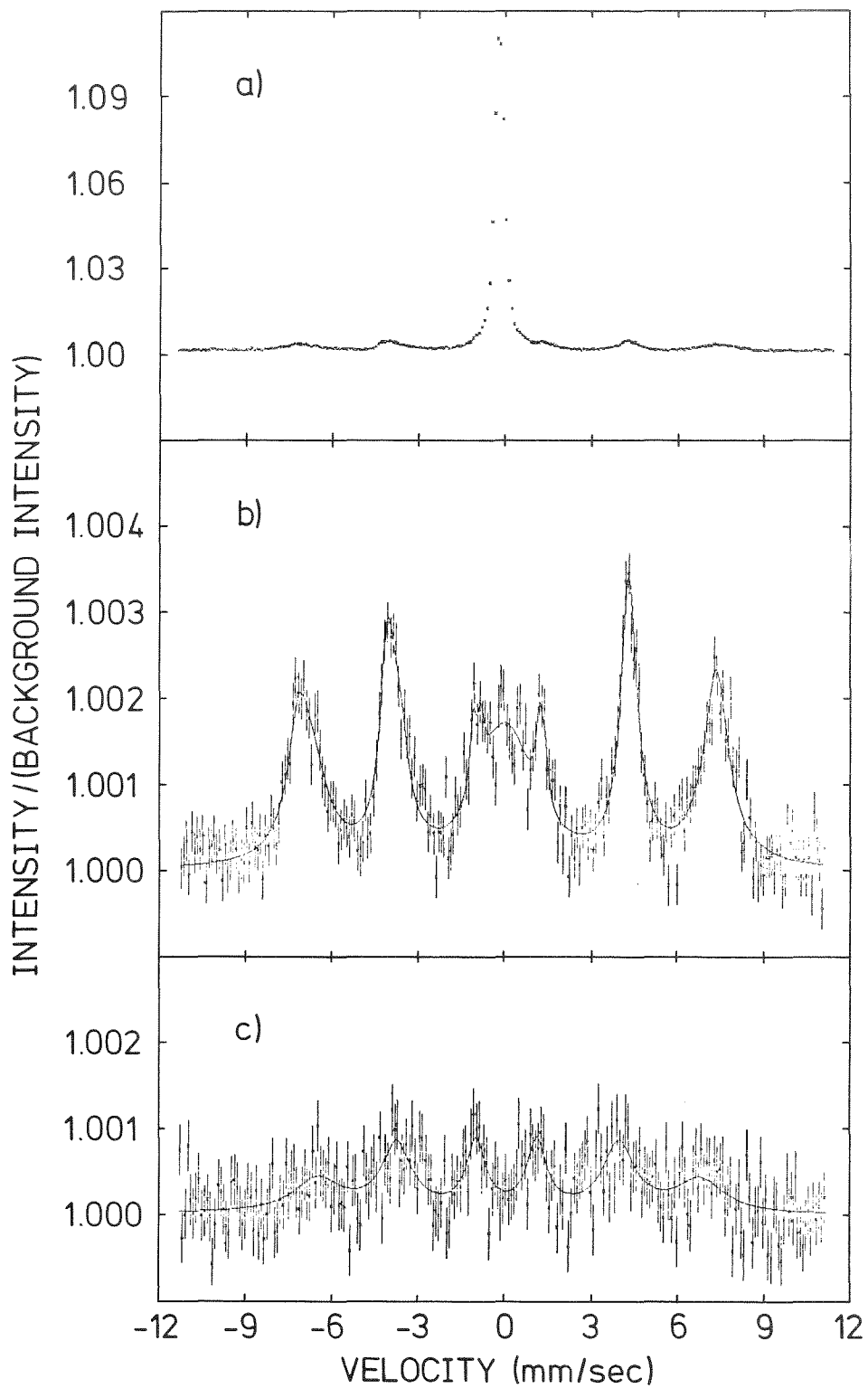
Fig. 1

a) Conversion electron Mössbauer spectrum of sample 1, INCOLOY 800, corroded at 342°C in pressurized water with 5 ppm O_2.

b) The same spectrum after subtraction of the spectrum obtained from an uncorroded INCOLOY 800 sample.

c) Spectrum of sample 2 (0.5 ppm O_2) after subtraction of the INCOLOY 800 line.

It is quite obvious that the spectra of the two samples have quite a different character. For sample 1 the total intensity is about 3 times that of sample 2. Furthermore, the spectrum of sample 2 can be fitted with a single 6-line component of rather broad lines whereas for sample 2 a satisfactory fit is obtained only if we assume a superposition of 3 different components. Thus, regarding the corrosion products of Fe, the layer on sample 2 certainly is more homogeneous than that on sample 1. The hyperfine parameters deduced from least squares fits to the 2 spectra are given in the table.

Table

Hyperfine parameters deduced from conversion electron Mössbauer spectra of corrosion layers on 2 samples of INCOLOY 800. δ: isomer shift with respect to pure Fe; Γ_0: line width (for components with magnetic hyperfine splitting: width of the inner pair of lines; for components 1 and 2 of sample 1, Γ_0 was not varied in the fitting procedure); $\Delta_Q = \frac{1}{2} e^2 qQ$, quadrupole splitting; $<|B_{hf}|>$: average hyperfine field; δB: full width at half maximum of the distribution of hyperfine fields. From this width the approximate range of concentrations shown in the last column was deduced. Standard deviations are given in parentheses.

sample	component	fraction of total intensity (%)	δ (mm/sec)	Γ_0 (mm/sec)	Δ_Q (mm/sec)	$<\|B_{hf}\|>$ (T)	δB_{hf} (T)	most probable compound
1 (5ppm O_2)	1	30(1)	0.22(0.03)	0.1	0(+0.05)	46.0(0.2)	4.1(0.5)	site A ⎱ in $(Ni_{1-x}Fe_x)(Cr_{1-y}Fe_y)_2O_4$ with $0.5 \le \frac{y}{x} \le 0.6$; $0.3 \le x \le 0.7$ — $Ni(Cr_{1-x}Fe_x)_2O_4$ with $0.35 \le x \le 0.7$ or $(Cr_{1-y}Fe_y)_2O_3$ with $0.45 \le y \le 0.7$
	2	33(3)	0.46(0.04)	0.1	0(+0.1)	44.5(0.3)	7.2(0.7)	site B ⎰
	3	37(8)	0.20(0.06)	1.9(0.4)	0.6(0.2)	0	-	Fe OOH, possibly amorphous
2 (0.5ppm O_2)	1	100	0.26(0.05)	0.7(0.2)	0(+ 0.2)	42.1(0.7)	10(2)	$(Cr_{1-x}Fe_x)_2O_3$ with $0.3 \le x \le 0.8$

These results allow a tentative identification of the compounds forming the layers. The pure iron oxydes Fe_2O_3 and Fe_3O_4 can be excluded as the magnetic hyperfine fields given in the table are much too small. Similarly, the isomer shift of FeO, which is nonmagnetic at room temperature, is about 1 mm/sec, and consequently FeO cannot be the compound giving rise to component 3 in the spectrum of sample 1. A literature search of ^{57}Fe hyperfine interaction parameters for mixed oxides of Fe, Cr, and Ni /1,2,3,4/ lead to the tentative identification shown in the last column of the table.

References

/1/ W. Meisel, Werkstoffe und Korrosion 21, 249 (1970)

/2/ M. Robbins, G.K. Wertheim. R.C. Sherwood, and D.N.E. Buchanan, J. Phys. Chem. Solids 32, 717 (1971)

/3/ P.P. Kirichok. G.S. Podvalnykh, and V.F. Belnov, Bull. Acad. Sci. USSR, Phys. Ser. 36, 364 (1972)

/4/ T. Birchall and A.F. Reid, J. Solid State Chem. 13, 351 (1975)

4. MATERIALS RESEARCH

4.1 Metastable, Crystalline Lead-Bismuth Alloys Produced by Ion Implantation

C. Gauss

For the study of superconductivity the system lead-bismuth with its large electron-phonon coupling is of considerable interest. The electron-phonon parameter λ is a monotonic function of the bismuth concentration; from 1.51 (Pb) to 2.13 (Pb$_{.65}$Bi$_{.35}$) /1/. The systematic study /1/ was ended at a bismuth-concentration of 35 at% because at room temperature the solubility of bismuth in lead ceases there /2/.

By ion implantation the solubility of an element in an alloy can be increased beyond the thermodynamical limit. In the present study lead-bismuth alloys were prepared with bismuth-concentrations greater than the thermal solubility by ion implantation. To qualify the prepared layers the crystal structure was examined by X-rays, the thickness by Rutherford backscattering and the superconductivity by the transition temperature.

Previous studies /3/ had shown, that the implantation of lead-bismuth alloys with bismuth-ions are not successful on account of sputtering. Therefore a different method was chosen. Oversaturated lead-bismuth alloys were irradiated with argon-ions with an energy of 640 keV such that the ions penetrated the 160 nm thick layers and were stopped in the quartz-substrate. The subsequent determination of the transition temperature T_c was done by 4-probe measurement of the electrical resistance as a function of temperature. The definition of the transition temperature is the point of intersection of two straight lines - the tangent at the point of inflection of the resistance curve and the straight line of the residual resistance extrapolated to lower temperatures.

In the experiments only a part of the layer was irradiated with argon-ions. Fig. 1 shows a typical T_c-measurement. The curve 1 - 2 shows the resistance of the non-irradiated region, the curve 2 - 3 that of the irradiated region as a function of temperature. The curve 1 - 3 corresponds to two superconductors with different transition temperatures connected in series. For the determination of the absolute temperature, the transition temperature of a niobium-reference layer (T_c = 9.20 K) was also measured.
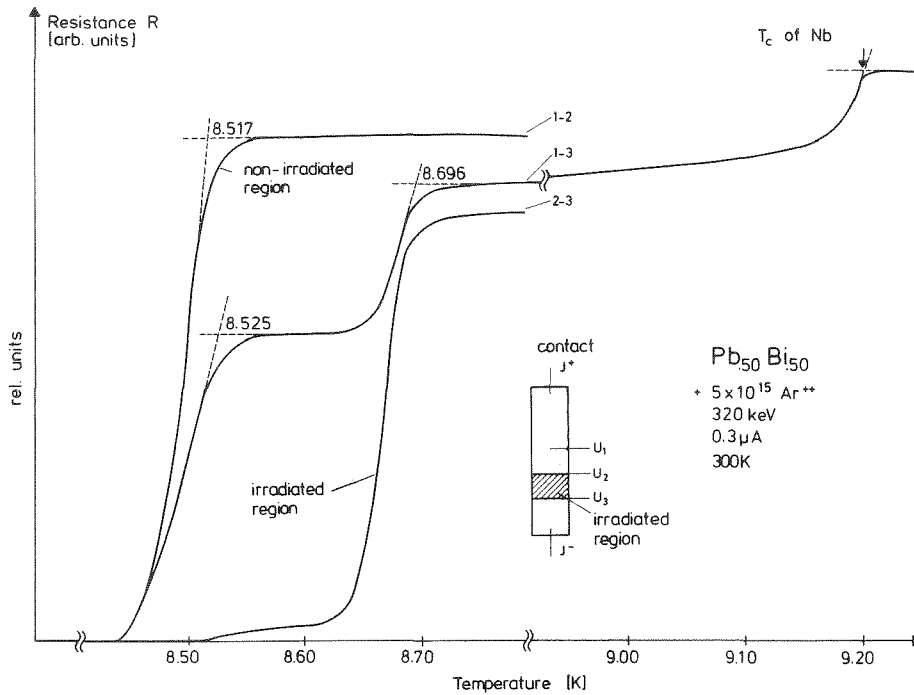
Fig. 1   An example of a T_c-measurement of an irradiated $Pb_{.50}Bi_{.50}$-layer

There exists no information on the nature of the bismuth precipitates in the oversaturated lead-bismuth alloys. So first the change of the transition temperature as a function of the argon-fluence was measured. Fig. 2 shows the results.
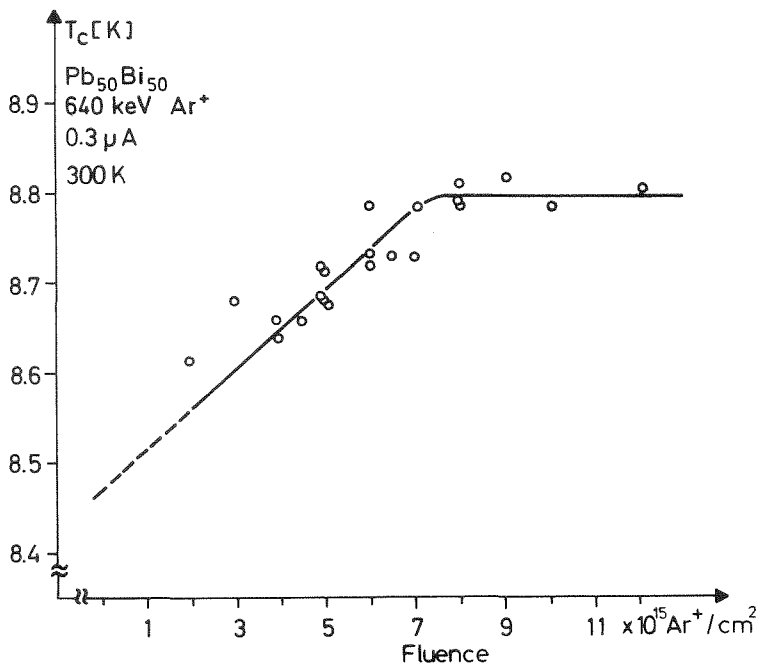
Fig. 2

T_c as a function of the argon-fluence $\emptyset$

The linear increase of the transition temperature from 8.45 K to 8.82 K with increasing fluence of $9 \cdot 10^{14}$ Ar$^+$/cm^2 to $8 \cdot 10^{15}$ Ar$^+$/cm^2 is explained by the steady dissolution of the bismuth precipitates. The saturation of the T_c-increase (8.82 K) for greater fluences ($> 8 \cdot 10^{15}$ Ar$^+$/cm^2) is interpreted as a balance between the dissolution of the precipitates and a diffusion of dissolved bismuth into the precipitates.

$Pb_{1-x}Bi_x$-alloys with different bismuth-concentrations x were also irradiated with a fluence of $8 \cdot 10^{15}$ Ar$^+$/cm^2. The transition temperature increase rapidly at the limit of solubility and reaches a maximum $\Delta T_c = 360$ mK (Fig. 3). This result shows that by recoil implantation additionally dissolved bismuth causes the change in T_c.
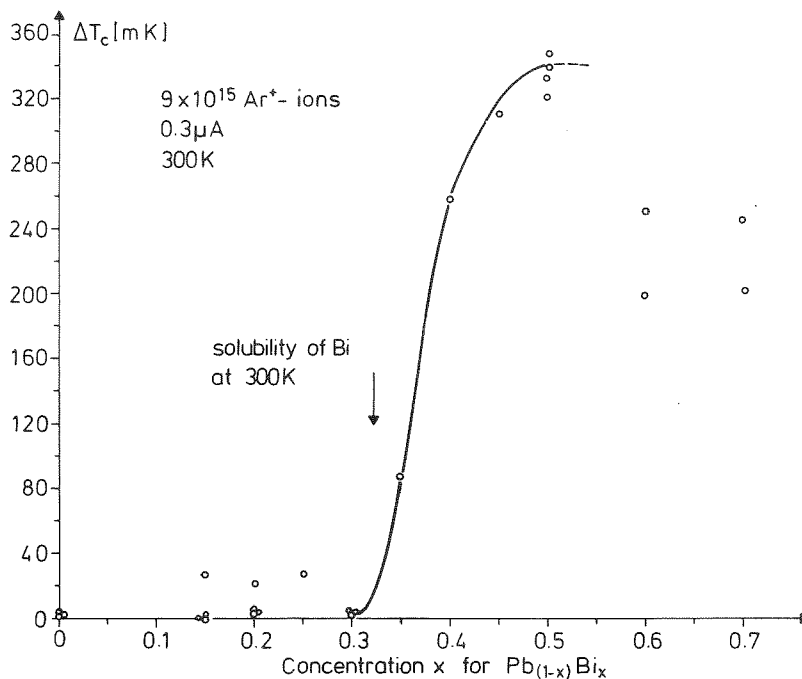
Fig. 3   The change of the transition temperature irradiated with the saturation fluence as a function of the Bi-concentration.

Normally the process of ion implantation is only a weak function of temperature when radiation effects are neglected. It is known, that in lead radiation effects at room temperature are small /4/. The substrate-temperature however is a sensitive parameter in the experiments. With increasing substrate temperature the superconducting transition temperature increases exponentially (Fig. 4). This result is at least partly due to the temperature dependence of the solubility. Other contributions to the increase of the bismuth-solubility are presently tested.
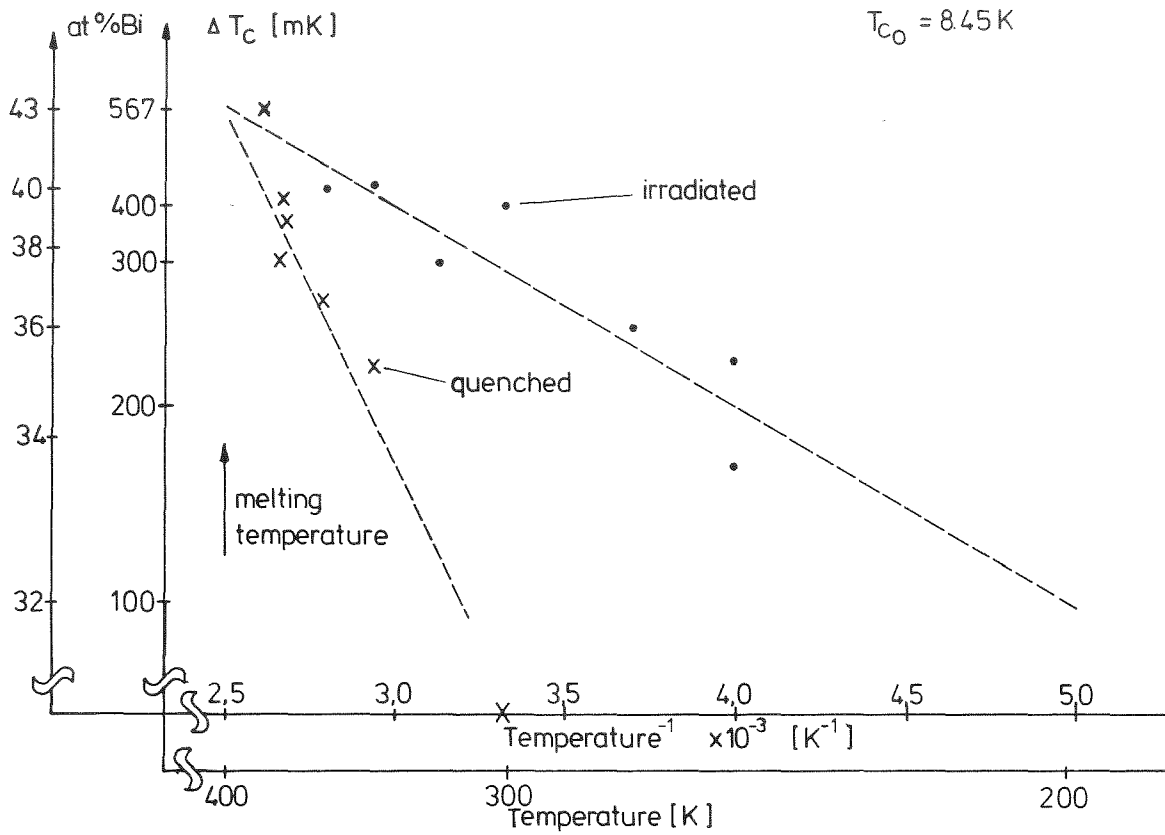
Fig. 4   Influence of the substrate-temperature during the irradiation
         on the increase of the transition temperature

References

/1/ R.C. Dynes and J.M. Rowell, Phys. Rev. B11, 1884 (1975)

/2/ B. Predel and W. Schwermann, Z. Metallkunde 58, 553 (1976)

/3/ C. Gauss, in Prog. Rep. Teilinst. Nukl. Festkörperphysik, Ges. f. Kern-
    forschung, KFK 2538, 90 (1977)

/4/ H. Schroeder and W. Schilling, Rad. effects 30, 243 (1976)

4.2   Channeling Analysis of Radiation Disorder in Ion Implanted Vanadium and
       Molybdenum Single Crystals

G. Linker

Abstract

Energy dependent channeling and backscattering analysis with $^4He^+$ ions in the energy range 1.0 - 2.8 MeV has been performed on V and Mo single crystals implanted either with Ne^+ or N^+ (C^+) ions ($\sim 5 \cdot 10^{16}$ ions/cm^2). The spectra of the implanted samples revealed an appreciable amount of dechanneling but only a small energy dependence of the dechanneling yield was observed. However, characteristic differences of the dechanneling profiles were detected in the Ne^+ and N^+ implanted crystals. The Ne^+ bombarded samples showed an almost linear increase of the dechanneling yield with depth but showed no change of the shape of the spectra as a function of analyzing beam energy. In contrast, the N^+ implantations revealed a peak in the spectra at the range of the implanted impurities as the beam energy was increased. These observations indicate that different types of defects are generated with implantations of Ne^+ and N^+ ions. The results are discussed together with changes of the superconducting transition temperature in ion implanted and irradiated V and Mo layers.

4.3   Influence of Ion Bombardment on the Superconducting Transition Tempera-
       ture of Evaporated Vanadium Layers

G. Linker

Abstract

The influence of ion irradiation and implantation on the superconducting transition temperature T_c of evaporated vanadium layers has been investigated as a function of ion species and layer purity. Irradiations of pure layers with Ne^+ ions and fluences of typically 10^{16} ions/cm^2 lead to small T_c decreases ($\Delta T_c \sim 0.1 - 0.2$ K). In oxygen contaminated layers however appreciable changes of T_c ($\Delta T_c \sim 2 - 3$K) are observed depending on oxygen content and ion fluence.

Similarly, the direct implantation of chemically active impurities (N^+, O^+) leads to drastic changes of T_c. Here T_c decreases as a function of nitrogen concentration down to the detection limit of 1.2 K. From these results it is concluded that the T_c changes are due to impurity stabilized disorder. Energy dependent channeling analysis of nitrogen and neon implanted V and Mo single crystals has been performed to obtain additional information on the nature of this disorder.

4.4   Preparation and Analysis of Evaporated Niobium Superconducting Thin Films

G. Linker and R. Smithey

Niobium thin films with thicknesses in the range of 120 - 250 nm have been prepared by electron beam evaporation onto quartz and carbon substrates kept at room temperature or heated to 500 - 800°C. The pressure in the evaporation chamber before deposition typically was $2 \cdot 10^{-9}$ Torr and rose to about $5 \cdot 10^{-8}$ Torr at evaporation rates of 3 nm/s. Layers were deposited both under optimum conditions and at deliberately caused partial pressures of oxygen and nitrogen in the range from $5 \cdot 10^{-8}$ to $1 \cdot 10^{-5}$ Torr.

Film thickness, purity, homogeneity, and impurity content and its distribution have been analyzed by Rutherford backscattering of 2 MeV He ions. The analysis of layers, when deposited onto carbon substrates, allowed a concentration determination of oxygen and nitrogen down to about 0.5 at%. The structure of the layers has been analyzed using a thin films X-ray camera. The superconducting transition temperature T_c was measured resistively and the residual resistivity ratio r, defined as the resistance ratio at room temperature and before transition into the superconducting state, was determined as a measure of layer quality.

Layers prepared under optimum conditions at room temperature had T_c-values around 9.4 K, r-values of about 4 and oxygen contents between 1 - 2 at%. For layers prepared at elevated substrate temperatures (500 - 600°C) these values were 9.3 K, 6.2 and < 1 at%, respectively. The high T_c-values in layers with relatively high oxygen contents indicate that the oxygen was not interstitially incorporated into the Nb-structure but probably was present in the layers in form of oxide precipitates /1/. At substrate temperatures above
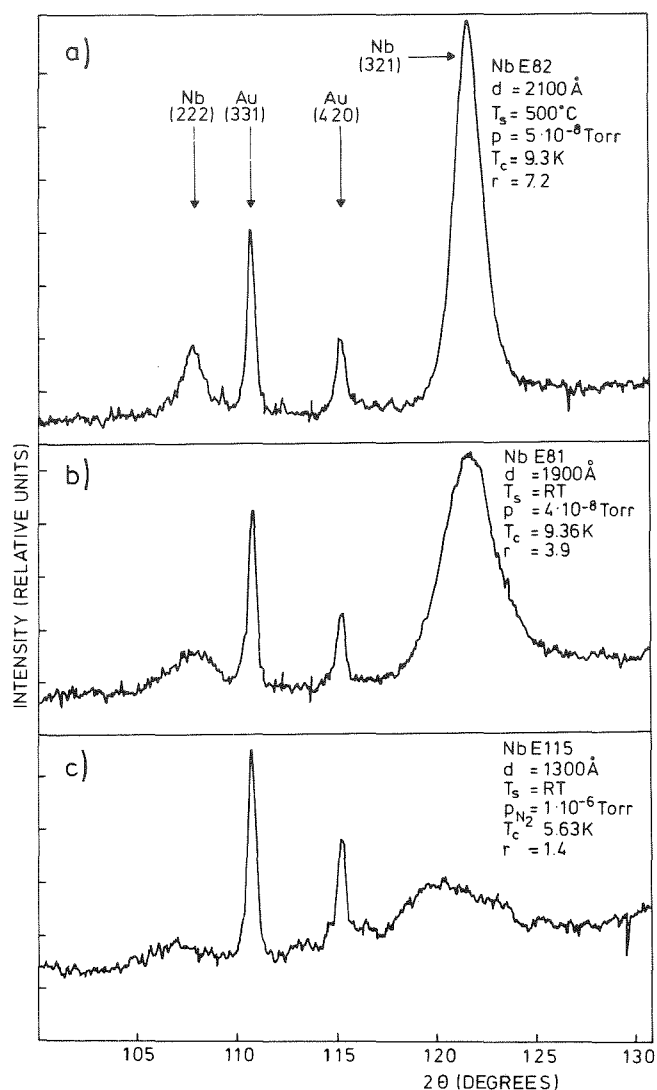
Fig. 1

Microdensity profiles of the (222) and (321) lines from photographs of Nb films prepared under different conditions, together with Au calibration lines.
Layer thickness d, substrate temperature T_c, pressure during evaporation p, transition temperature T_c and residual resistivity ratio r are listed in the figure.

$700^\circ C$, both T_c and r decreased. Similarly evaporations in oxygen or nitrogen atmospheres led to enhanced impurity contents in the layers and to reductions of T_c down to the detection limit (1.2 K) and of r below 1.0 depending on the partial pressure in the evaporation chamber.

All the layers evaporated under optimum conditions revealed the pure bcc-structure with a lattice parameter slightly above that of bulk material. A considerable difference in the linewidth however was observed for layers prepared at room temperature and at elevated temperature. This effect is demonstrated in Fig. 1a), b) for the (321) line. A particle size of about 12 nm has been estimated for the room temperature layers and of about 25 nm for layers prepared at elevated temperature, if the line broadening is ascribed to particle size effects alone. Evaporation in the presence of reactive gases led to distortions of the Nb bcc-structure with a considerable line broadening, intensity decrease and a line shift to lower angles indicating

a lattice parameter increase. An example for this behaviour is given in Fig. 1c).
The degree of distortion was depending on impurity content and an amorphization
of the layers was observed at about 30 at% of impurities incorporated into the
layers.

The results of this analysis show that r-values for the layers closely
correlate with growth conditions (substrate temperature). Both r and T_c are
sensitive to impurities incorporated into the bcc-structure and are strongly
affected at high impurity levels in the layers, causing amorphization of the
structure.

Reference

/1/ W. DeSorbo, Phys. Rev. 132, 107 (1963)

4.5   Superconducting Transition Temperature and Structure of Ion Bombarded
       Niobium Thin Films

       G. Linker and M. Kraatz

An enhanced influence of impurities on the superconducting transition
temperature T_c of ion irradiated and ion implanted vanadium layers has been
described in an earlier study /1/. The control of T_c for niobium layers by
nitrogen ion implantation has been reported recently /2/. In this study the
influence of ion irradiation for the case that the bombarding particles
penetrate the layers and come to rest in the substrate, and of impurity
atoms (N, O, Ne) implanted into the layers on T_c and the structure of
evaporated Nb thin films has been investigated.

The as-evaporated layers (see preceding report) had T_c values in the
range 9.2 - 9.5 K and oxygen contents up to 2 at%. Layers with the least oxygen
content were implanted with N^+ ions in the concentration range from 1 - 30 at%.
Ne^+ and O^+ profiles corresponding to 5 at% impurity were implanted for
comparison. Irradiations of layers with different oxygen contents were
performed with 360 keV Ne^+ and fluences of $1 \cdot 10^{15} - 1 \cdot 10^{17}$ ions/cm^2.
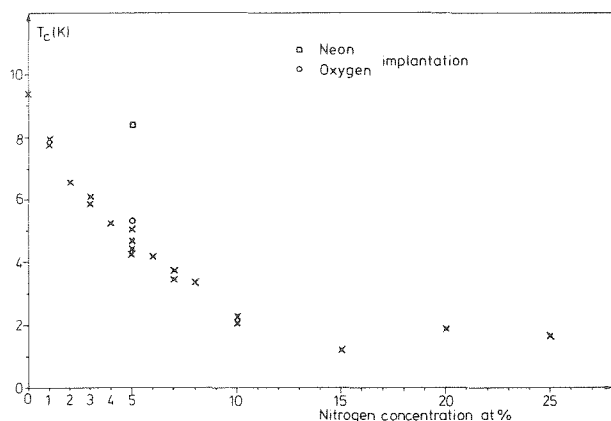
Fig. 1 T_c vs. nitrogen concentration in implanted niobium layers
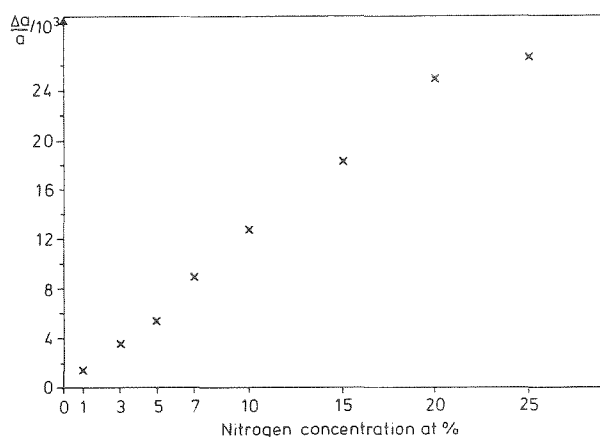
Fig. 2 Relative lattice parameter increase vs. nitrogen concentration in implanted niobium layers

T_c as a function of the implanted nitrogen concentration is shown in Fig. 1. Different T_c values at the same concentration indicate the reproducibility of the experiments performed with different layers. A continuous depression of T_c is observed with nitrogen concentration down to the T_c measuring limit of 1.2 K at 15 at% N. For higher N concentrations a slight T_c increase is observed. Though this effect must be still confirmed, it may be due to nitride precipitation in the layers. While the implantation of oxygen led to a similar T_c depression as observed for nitrogen, only a relatively small decrease occured for the neon implantation. The measurement points are included in Fig. 1.

In the irradiation experiments T_c depressions have also been observed. Here the effect was a function of ion fluence and depended on the oxygen content. For higher oxygen contents larger T_c depressions occured. In this experiment however the influence of secondary effects like the recoil implantation of impurities from surface oxide layers especially at high fluences must still be explored to quote quantitative results.

The T_c depressions were accompanied by a decrease of the residual resistivity ratio r. Layers with high (> 5) initial r-values revealed a rather sharp drop of r for small implantation or irradiation fluences to a value of about 3. A unique relationship between the T_c- and r-values of the ion-bombarded layers showed up, with a T_c-saturation for r-values above 3. This relationship suggests a common defect structure in the implanted and irradiated layers.

The depressions of T_c correlate with structural distortions in the bombarded Nb layers. In the N-implanted layers the bcc structure is preserved up to an impurity concentration of 15 at%. In this range some line weakening and a considerable increase of the lattice parameter a was observed. The relative increase of a as a function of nitrogen concentration is shown in Fig. 2 and reveals an almost linear relationship up to 20 at% N. In the nitrogen concentration range of 20 - 25 at% the high angle lines disappeared and only faint and broad low angle lines were observed indicating heavy structural distortions towards amorphization. At 30 at% new lines appear in the X-ray photographs probably due to nitride precipitation.

The linear relationship between impurity concentration and lattice parameter increase suggests that the T_c-reductions are due to a homogeneously distorted Nb structure with the degree of distortion growing with impurity concentration.

References

/1/ G. Linker, J. Nucl. Mat. _72_, 275 (1978)

/2/ K. Gamo, H. Goshi, M. Takai, M. Iwaki, K. Masuda, and S. Namba, J.J.Appl. Phys. _16_, 1853 (1977)

4.6   Channeling Studies in Carbon Implanted NbC-Single Crystals

J.M Lombaard[a] and O. Meyer

[a]_Physics Department, University of Pretoria, Pretoria 0002, South Africa_

Abstract

Critical angles and minimum yields have been measured for the Nb and the C-rows in [110]-aligned $NbC_{0.89}$ and have been compared to calculated values. Similar measurements have been performed in C-implanted NbC single crystals. Differences in the dechanneling yields of the Nb and C-sublattice have been found indicating an additional damage component in the C-sublattice.

4.7 The Superconducting Transition Temperature of Niobium Carbide
Single Crystals After Implantation of Light Elements

J. Geerk, M. Kraatz, O. Meyer, and B. Scheerer

The superconducting transition temperature T_c of niobium carbide is very
sensitive to deviations of the carbon content from stoichiometry. The maximum
carbon content obtainably by conventional methods is 0.98 corresponding to a
T_c of 11.1 K. By implantation of carbon ions the carbon content could be
increased resulting in a T_c of 11.8 K /1/. To investigate whether the deficient
carbon could be substituted by other light elements, single crystals of
$NbC_{0.89}$ with a T_c of 4.0 /2/ were implanted with elements from rows 2 and 3 of
the periodic system. During implantation the samples were held at elevated tempera-
tures. Implantation energies and fluences were selected to result in
homogeneously implanted surface layers of about 2000 Å thickness with a
concentration of 12 at% of implanted ions. The superconducting transition
temperature was measured resistively by the use of an alternating current
4 point probe method described elsewhere /3/.

Fig. 1 shows the transition temperature of single crystals implanted
with P^+ and S^+ ions as a function of implantation temperature. As T_c seems to
saturate at about 920°C, which is also the optimum implantation temperature
for carbon implantation /1/, all following implantations were carried out at
this temperature.
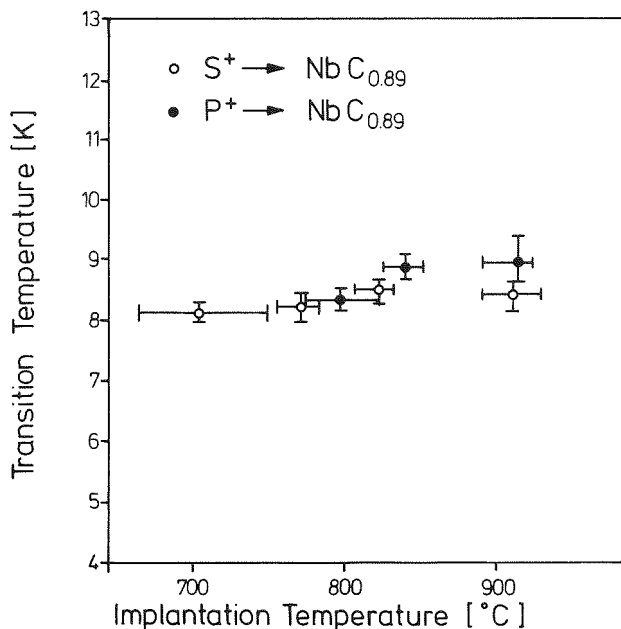
Fig. 1
The transition temperature of
$NbC_{0.89}$ single crystals as a
function of implantation tem-
perature. S^+ and P^+ ions were
implanted with fluences which
results in a concentration at
12 at%.

Fig. 2 shows the transition temperature after implantation with elements from row 2 and 3 of the periodic system including He from row 1, where the abscissa denotes the atomic number of the implanted element. T_c is continuously increasing from Li ($\simeq$ 5.5 K) to N (12.8 K). O and F do not continue this trend further. A striking fact is the T_c increase found after rare gas implantation with the highest value of T_c = 9.7 K for He. Annealing of a He-implanted single crystal at 1050°C for 300 sec resulted in a rapid decrease of T_c down to 5 K.
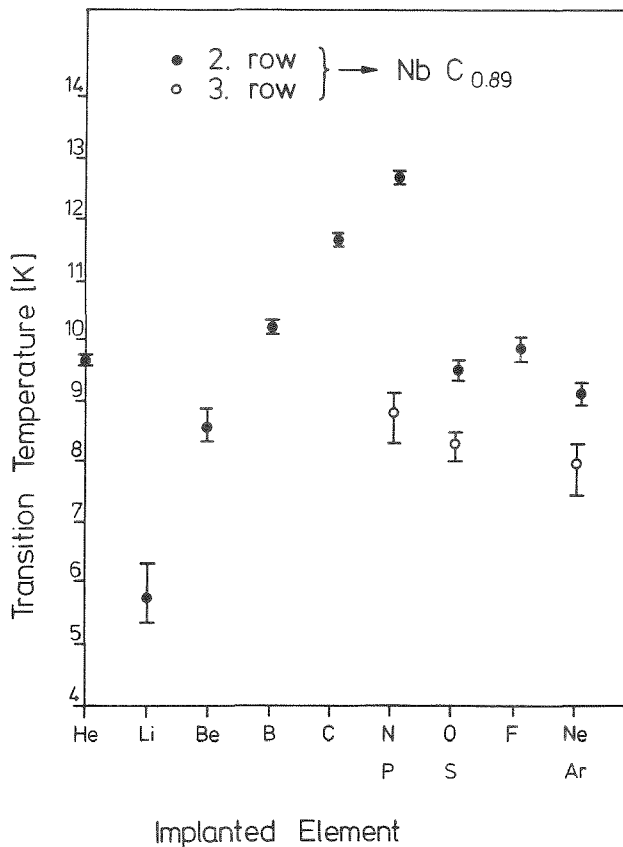
Fig. 2   The transition temperature of $NbC_{0.89}$ single crystals after implantation of elements from rows 2 and 3.

References

/1/ J. Geerk and K.-G. Langguth, Solid State Comm. 23, 83 (1977)

/2/ B. Scheerer and W. Reichardt, in Prog. Rep. Teilinst. Nukl. Festkörperphysik, Ges. f. Kernforschung, KFK 2054, 74 (1974)

/3/ K.-G. Langguth and J. Geerk, in Prog. Rep. Teilinst. Nukl. Festkörperphysik, Ges. f. Kernforschung, KFK 2357, 104 (1976)

4.8   On the Production of Tunneling Barriers on Niobium Carbide Single Crystals

J. Geerk and B. Scheerer

So far tunneling studies of NbC and TaC have been carried out on samples treated by chemical methods to achieve a clean surface prior to oxidation. The main experimental difficulty then arises through the fact, that results from chemically cleaned samples are unreproducible to an extent that studies of this kind touch the limit of effectiveness of experimental work. A more reliable cleaning method is ion etching which has been applied in a first test series to niobium carbide.

Single crystals of $NbC_{0.93}$ with a superconducting transition temperature T_c of about 8 K have been prepared by zone refining a pressed powder mixture of 1 part Nb in 1.04 parts c /1/. The single crystals have been etched electrolytically in HF /2/, resulting in a flat and shiny surface. After ion etching in an UHV-apparatus described in /3/ the samples were oxidized in air or pure oxygen at different temperatures between $200^{\circ}C$ and $285^{\circ}C$ for 2 hours. After masking of suitable tunneling surfaces (0.01 x 0.01 mm^2) counter electrodes were evaporated. Then the sample was mounted in a liquid He-cryostat for the tunneling measurements. In the following the main results of 15 runs are described.

We found a high degree of reproducibility from run to run obviously due to the fact that ion etching provides reliably clean surfaces. The junction resistivity turned out to be a strong function of oxidation temperature. Fig. 1 shows the junction resistance in the normal state as a function of oxidation temperature. The vertical bars are a measure for the deviations of many different junctions prepared at the same oxidation temperature. Junctions below 5 kΩ are suited for a detailed tunneling measurement /2/ concerning the limits of the electronics.

Fig. 2 shows the dI/dU characteristic of a typical junction in the superconducting state. The resistance of the junction was 200 Ω. In the voltage region near the energy gap the dI/dU characteristic reflects very well the density of states of the superconductor. However, measurements of the phonon induced structures situated between 20 and 30 meV were not possible due to the strong bending up of the curve in this voltage region. This strongly varying background is caused by a tunneling barrier very low in height. Here the height can be estimated to about 0.2 - 0.3 eV, whereas a minimum height of 0.7 eV is necessary for a determination of phonon induced structures /2/. As a low barrier

height is mostly due to an oxide barrier with a low oxygen content the work in
future will be concentrated on the development of an oxidation procedure, that
yields a high oxidation stage of niobium.
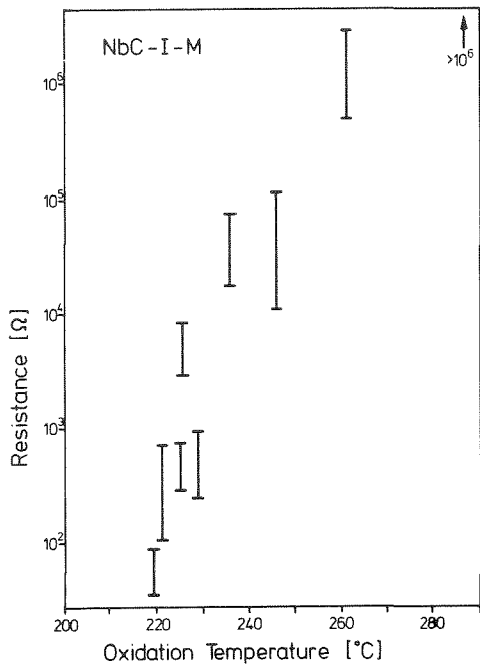
Fig. 1
The resistance of NbC-I-M
tunnel junctions as a function
of oxidation temperature.
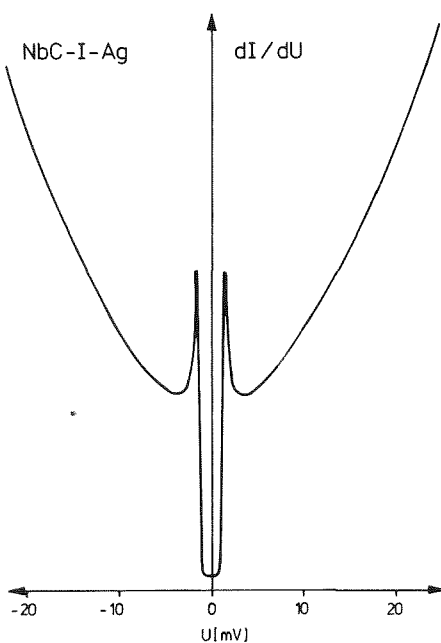
Fig. 2
The first derivative dI/dU of a
tunnel junction NbC-I-Ag as a
function of voltage.

References

/1/ B. Scheerer, private communication

/2/ J. Geerk, Ges. f. Kernforschung, KFK 2410 (1976)

/3/ J. Geerk , this report, p. 109

4.9   Channeling Effect Studies in V₃Si Single Crystals

O. Meyer

Abstract

Angular scans through the [100] and [110] channeling directions in V_3Si have been performed using elastically scattered He ions for the V-rows and the $^{28}Si(d,p)^{29}Si$ reaction for the Si-rows. The amplitude of thermal vibration perpendicular to the V-chains was found to be larger than that at 45° to them. The Si atoms however vibrate isotropically. The use of multi-row potentials instead of single-row potentials leads to better overall agreement between measured and calculated critical angles.

4.10   Radiation Damage and Superconductivity in V₃Si Single Crystals

O. Meyer

Abstract

Single crystals of V_3Si have been implanted at room temperature with Zr, Kr and He ions and were analysed using the backscattering and channeling techniques. A strong component of direct backscattering has been observed due to randomly displaced interstitials resulting in amorphization at Kr ion fluences of about $3 \cdot 10^{14}/cm^2$, similar to those observed for covalently bonded systems. For He ions, using the same energy-deposited density, this component is found to be a factor of about 30 lower than that observed for heavy ions. In the region of low damage level (near the surface) for crystals implanted with 300 keV He ions a narrowing of the critical angle of about 12 % is found for the [100] as well as for the [110] channeling direction. These results can be explained assuming the V-atoms have been displaced from their lattice sites with an average displacement of about 0.1 Å. The influence of the various damage structures on the superconducting transition temperature T_c is discussed.

4.11 Computer Simulation of Channeling Measurements on V_3Si Single Crystals

R. Kaufmann and O. Meyer

A computer program has been developed /1/ to simulate the channeling process of He-ions in V_3Si with A15 crystal structure. The program takes into account the interactions of an ion with all neighboured atoms in a plane and consideres the anisotropy of the thermal vibrations of the V-atoms. The following thermal vibration amplitudes as determined from X-ray measurements /2/ were used: for V: $\sqrt{u_{22}} = \sqrt{u_{33}} = 0.076$ Å and $\sqrt{u_{11}} = 0.067$ Å, and for Si: $\sqrt{<u^2>} = 0.075$ Å.

Angular scan measurements through the [100]- and [110]- channeling direction for the V-rows were performed using 2 MeV He-particles elastically scattered from V-atoms and well separated in energy from those scattered from Si-atoms /3/. The calculated angular scan curves together with the measured values are shown in Fig. 1. The agreement between simulation and experiment at $\psi_{1/2}$ is within $0.02°$. For the [100]-direction the simulated curve is steeper than the experimental values at tilt angles above $0.8°$. For the [110]-direction the theortical curve is slightly above the measured values for tilt angles below $0.4°$. These deviations however are within the statistical accuracy of both the calculated and measured values.
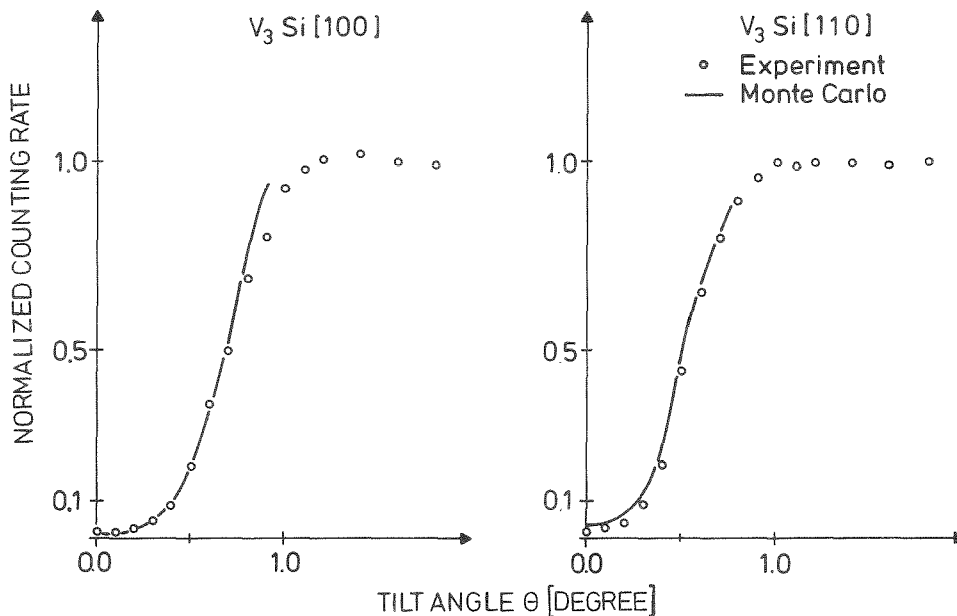
Fig. 1   Calculated and experimental angular scan curves through the [100]- and the [110]-channeling directions of V3Si. The He-ions are scattered from V-atoms at a depth of 470 ± 250 Å.

The ^{28}Si(d,p)^{29}Si-reaction with an incident beam energy of 1.7 MeV was used for angular scan measurements from the Si-rows. Due to the relative small energy loss of the protons the measurements have been performed in a depth region close to the surface within a width of about 3000 Å. Angular scan curves through the [100]- and [110]-channeling directions have been calculated and compared to the measured results in Fig. 2. The agreement is good for the $\psi_{1/2}$-values, however a large discrepancy is found by comparing the χ_{min}-values for the [110]-direction. If an amorphous layer of 20 Å was simulated in the calculations, the following results have been obtained: no change has been found for the $\psi_{1/2}$-[100]-value, however, the value for $\psi_{1/2}$-[110] was found to decrease by 0.03° · χ_{min}-[100] was found to increase from 7 % to 10 % and χ_{min}-[110] from 9 % to 12 %. This result is supported by the experimental observation that low χ_{min}-values are obtained after careful surface treatment only, whereas $\psi_{1/2}$-values are less sensitive to surface contamination. The calculated depth dependences of the critical angle and the minimum yield are in reasonable agreement with the measured results.
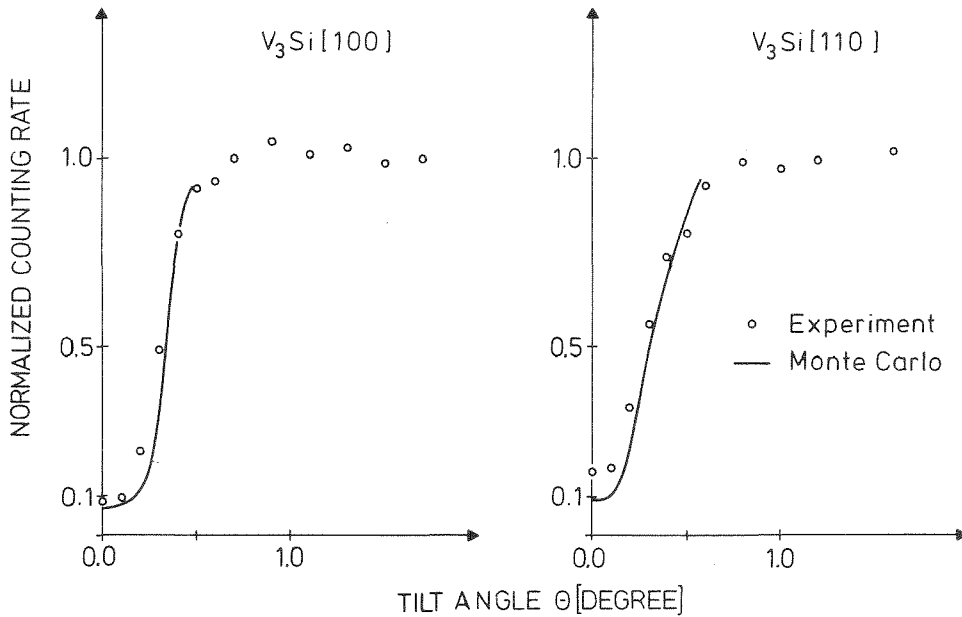
Fig. 2   Calculated and experimental angular scan curves through the [100]- and [110]-channeling directions. Protons from the ^{28}Si(d,p$_{10}$)^{29}Si-reaction have been used to measure the channeling data from the Si-rows.

From the good agreement between measured and calculated angular scan curves and depth dependence of $\psi_{1/2}$ and χ_{min} it is concluded that the models for the physical processes used in the computer program are sufficient to describe the channeling process in complicated crystal structures such as the A15-structure. As an extension of the binary collision model the interactions of the ion with all neighboured atoms in one plane have to be considered.

The anisotropy in the thermal vibrations of the transition metal atom influences the angular scan curves only slightly above the limit of accuracy of current measurements and calculations. Clearly, the computer calculation is the only possible way to study this influence on the channeling process.

References

/1/ R. Kaufmann, Kernforschungszentrum Karlsruhe GmbH, KfK 2638 (1978)

/2/ J.L. Staudenmann, P. Coppens, and J. Muller, Sol. State. Comm. 19, 29 (1976)

/3/ O. Meyer, Nucl. Instr. Meth. 149, 377 (1978)

4.12 Computer Simulation of Channeling Measurements on He-Irradiated V_3Si Single Crystals

R. Kaufmann and O. Meyer

A computer program developed previously /1/ for the simulation of channeling measurements has been extended to analyse damage structures in V_3Si. The damage has been produced by ion irradiation at room temperature with $4 \cdot 10^{16}$ and $1.5 \cdot 10^{16}$ He^+/cm^2 at energies of 300 and 50 KeV respectively. Depth profiles of the defects as well as the lateral distribution perpendicular to the channels have been included in the program, and have been varied until the measured backscattering yields in dependence of the incident beam angle could be reproduced by the calculation.

1. Lateral defect distribution in the transmission region

In experiments described previously /2/ disorder produced by 300 KeV He-ions in V_3Si had been analysed by 2 MeV He-ion channeling measurements. The 300 KeV He-ions penetrate a surface region of about 4000 Å with low energy loss. The particles are stopped at a depth of approximately 6000 Å where a direct backscattering contribution from displaced V- and Si-atoms had been observed. Angular scan curves from V-rows in the [100]- as well as in the [110]-channeling direction as performed in the near surface region revealed an appreciable narrowing of the angular width after implantation of $6 \cdot 10^{16} He^+/cm^2$ at room temperature.

As a defect model in the computer simulation it was assumed that all
V-atoms are displaced from their lattice sites. It was further assumed that
the displacements have a Gaussian distribution with rms-amplitudes of
0.05 Å perpendicular to the [100]- and [110]-channeling direction. The
results of the computer calculation are presented in Fig. 1 together with
the measured angular scan curves. Within the statistical accuary limit of
calculations and measurements good agreement is achieved.
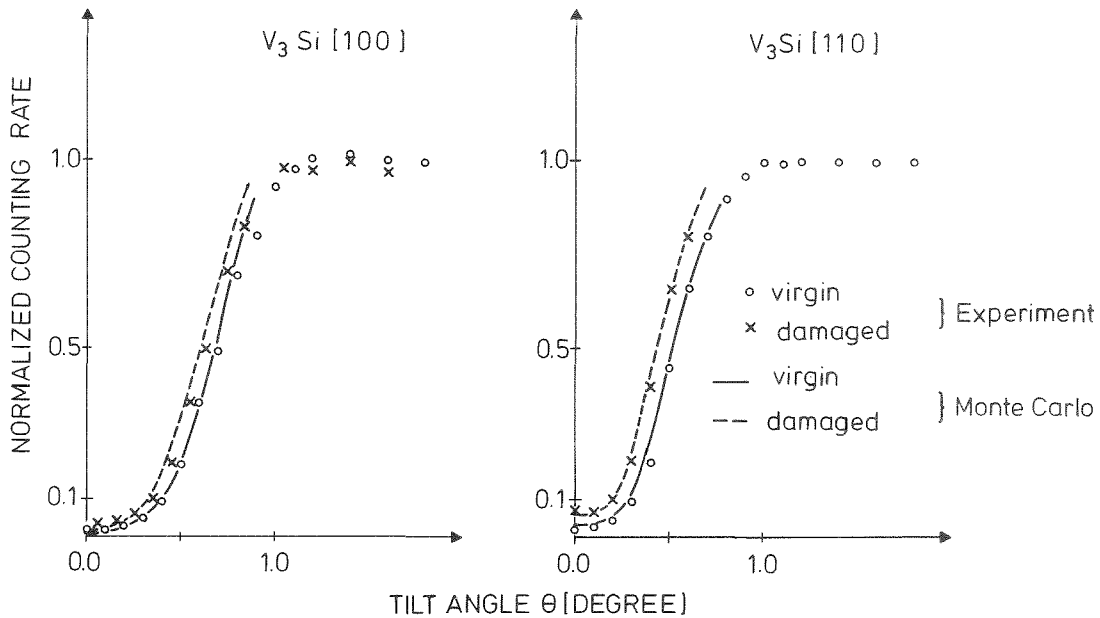
Fig. 1   Normalized angular scan curve at 500 Å below the surface through the
[100]- and the [110]-channeling directions using 2 MeV He-ions scattered
from V-atoms. Results are presented prior to and after irradiation with
$4 \cdot 10^{16}$ He+/cm2, 300 KeV at room temperature and are compared to calcu-
lated angular scan curves.

2. Lateral damage distribution at the end of the He-ion range

A direct backscattering component which was observed at the end of the
He-ion range indicated that a large amount of lattice atoms had been displaced
with displacement lengths larger than about 0.2 Å. The lateral distribution of
these displacements can be conveniently explored if the damage depth profile is
close to the surface. Therefore $1.5 \cdot 10^{16}$ He+/cm2 with a low energy of 50 KeV
have been implanted in V_3Si at random direction. The He-implanted V_3Si single
crystal has been analysed with 2 MeV He-particles. Increasing the transverse
energy of the probing beam by increasing the angle of incidence will vary the
spatial distribution of the channeled beam such that the flux peak in the
minimum potential will decrease and the density of trajectories close to the
rows will increase. Thus if the number of displaced atoms increases with de-

creasing displacement length the direct backscattering peak area will increase with increasing angle of incidence. A quantitative analysis however is difficult as a second contribution to the aligned backscattered yield exists. This contribution is due to ions being scattered from displaced atoms and thus being transferred from the channeled to the random beam.

In order to simulate the measured results with the computer program two different lateral defect distributions have been used: in a first model 10 % of the atoms have been assumed to be randomly displaced across the channel and in a second model a rectangular distribution of 50 % displaced lattice atoms was assumed with a width of 0.5 Å from the atomic rows. The depth distribution used has been calculated using a computer program from D.K. Brice /3/.

Experimental and calculated backscattering spectra of aligned crystals are compared in Fig. 2 and 3.
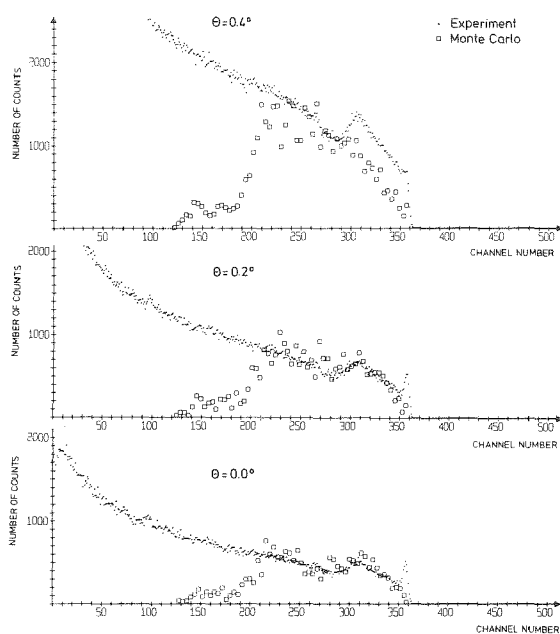
Fig. 2
Calculated and measured aligned spectra at various tilt angles between the [100] - direction and incident beam from a V_3Si single crystal after implantation of 1.5 · 10^{16} He^+/cm^2, 50 KeV at room temperature. As a defect model 10 % of the atoms have been assumed to be randomly displaced across the channel.
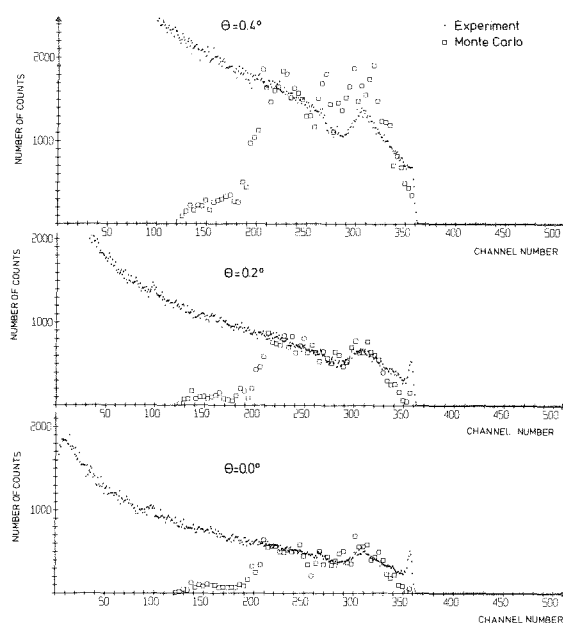
Fig. 3
Calculated and measured aligned spectra at various tilt angles between the [100]- direction and incident beam from a V_3Si single crystal after implantation of 1.5 · 10^{16} He^+/cm^2, 50 KeV at room temperature. As a defect model 50 % of the atoms have been assumed to have a lateral rectangular distribution with a maximum displacement amplitude of 0.5 Å.

This comparison shows that the spectrum at zero tilt angle can be described with both defect models. At larger tilt angles however it clearly favours the model where the number of displaced atoms increases with decreasing lateral displacement amplitude.

A lateral defect distribution is therefore not only observed in the transmission region but also in the region where the He-ions come to rest and produce a large number of displaced atoms. In this region the maximum displacement length used is $0.5 \overset{O}{A}$, a factor of 10 larger than in the transmission region.

The defect model is not yet optimized in regard of the most appropriate shape of the lateral distribution and is clearly not unequivocal. Nevertheless the above results prove the usefullness of the computer simulation calculations to analyse aligned backscattering spectra from damaged crystals with complicated crystal structures.

References

/1/ R. Kaufmann, Kernforschungszentrum Karlsruhe GmbH, KfK 2638 (1978)
/2/ O. Meyer and B. Seeber, Sol. State Comm. 22, 603 (1977)
/3/ D.K. Brice, Sandia Lab. Res. Report SAND 75-0622 (1977)

4.13 Epitaxial Growth of Sputtered V_3Si Thin Films

O. Meyer and R. Smithey

V_3Si bulk material has a transition temperature of $16.85^O K$ at stoichiometric composition /1/ and can be prepared in single crystalline form. Here we report on the conditions for the epitaxial growth of thin (500 to 1500 $\overset{O}{A}$) sputtered V_3Si films. A HF-sputtering system was employed with a composed V- and Si-target. The target geometry was optimized in order to get laterally homogeneous layers with a 3/1 ratio for V/Si over a length of 3 cm. The following parameters were used during deposition: HF-power 300 W, bias voltage 1300 V, Ar-pressure $1.3 \cdot 10^{-1}$ Torr. None of this parameters has a strong influence on the growth process and film properties. The films were deposited on hot single crystalline Al_2O_3-substrates and the substrate temperature T_s was found to be the most important parameter for epitaxial growth. Thin film X-ray technique and back-scattering and channeling technique have been used to explore the degree of epitaxy. In Fig.1 channeling spectra for samples prepared at different substrate temperatures are compared to a random spectrum. The minimum yield was found to decrease with increasing substrate temperature. From angular scan curves obtained for sample V-21 ($T_s = 1150°C$) the critical angle $\psi_{1/2}$ was found to be $0.72°$ and the minimum yield X_{min} was 19%.
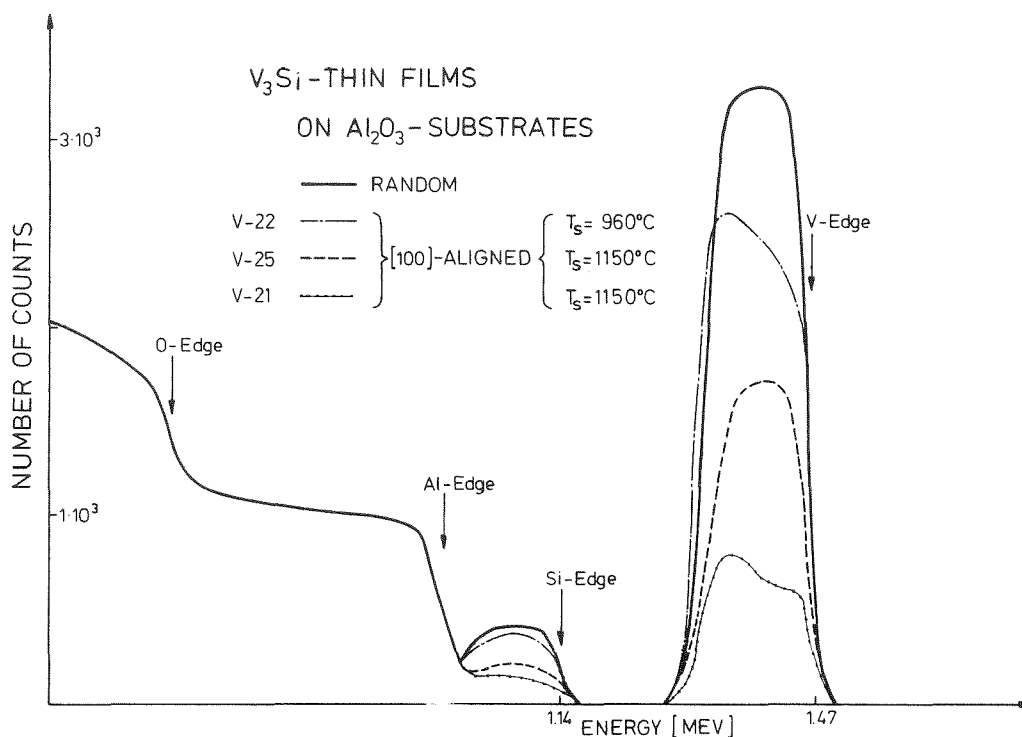
Fig. 1 Random and [100]-aligned spectra from 2 MeV He-ions backscattered from V_3Si thin films epitaxially grown on single crystalline Al_2O_3-substrates.

Using the measured χ_{min}-values, one can estimate the distribution of crystallite orientations as characterized by it's standard deviation σ from /2/:

$$\sigma = \left| \frac{\chi_0 - \chi}{\chi - 1} \right|^{0.5} \frac{\psi_{1/2}}{\sqrt{\ln 4}}$$

where $\chi_0 = 2$ % and $\psi_{1/2} = 0.75^\circ$ are the values

obtained for a single crystal /3/ ($\chi_0 [100] = 2$ %, $\psi_{1/2} = 0.72^\circ$). The factor $\ln 4$ is the conversion from full width at half height to standard deviation. From this equation σ is found to be 0.6° for sample V-21.

In Fig. 2 the superconducting transition temperature is given as a function of the electrical resistance ratio $r = \rho_{RT}/\rho_{20 \text{ K}}$. Samples with various T_c-values were obtained by varying T_s but keeping the V/Si ratio constant. At T_s below $880^\circ C$, with r-values smaller than 2, the films became polycrystalline and the A15 phase was detected with thin film X-ray technique. At higher temperatures the films were single crystalline with r-values of 20 close to values observed for bulk single crystals. The highest observed onset value of T_c was 16.5 K, which is slightly lower than the bulk value for stoichiometric V_3Si.
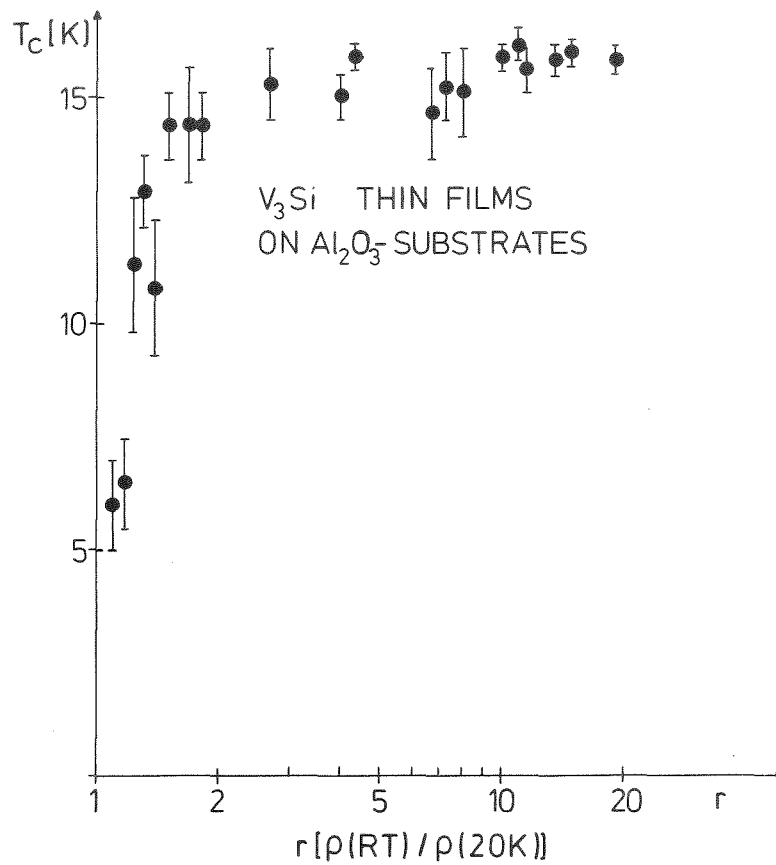
Fig. 2 T_c versus resistance ratio $r = \rho(RT)/\rho(20\ K)$ for different V_3Si
thin films grown at various substrate temperatures.

References

/1/ A. Junod, J.L. Staudenmann, J. Muller, and P. Spitzli, J. Low-Temp. Phys. 5,
    25 (1971)

/2/ D. Sigurd, R.W. Bower, W.F. Van der Weg, and J.W. Mayer, Thin Solid Films 19,
    319 (1973)

/3/ O. Meyer, Nucl. Instr. and Meth. 149, 377 (1978)

4.14 Preparation of Nb_3Si in Pure A15-Phase and Investigation of the

$Nb_3Ge_{1-x}Si_x$ System

E.L. Haase, R. Smithey, and O. Meyer

It has frequently been pointed out in the past that Nb_3Si, if made in the A15-phase, is a likely system for a high transition temperature T_c to superconductivity. This also holds for the pseudobinary compound $Nb_3Ge_{1-x}Si_x$ where one can expect high T_c values for high values of x. A_3B compounds with A15-structure and stoichiometric composition show a marked trend of rising T_c with decreasing lattice parameter a_o.

We have prepared thin ($\simeq$ 250 nm) films of Nb_3Si and $Nb_3Ge_{1-x}Si_x$ by the following four methods:

1. Simultaneous evaporation of two, and for the pseudobinary compounds three, elements onto hot substrates of sapphire, silicon and quartz.

2. Sputtering from a composite Nb and Si target.

3. Simultaneous evaporation of Nb and Ge with a silane (SiH_4) gas pressure of several times 10^{-5} torr.

4. Simultaneous evaporation of Nb and Ge onto hot Si-substrates. Strong Si-diffusion yields the pseudobinary compound.

Fig. 1 shows results for the pseudobinary phase $Nb_yGe_{1-x}Si_x$. The open circles show T_c versus composition as measured with backscattering for samples with pure or predominantly A15-phase. T_c drops slightly as x increases. Most samples were prepared with non-optimum composition, (y mostly being smaller than three as measured by Rutherford backscattering). Only the highest points are to be taken into acount, as T_c approaches asymtotically an optimum. The corresponding a_o-values did not show the expected decreasing trend. Beyond x = .44 we did not as yet succeed to prepare samples with detectable A15-phase. The triangles are values from samples with predominantly Ta_3Si structure.

In Fig. 2 information on Nb_3Si is summarized. It was prepared in essentially pure A15-phase. At 20 at% Si-content T_c is 9.3 K. The lattice parameter at 19 at% as determined by the procedure described in the following contribution is 5.126 Å and thus 0.04 Å below the value for Nb_3Ge at the same

composition. In the bottom half of Fig. 2a) T_c is shown versus Si concentration. Only the solid circles bear relevant information as these are measured on essentially pure A15-phase samples. As Nb can form solid solutions in Nb_3Si, only those samples are shown, which show no detectable Nb. The detection limit is about 3 at%. Both sputtered and evaporated samples are shown. In Fig. 2b) the corresponding values for a_o are given. The open circles show samples that have too large a lattice parameter on account of non-optimum growth conditions, or contain foreign phases that make a microscopic composition determination difficult, or both. Not all samples shown in Fig. 2a) were evaluated.

On the top right of Fig. 2b) a_o-values are shown for Nb_3Ge samples which were prepared under similar conditions. The a_o-values were evaluated by the same method. Below 25 at% Ge, a_o begins to rise as the larger Nb atoms are occupying Ge sites. When we extrapolate from the lowest point a_o to 25 at%, for Nb_3Si, using the slope from Nb_3Ge /3/, we obtain a value of 5.10 Å for the stoichiometric composition. This is the smallest value reported so far, but still higher than the emperical estimates of about 5.07.

Concerning the T_c-values one should notice that we are still far from stoichiometry at 25 at%. A reasonable extrapolation procedure for T_c is to take the value at a_o = 5.10 on the line connecting the points for Nb_3Sn (18.3 K, 5.30 Å) and Nb_3Ge (23.2 K, 5.13 Å) in a T_c vs. a_o plot. The result for Nb_3Si is 24 K.

The structure analysis shows that with increasing Si-contents and with increasing deposition temperature the competing phase with Ta_3Si-structure is preferentially formed. Rather extensive attempts to procedure more stoichiometric Nb_3Si in A15-phase have been unsuccessful. On this basis it is considered improbable that with the above methods a substantial increase in T_c will be obtained. For Nb_3Si, as shown in Fig. 1, there exist measurements of Pan et al. /1/ and Somekh and Evetts /2/ and others. The former sample was prepared by an explosive technique and is stated to contain about 5 % A15-phase. The highest T_c sample of ref. /2/ is stated to have a high content of foreign phases and was prepared at a substrate temperature about 400°C higher than ours. The quoted lattice parameter is too large to be compatible with our results for A15-type Nb_3Si. Moreover, when we increased our substrate temperature, the A15-phase ceased to form and the Ta_3Si-type phase was observed. These samples were super-conducting with T_c as high as 12.2 K, as shown in Fig. 1 (open triangles).

A15 Nb$_y$ Ge$_{1-x}$ Si$_x$

× Testardi et al.
⊕ Pan et al.
□ Somekh and Evetts
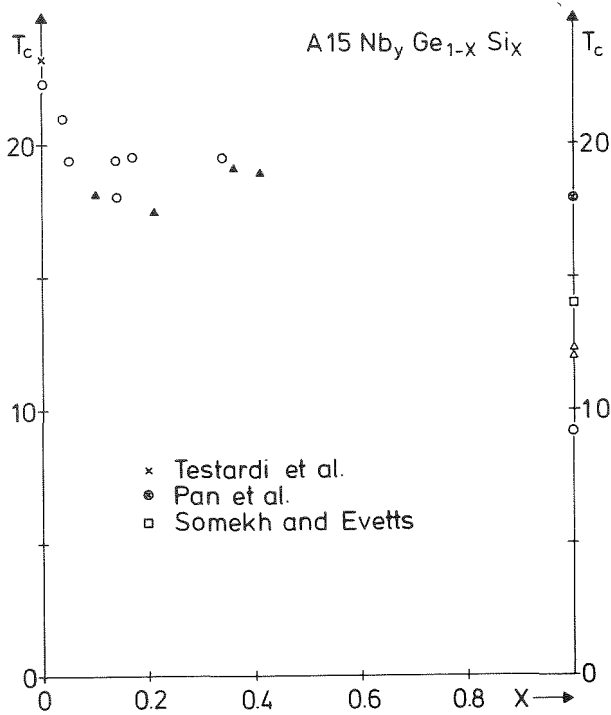
Fig. 1 T$_c$ vs. x for the Nb$_3$Ge$_{1-x}$Si$_x$ pseudobinary compound. Open circles have predominantly A15-phase.
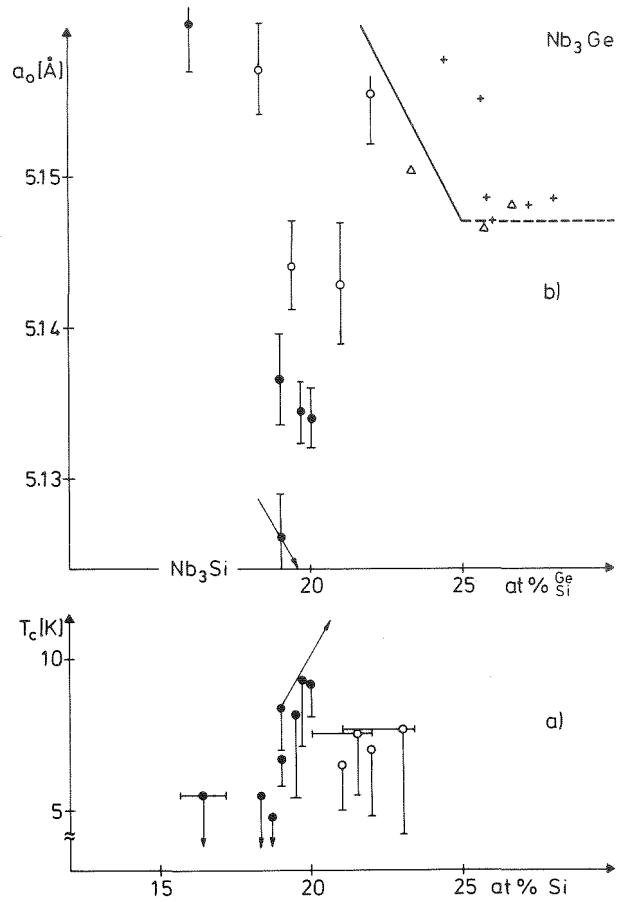
Fig. 2 T$_c$ and a$_o$ vs. at% Si (or Ge), respectively. The solid circles show the essential results and the arrows extrapolations as discussed in the text.

Our numerous observation of samples with T$_c$ as high as 19 K with no detectable A15-phase urge us to consider that there exists another high T$_c$-phase in the Nb$_3$Ge$_{1-x}$Si$_x$ and Nb$_3$Si systems, most probably of the under-stoichiometric Ta$_3$Si type.

References

/1/ V.M. Pan et al., JETP Lett. 21, 228 (1975)

/2/ R.E. Somekh and J.E. Evetts, Solid State Comm. 24, 733 (1977)

/3/ A.B. Hallak et al., IEEE Trans. Mag. MAG-13, 313 (1977)

4.15 Lattice Parameter Determination in Superconducting Thin Films

E.L. Haase

So far stresses in thin superconducting films prepared by evaporation or sputtering onto hot (≈ 850°C) substrates have generally not been taken into account in lattice parameter determinations. In the following it is shown that employing the usual extrapolation procedure can lead to errors that are an order of magnitude larger than the errors generally given in the literature. A method is proposed that allows to determine an average value for the lattice parameter and the magnitude of the stress.

The standard method to eliminate instrumental errors is to extrapolate the scattering angle Θ to $2\Theta = 180°$. This method however gives incorrect results for the lattice parameter, when layers are stressed thermally, i.e. due to different thermal expansion of a layer and a thick substrate.

Feder and Berry /1/ need an unstressed reference sample to determine the stresses. This method is generally not feasible for thin layers, because their lattice parameter varies as a function of composition, deposition temperature, method and rate and other parameters. Thus a method has to be worked out, that does not depend on unstressed reference samples.

Rather than using the extrapolation procedure, an alternate way to eliminate instrumental errors is to make a second exposure on the same film with a well behaved calibration sample like gold. Care has to be taken that both the samples and the calibration sample are precisely at the same position on the focussing circle and that they have comparable areal density to avoid an absorption correction. Using both the measured and the calculated positions of the gold reflexes one obtains a corrected film length dependent linear expression for the diffraction angle, in the present geometry $\Theta(°) = (L + A + B \cdot L)/4$.   The points in Fig. 1a) show $4\Theta - L$ vs. L for such a gold calibration and a least-squares-fit line through the points, with intercept A and slope B for the origin as a function of film length L. The slope is caused by instrumental errors like film shrinkage, but as these are the same for sample and calibration sample, they are eliminated by the above procedure.

Fig. 1b) shows the result when this procedure is applied to an aluminium powder sample. The points give the lattice parameter for the different reflexes, plotted as a function of the function $F = \cos^2\Theta/\sin\gamma\sin(2\Theta - \gamma)$ /1/, γ being the fixed grazing angle of incidence of the X-ray beam onto the target. The

line, a weighted linear least square fit through the points, should have a slope of zero. The deviation gives an indication of the accuracy of the method. The average lattice parameter $\langle A_O \rangle$ is in good agreement with the JCPDS-value of 4.0494.

Figs. 1c) and d) show the results of the same procedure for two Nb_3Ge layers prepared simultaneously under identical conditions, the only difference being that the layer 165IIS was deposited on sapphire and 165IIQ on silica with a small coefficient of thermal expansion. The lines are linear weighted least squares fits to the points. Their intercepts show that large errors can arise when the usual linear extrapolation procedure is applied to stressed layers.

The points, and the curves dashed line through them, in Fig. 1c) show the typical appearance of a compressively thermally stressed layer. Thermal stress has the angular dependence $\varepsilon_\phi = \Delta A_T \cdot \cos 2\phi$, ϕ being the angle between the normal to the surface of the layer and the normal to the lattice planes. In the derivation the Poisson number is taken to be 1/3. ε_ϕ is zero at $\phi = \Theta - \gamma = 45^O$, which corresponds to F = 1.97 for $\gamma = 10^O$ as shown in Fig. 1c). ΔA_T is the magnitude of the thermal stress and of other stresses that have the same angular dependence. As discussed later, intrinsic stresses also vanish at $\phi = 45^O$. Hence, to obtain an average value for the lattice parameter needed for comparisons, one must draw or fit a smooth line through the experimental points after instrumental corrections and take the value at $\phi = 45^O$.

When this is done for the two films, we obtain $\langle A_O \rangle$ = 5.155 for Fig. 1c) and 5.156 for 1d), in excellent agreement as expected. The method can readily be adapted to diffractometers with Seemann-Bohlin focussing. The Bragg-Brentano arrangement it unsuitable, as it allows reflections only from lattice planes parallel to the sample surface.

If one wants to determine kind and magnitude of the stress one has to go further. The magnitude of the thermal stress ΔA_T is determined by a $\Delta A_T \cos 2\phi$ least squares correction to the experimental lattice parameter values. After the thermal correction is carried out, there still remains in most cases a comparable departure from a constant value for a_O.

Such stresses are known under the generic name intrinsic /2/. In the present study, all of the numerous films measured showed that the thermally corrected a_O-values vary linearly with F. In the absence of detailed models, it is most reasonable to use this empirical fact as a basis. If we assume that all grain orientations are equally probable (the X-ray films can be tested for this) then on the basis of symmetry considerations we also have to take the value at $\phi = 45^O$.

GOLDEICHUNG
PROBE NR. NB1I
A= 51.0887 B=-2.97808E-03
a)

PROBE NR. 165IIS <A0>= 5.1547
DELTA AT= .0000 AT(0)= 5.1521 c)

PROBE NR. 221 <A0>= 4.0491 b)
DELTA AT= .0000 AT(0)= 4.0500

PROBE NR. 165IIO <A0>= 5.1597 d)
DELTA AT= .0000 AT(0)= 5.1785
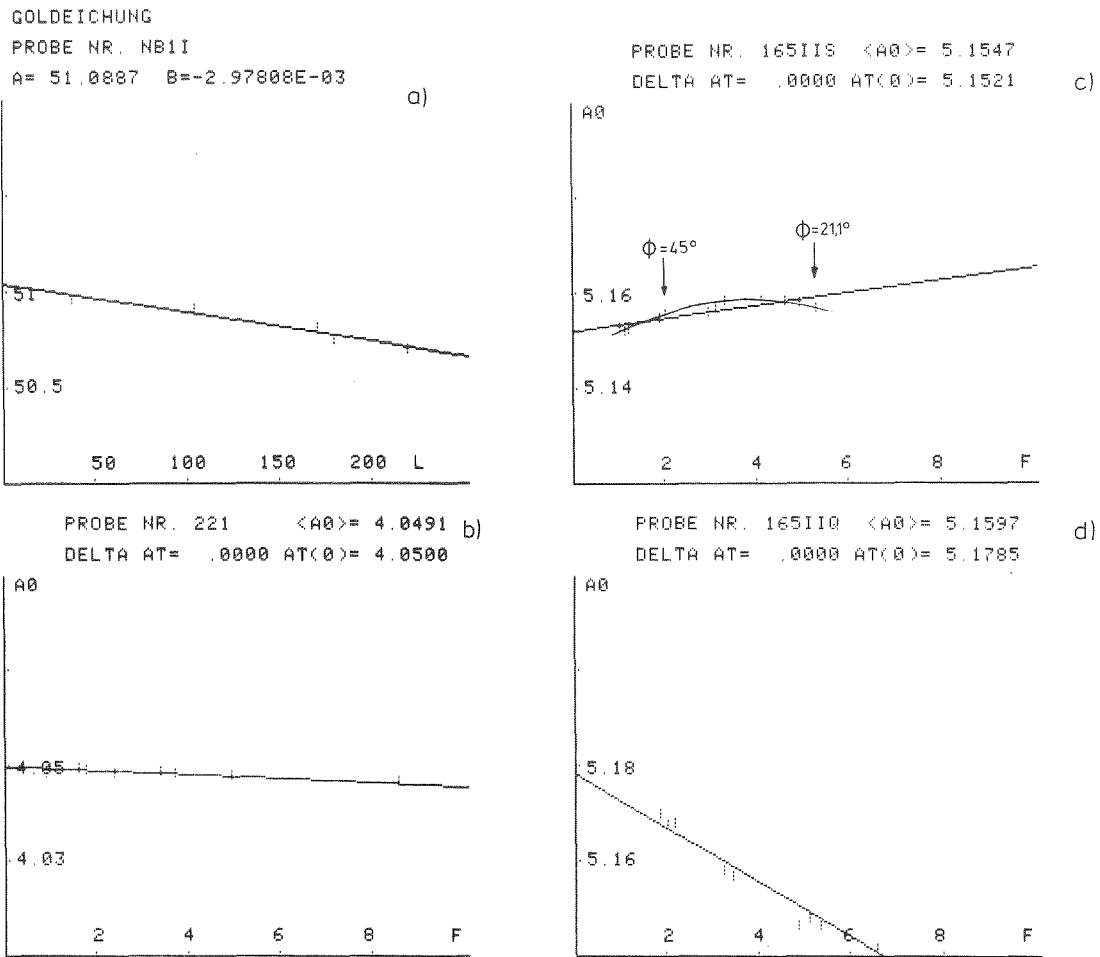
Fig. 1   a) Typical film length L dependent origin (4θ - L) for instrumental
              correction.

           b) Test of method for unstressed Al-powder sample.

           c) Compressively stressed sample on sapphire.

           d) Tensile stress for sample on silica substrate.

The adopted procedure is to make a linear least square fit to the a_o-values.
The magnitude of the two kinds of stress are quite different for evaporated and
sputtered layers.

References

/1/ R. Feder and B.S. Berry, J. Appl. Cryst. 3, 372 (1970)

/2/ R.W. Hofmann in "Physics of Nonmetallic Thin Films", C.H.S. Dupuy and
    A. Cachard eds., Plenum Press, N.Y., 273 (1976)

4.16 Annealing Tests on A15 Superconducting Layers

E.L. Haase and R. Smithey

It has generally been observed that annealing of bulk A15 superconductors like Nb_3Al, Nb_3Sn or V_3Si for periods of days at about half the melting temperature increases T_c by about 1 K and improves long range order. It is of interest to perform such tests on thin films of A15-superconductors prepared by simultaneous evaporation or sputtering.

The special situation in annealing films of Nb_3Ge or Nb_3Si is that these materials are metastable and that, when sufficient energy is imparted, it is to be expected that these systems revert to a status of lower free energy, which in practice means lower T_c.

The tests were carried out in the apparatus used for the simultaneous evaporation. The samples were clampled to a Mo-block, the back of which was heated with an electron gun. To avoid contamination by diffusion from the residual gas, the annealing was performed at a vacuum of typically $2 \cdot 10^{-8}$ Torr for periods of 1 min to 2 h.

For Nb_3Ge no change in T_c or lattice parameter was observed for temperatures of less than $750^{\circ}C$. In about 25 tests on Nb_3Ge or Nb_3Si layers, there was in no case an increase in T_c. When the temperature was raised to $800^{\circ}C$, the Rutherford backscattering analysis showed that the layers started to decompose. The germanium diffuses to the surface and sublimes.
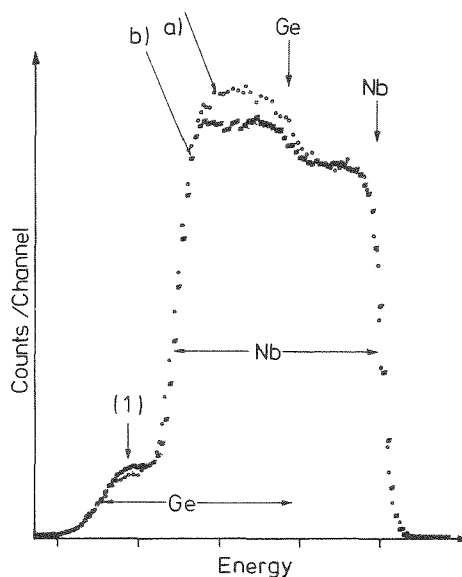
Fig.   Rutherford backscattering spectra of a Nb_3Ge layer. The height of the Nb and Ge /1/ edges are proportional to the at% concentration: a) as prepared, b) after annealing for 1 h at $850^{\circ}C$ and 1 h at $950^{\circ}C$. The decrease in Ge-contents is substantial for the front of the layer.

The result is described in detail in the caption of the figure. Inter-mediate results show an enhanced Ge-concentration at the surface. While most of the layer is strongly depleted, the backside (1) is actually enhanced in Ge-contents, indicating that Ge also diffuses towards the substrate interface. The X-ray measurements support the observation of decomposition: while the considerably weakened A15-reflexes persist, most of the intensity after annealing is due to the competing Nb_5Ge_3 α-phase.

The A15 phase in Nb_3Si layer annealed for 1/2 h at 750° transformed in-to the Ta_3Si phase.

Only in a single case, a $Nb_{.80}Si_{.10}Al_{.10}$ sample annealed at 690^OC for about 1/2h, a T_c increase of 1 K was observed.

4.17 The Superconducting Transition Temperature of $Nb_3(Nb_{0.2}Ge_{0.8})$ after Implantation of Ge^+-Ions

J. Geerk, G. Linker, M. Kraatz, and B. Scheerer

Many high temperature superconductors show a low transition temperature T_c when prepared in bulk form by using conventional methods like arc melting. The decrease in T_c is mostly correlated with a deficiency of one component by the melting process. Examples are the B1 superconductors NbC and NbN, which always have a certain lack of C or N, respectively. In this case it has been shown /1/, that the deficiency of carbon or nitrogen can be overcome by ion implantation of these elements. The most interesting superconductor whose properties are quite sensitive to deviations from stoichiometry is Nb_3Ge with the highest known transition temperature of 23.2 K. Bulk material of Nb_3Ge produced by melting the components becomes superconducting at about 6.5 K only. Geller /2/ found that this material crystallizes in the A15 structure with a deficiency of germanium of 25 %. Up to now the high T_c phase of Nb_3Ge has only been produced by sputtering, evaporation or chemical vapour deposition on hot substrates. In this work it was investigated whether it is possible to raise the transition temperature of bulk Nb_3Ge by ion implantation of Ge-ions.

Bulk material with the nominal composition Nb_4Ge was produced by melting a mixture of 4 parts Nb and 1 part Ge in an RF oven as described in detail in /3/. A part of the resulting material was pulverized and analyzed by X-ray diffraction. From the diffraction lines it could be concluded, that the sample nearly completely consisted of A15 material, the content of other phases being lower than 5 %. The lattice constant was determined to be 5.162 Å. The physical density ρ of the sample has been determined by measuring its buoyancy in different liquids with the result $\rho = 8.61 \pm 0.025$ g/cm^3. From the density and the measured lattice constant it was confirmed that the composition of the unit cell is of the form $Nb_3(Ge_{0.8}Nb_{0.2})$ and not $Nb_3Ge_{0.75}$. Nb-atoms occupy the sites of the lacking Ge-atoms.

After polishing and etching the sample was cut into pieces with dimensions $12 \cdot 5 \cdot 1$ mm^3. These samples were then implanted at room temperature with Ge^{++}-ions of 700 keV and a fluence of $8 \cdot 10^{16}$/cm^2 and Ge$^+$-ions of 350 keV and $4 \cdot 10^{16}$/cm^2. The transition temperature was measured resistively. Directly after implantation the samples showed no T_c increase. To remove radiation damage the samples were annealed in a bakeable UHV-vacuum system at temperatures between 400 and 800°C. The sample temperature was controlled by a thermocouple. The annealing time was 2 h. The figure shows T_c versus the annealing temperature. Between 600 and 700°C T_c increases to about 16.4 K. At higher annealing temperatures a T_c-decrease is observed. This decrease is possibly due to diffusion of the implanted germanium. The results reported here are consistent with the findings of Sweedler et al. /4/. They found between 600°C and 700°C the main T_c recovery of neutron irradiated Nb_3Ge samples produced by chemical vapour deposition.
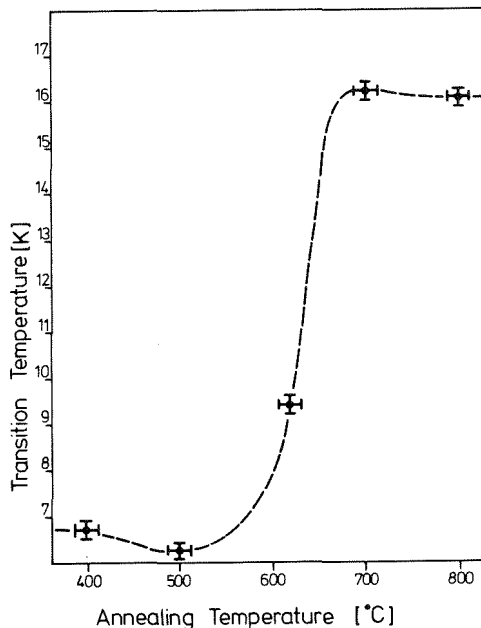
Fig.

The superconducting transition temperature of Ge-implanted $Nb_3Ge(Ge_{0.8}Nb_{0.2})$ as a function of annealing temperature

The results show, that with ion implantation it is possible to produce of the metastable high T_c phase of Nb_3Ge despite the fact, that in the starting material the Ge "vacancy sites" are occupied by Nb atoms.

References

/1/ J. Geerk and K.-G. Langguth, Solid State Comm. 23, 83 (1977)

/2/ S. Geller, Acta Cryst. 9, 885 (1956)

/3/ B. Scheerer and D. Ewert, this report, p. 112

/4/ A.R. Sweedler, D.E. Cox, S. Moehlecke, R.H. Jones, L.R. Newkirk, and
    F.A. Valencia, J. Low Temp. Phys. 24, 645 (1976)

4.18 Preparation and Superconductivity of Sputtered Nb_3Al-Films

O. Meyer, G. Linker, and R. Smithey

DC-sputtering onto hot substrates at high sputtering gas pressures ($\sim$ 0.1 Torr) and low bias voltage ($\sim$ 750 V) was applied to synthesize high T_c superconductors e.g. Nb_3Ge /1,2,3/. The highest T_c-values of 14.7 K reported up to now for sputtered Nb_3Al-films /3/ however were below those observed for bulk samples [T_c^{max} (as cast): 17.5 K, T_c^{max} (annealed): 18.5 K].

We have optimized a HF-sputtering system in regard to the preparation of high T_c Nb_3Al with A15 structure. The geometry of the composed Nb and Al-target was chosen to produce thin NbAl-layers on to heated Al_2O_3-substrates with a 3 to 1 composition of Nb to Al over a length of about 2 cm. The depth dependence of the composition was measured with Rutherford backscattering. Inhomogeneities in composition could be attributed to variations of the Al-sputtering yield which in turn was found to depend on the residual gas pressure and the cooling efficiency of the Al-target. The T_c-values of the layers were found to depend strongly on the substrate temperature, on the Ar-gas pressure in the discharge and on the discharge power.

In Fig. 1 the T_c-values are given as a function of the Ar-gas pressure. The highest T_c-values of about 17.5 K with onset values of 18.2 K were obtained at an Ar-pressure of $1.5 \cdot 10^{-1}$ Torr. The remaining sputtering deposition parameters of these films were: substrate temperature: $870°C$; bias voltage: 700 V; power: 100 W; deposition rate: 2 Å/s; target-substrate distance: 2.5 cm. The layers were homogeneous in composition and consisted of pure A15 phase. The smallest lattice parameter observed was 5.188 Å which is close to the bulk value for stoichiometric material (a = .1835). The observed T_c-values are comparable to those found for as cast bulk material. Annealing of the films at temperatures between 600 and $800°C$ did not result in an increase of T_c as observed for bulk material. In contrast, T_c was found to decrease at these temperatures. As a possible explanation it is assumed that due to the small Nb_3Al grain size in these films Al easily precipitates at grain boundaries.
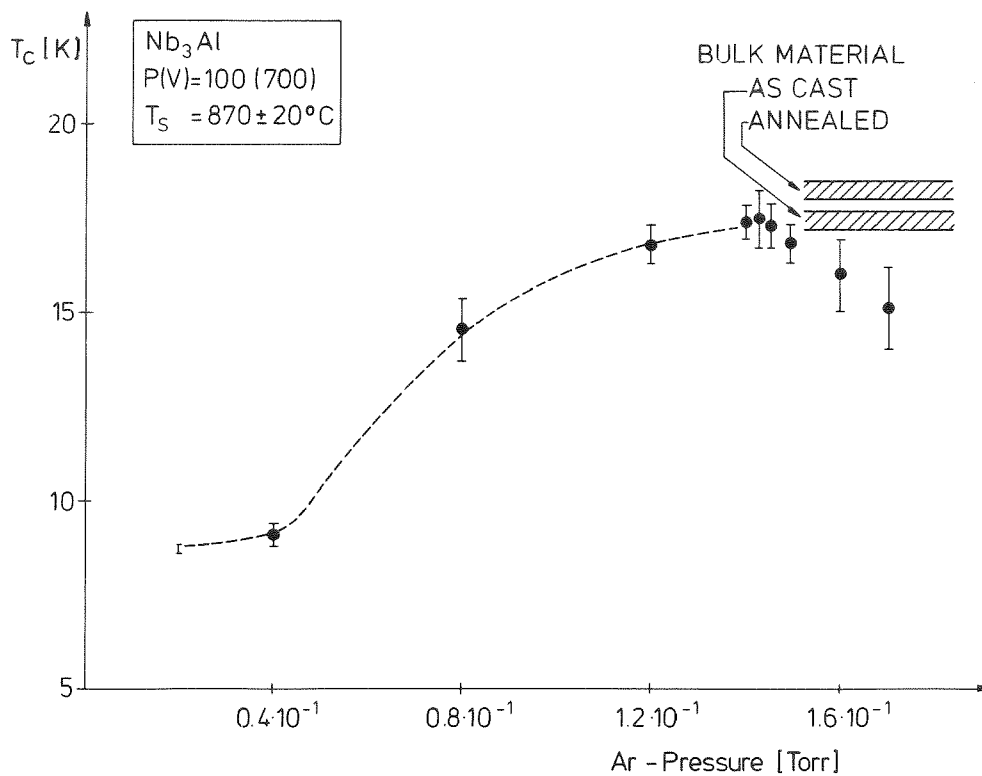
Fig. 1　T_c-values of sputtered Nb_3Al-films in dependence of the Ar-pressure in the HF-discharge during deposition

In Fig. 2 the T_c-values are plotted versus the electrical resistivity ratio $r = (\rho_{RT}/\rho_{20\,K})$. T_c decreases with decreasing r-values below 1.2. Films with low r-values were produced under non-optimized growth conditions, especially at low substrate temperatures. X-ray measurements revealed an increase of the lattice parameter a_o with decreasing r. From similar dependences

of a$_o$ on r or T$_c$ on r as observed for other materials with A15 structure by varying the growth conditions or for He-irradiated layers, the existence of a universal defect structure had been concluded /4/. As-grown Nb$_3$Al evidently follows the same general rule.
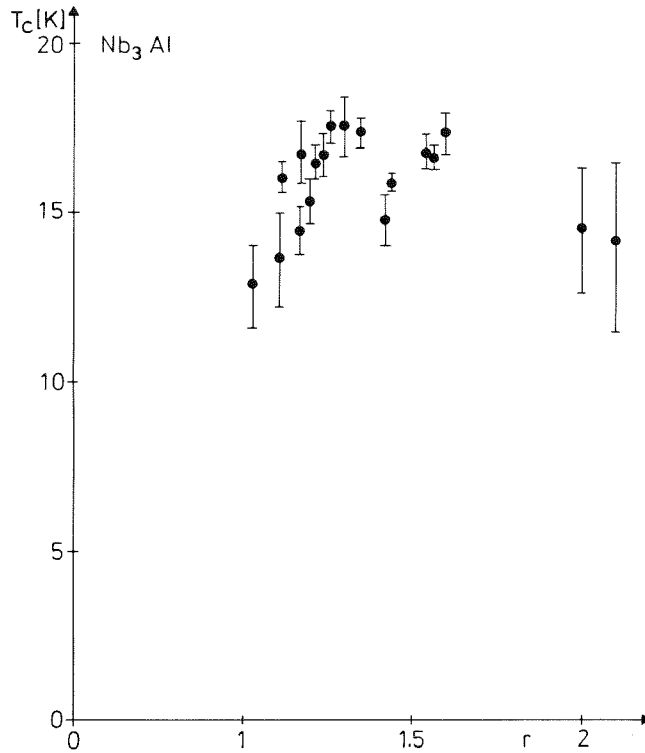
Fig. 2   T$_c$-values of sputtered Nb$_3$Al-films in dependence of the residual resistivity ratio r = $\rho_{RT}/\rho_{20 \text{ K}}$

References

/1/ J.R. Gavaler, Appl. Phys. Lett. 23, 480 (1973)

/2/ L.R. Testardi, J.H. Wernick, and W.A. Royer, Solid State Commun. 15, 1 (1974)

/3/ F.J. Cadieu and N. Chencinski, J. Low Temp. Phys. 28, 535 (1977)

/4/ L.R. Testardi, J.M. Poate, and H.J. Levinstein, Phys. Rev. B15, 2570 (1977)

4.19 Surface Preparation of Superconductors by Ion Etching

J. Geerk

A clean surface is an important condition if the most powerful method for the determination of superconducting parameters, electron tunneling, is hoped to be applied successfully. Also the method of high energy particle channelling, which in future will be used intensively for the characterization of defect structures of superconductors is dependent on a clean, oxide-free surface. As one component of most high T_c superconductors is the element niobium or vanadium, the surfaces of such superconductors are usually contaminated by oxides of these elements. To remove these oxides thermally temperatures in the 2000^oC region are required in an UHV-environment. In this way clean surfaces on niobium can be produced. However, the more interesting high T_c superconductors are compounds (like NbC, NbN, Nb_3Sn, Nb_3Al, V_3Si) which start to decompose far below 2000^oC. Therefore other surface cleaning methods have to be applied. A possible method is ion etching combined with subsequent annealing of the ion bombardment induced surface damage. Such an ion etching apparatus has been built up and is described in the following.

Fig. 1 shows a photograph of the experimental setup. The surface of the sample (a) is bombarded with Ar^+-ions with an energy of about 400 eV produced in the ion gun (b). The angle of incidence is about 45°. The sample rests in the boat of an electron gun (c). After bombardment the sample is heated up by the electron gun to a temperature sufficiently high for annealing. Typical annealing temperatures are 1300^oC for NbC and 1200^oC for V_3Si. Not included in the photograph for clarity is a liquid nitrogen cooled copper shield between the ion gun and the sample. The shield is provided with an opening through which the ion beam passes to strike the sample. The shield serves to protect the ion gun from stray electrons of the electron gun and to improve the vacuum conditions during annealing. The whole arrangement with the electrical and liquid feed throughs is mounted on a CF-flange NW 200. The vacuum chamber is a double T-piece with 4 CF-flanges NW 200. The chamber is evacuated by a 400 l/sec turbomolecular pump. A final pressure of $2 \cdot 10^{-10}$ Torr is routinely achieved after baking at 300^oC.

The ion gun is an electron impact source which needs a certain overall argon pressure for optimum performance. Fig. 2 shows the current density on the sample as a function of argon pressure. The optimum pressure is about

$1.5 \cdot 10^{-4}$ Torr. It is obvious that argon gas of highest available purity
(99.999 %) has to be used in order to avoid contamination of the sample
surface by impurities from the sputter gas. The maximum current density is
sufficient to remove a 2000 Å thick niobium oxide layer within 1 hour.
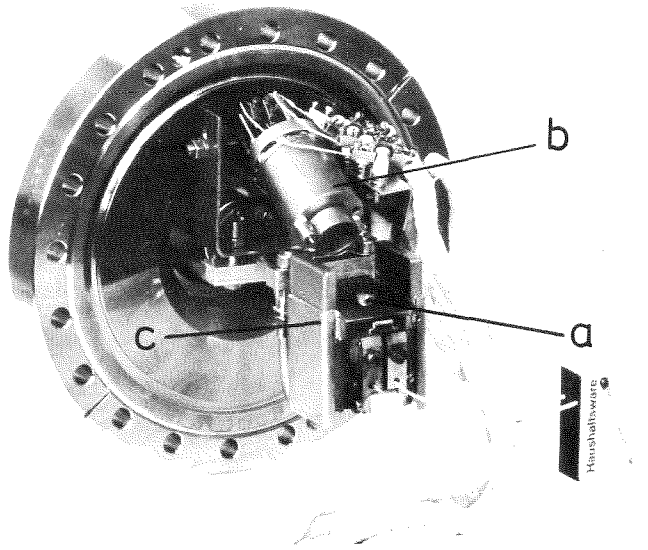
Fig. 1   Photograph of the ion etching apparatus. (a) sample, (b) ion gun,
(c) electron gun
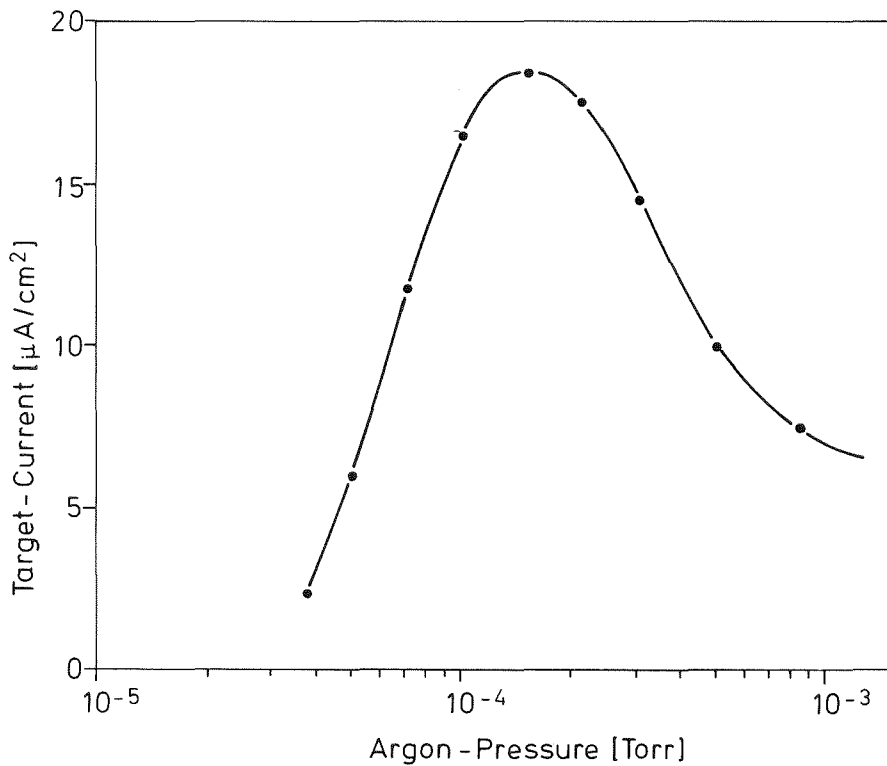
Fig. 2   The current density on the target as a function of argon pressure.

When the argon flow is switched off after bombardment the pressure decreases down to $1 \cdot 10^{-9}$ Torr within fractions of a second. During the following annealing process the pressure raises typically to $3 \cdot 10^{-9}$ Torr and then decreases to about $5 \cdot 10^{-10}$ Torr during the cooling down period. The results of a test series with NbC single crystals for tunneling experiments are described elsewhere /1/.

Reference

/1/ J. Geerk and B. Scheerer, this report, p. 86

4.20 Depth Profiling of Oxygen in Oxidized Ceramic Si_3N_4 with the Back-scattering Technique

J.M. Lombaard[a] and O. Meyer

[a]Dept. on Physics, University of Pretoria, South Africa

Abstract

The internal oxidation of reaction sintered Si_3N_4 during creep measurements at high temperatures has been measured with the MeV ^{4}He backscattering technique. A computer program has been used to generate theoretical spectra which are fitted to the experimental spectra and thus determine the composition. The measurements reveal that the bulk material is contaminated with calcium and iron which diffuse to the surface during the heat treatment. At the surface the material is completely oxidized to SiO_2 and an appreciable amount of oxygen has been diffused throughout the whole material.

4.21 Single Crystal Growth and Sample Preparation

B. Scheerer and D. Ewert

Growth of δ-NbN$_{1-x}$ Single Crystals

For phonon dispersion measurements of NbN by inelastic neutron scattering, we started to prepare face-centered δ-NbN single crystals.

We had no success by earlier zone melting experiments with hot pressed NbN-powder rods /1/. Because of the high equilibrium N_2-gas pressure at the melting point of NbN, this method yields only a nitrogen deficient material consisting of both the β- and γ-phase. Furthermore it must be taken into consideration that there is a phase transition to the ϵ-phase which can be avoided by rapid quenching (see C. Politis, Constitution Diagram of the System Nb-N) /2/. Therefore we followed a nitration method described by Christensen /3/.

Nb single crystal disks 9 mm in diameter and about 3 mm thick were cut from a zone melted Niobium single crystal. These disks were annealed at various temperatures around 1900°C in a N_2-atmosphere of 20 bar for at least 150 hours. The Nb crystal disk was suspended at a tungsten wire and heated by radio frequency. Temperature was adjusted and controlled throughout the nitrating duration by a pyrometer. The N_2-gas had a purity better than 99.9995 Vol.%. O_2- and vapour-impurities were reduced by a "Oxisorb"-gas cleaner. The nitration of each sample was stopped by switching off the generator power. Because of the small sample volume and a N_2-gas pressure of 20 bar, the sample cooled down very quickly. The characterisation of the samples by a θ-2θ-neutron diffraction scan showed in two cases, that the produced NbN$_{1-x}$ single crystals were entirely cubic δ-phase. The lattice constant as determined by X-ray diffraction was a = 4.377 $\overset{\circ}{A}$, by neutron diffraction a = 4.379 $\overset{\circ}{A}$. The superconducting transition temperature was T_c = 14.0 - 14.2 K. From these values we determined the N to Nb ratio as .82 /4/.

We shall continue these investigations with the aim to obtain single crystals with higher N concentration.

Nb$_3$(Ge$_{0.8}$Nb$_{0.2}$)-Alloys

For measurements of the phonon density of states in niobium-germanium alloys, we prepared bulk samples with the A-15 structure. From neutron diffraction measurements the contamination by other phases was estimated to be less than 5%.

Nb and Ge have been mixed in the ratio of 4 : 1 corresponding to $Nb_3(Ge_{0.8}Nb_{0.2})$ and molten in a cold crucible. The weight of each sample was about 35 gramm. The superconducting transition temperature of the samples was $T_c = 6.5$ K.

Pd-Alloys

For measurements of the magnetic field at interstitial sites in PdFe- and PdNi alloys by μ^+ spin rotation, we prepared samples which had the shape of spheres.

The starting material was molten several times in a cold crucible to get a homogeneous distribution of the alloyed constituents. After this we cut spheres with diameters of about 17 mm and 12 mm, respectively, by spark cutting (Fig.).
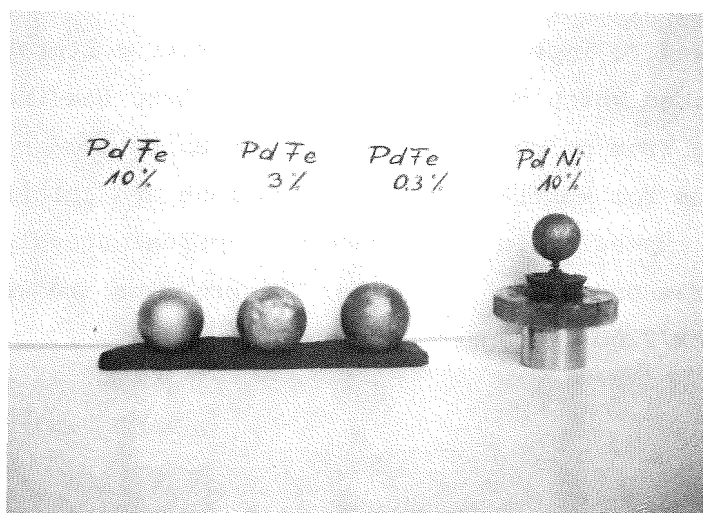
Fig.   Spheres of Pd-alloys

References

/1/ B. Scheerer, in Prog. Rep. Teilinst. Nukl. Festkörperphysik, Ges. f. Kern-
    forschung, KFK 2538, 134 (1977)

/2/ C. Politis, Kernforschungszentrum Karlsruhe GmbH, KfK-Ext. 6/78-1 (1978)

/3/ A.N. Christensen, Acta Chem. Scand. A31, 77 (1977)

/4/ L.E. Toth, Transition Metal Carbides and Nitrides, Vol. 7. Academic Press,
    New York and London, p. 94 Fig. 16, p. 221 Fig. 3 (1971)

5. DATA PROCESSING

5.1 Interactive Computer Graphic Methods of the Direct Determination of the Phonon Frequency Spectrum by Inelastic Scattering of Neutrons from Polycrystalline Samples

W. Abel

Ges. f. Kernforschung, KFK <u>2481</u> (1977)

Abstract

An on-line graphic display facility has been employed for the determination of the phonon frequency spectrum from inelastic coherent or incoherent scattering data of polycrystalline samples. One of the present interactive graphic programs is based on Egelstaff's method allowing to analyze the experimentally observed scattering law $S(\alpha,\beta)$. An interactive version of the LEAP computer code is used to improve the frequency spectrum iteratively. A second program is described which may be applied to analyze the inelastic coherent scattering data from polycrystalline samples using Bredov's method of averaging. Corrections for multi-phonon contributions are calculated, using the conventional phonon expansion in the incoherent approximation. A detailed description of the program operations is given. The programs are written in FORTRAN IV and use an IBM/2250-1 graphic display unit.

5.2 Tayloring of BASIC Interpreter Systems for the Experimentators

G. Ehret

BASIC is implemented as an interpreter system /1/. For some operation typical for data reduction in physical research environment the computing speed is too slow. To overcome the bottle necks (varying in different experiments) a number of assembly routines have been written. Selection of these routines to built a specific BASIC system is done by software switches. The same table is also used to selected the driver routines for the hardware installed in the computer for a specific experiment.

The table with the software switches is input file for an assembly under condition using the macro assembler /2/. The resulting output file is used for an automatic library call during the load process for the new tailored BASIC-interpreter.

In order to reduce drastically the memory space needed for these routines (typical 8 kBytes) a method has been developed to expand this very useful and reliable procedure to an arbitrary number of overlay modes and overlay segments in the load process. The implementation is done in collaboration with the Institut für Angewandte Informatik und Formale Beschreibungsverfahren of the University of Karlsruhe.

References

/1/ Data General Corp. NOVA EXTENDED BASIC System Manager Guide, No. 093-000119-02 C19
/2/ Data General Corp. MACRO Assembler User's Manual, No. 093-000081-04

5.3   Real-Time-Process-BASIC

G. Ehret and H. Hanak

The adaption of the "Extended BASIC" of Data General for the NOVA-Computer to the needs of the experimentators and experiments has been proceeded. The status achieved can be defined that as we have a Real-Time-Process-BASIC:

i)   External events can be prepared to interrupt the BASIC program. Thus there are planes of interrupt activity

   a.   on hardware level
   b.   on system level
   c.   on BASIC level

   The BASIC programmer can control (as far as useful) the activity of all levels. But most efficiently he can write the programs that match the interrupts in the BASIC language. The method of implementation has been described elsewhere /1/.

ii)   Software timer and clocks are implemented and are avialable to the BASIC programmer. Thus he can schedule delayed and/or periodic tasks programmer in BASIC.

   The Process-BASIC system is running on more than 30 installations. It may be termed "field proven".

Reference

/1/ G. Ehret, W. Karbstein, and B. Volk, in Annual Report Teilinst. Kernphysik,
    Ges. f. Kernforschung, KFK 2223, 126 (1975)

5.4   Mega-Channel-Kicksorter   A S S T R O

G. Ehret, H. Hanak, and H. Richelsen

ASSTRO (Automatisches Summieren von Spektren auf einem TROmmelspeicher, i.e. automatic accumulation of spectra of a drum) /1/ has been improved in hardware and software. Special drum controllers have been built, using the proven multiwire technique, to meet all expected programs in reliability of the system. The cards are operational.

As a preparation of the general byte-buss of the NOVA computers, /2/, the software driver for the papertape reader and puncher has been incorporated into the operating system. Data rate achieved for command and data exchange is about 5 kByte/sec. This is sufficiently fast for communication purposes, having in mind that data totalisation is not seriously affected by this process.

A new concept for a mega-channel-kicksorter is discussed elsewhere /3/.

References
/1/ G. Ehret, in Prog. Rep. Teilinst. Nukl. Festköprperphysik, Ges. f. Kern-
    forschung, KFK 2538, 138 (1977)
/2/ G. Ehret, this report, p. 117
/3/ G. Ehret, in Annual Report Teilinst. Kernphysik, Ges. f. Kernforschung,
    KfK 2686 (1978)

5.5   A New Direct Path to MIDAS-Data

G. Ehret, H. Hanak, H. Richelsen, and H. Sobiesiak

The CDC computer, main part of the old MIDAS system, has been taken out of operation. Access to the ASSTRO-data is achieved now exclusively through the NOVA computer MIDAS II /1/. This computer has been equipped with a Multi-User

BASIC interpreter system allowing a great deal of experimental data evaluation at different locations in the reactor hall and in the institute building. Final data evaluation is still done at the central IBM computer because of the well tested evaluation programs available there /2, 3, 4/.

Programs running already on the NOVA are

1. ESP   spectra evaluation on video display
2. EINFON   one phonon evaluation
3. MUPHOCOR   multiphonon evaluation using Bredov's method /2/.

These programs are written in FORTRAN and BASIC. Partly they consist of chained BASIC and/or FORTRAN programs modules. While on the old MIDAS only one user from one terminal had access to the whole system, with the new system only during execution of a FORTRAN phase the Multi-User-BASIC is suspended. To allow interactive data evaluation, facilities for task scheduling and for processing user interrupts have been implemented in this Multi-User BASIC interpreter system /5/.

References

/1/ G. Ehret, H. Hanak, and H. Richelsen, in Prog. Rep. Teilinst. Nukl. Festkörperphysik, Ges. f. Kernforschung, KFK 2183, 1I1 (1975)

/2/ J.-B. Suck and W. Reichardt, in Prog. Rep. Teilinst. Nukl. Festkörperphysik, Ges. f. Kernforschung, KFK 2183, 94 (1975)

/3/ W. Abel, in Prog. Rep. Teilinst. Nukl. Festkörperphysik, Ges. f. Kernforschung, KFK 2481 (1977); for an abstract see this report

/4/ J.-B. Suck, J. Salgado, and W. Reichardt, in Prog. Rep. Teilinst. Nukl. Festkörperphysik, Ges. f. Kernforschung, KFK 2054, 88 (1975)

/5/ G. Ehret, this report, p. 114

5.6   How to Communicate with all NOVA Computers

G. Ehret and H. Hanak

There is an increasing need to look into those computers which are controlling experiments far away from the experimenter's usual working place. This is especially true for experiments in the reactor FR2. The run time of the experimenter from the institute into the reactor and back in order to have a short glance to this experiment is no less than 40 minutes. Another need for inter-

connecting the NOVA computers originates in security problems of the disc contence of those experiments equipped with disc units but not with tape drives. A third need comes from those computers running with a core resident BASIC version. They need a background computer for data and programs.

There are two interfaces in each NOVA computer which are always ready to operate, but which are never used. These are the control for paper tape reader and for paper tape puncher. If one connects the paper tape puncher interface of computer I with the paper tape reader interface of computer II one has one link of a computer-computer coupling. The other link of a bi-directional setup is established by connecting the remaining reader puncher interfaces. The software drives for readers and punchers are fully supported by the running operating systems i.e. SOS (Stand alone Operating System), RTOS (Real Time OS), and RDOS (Real Time Disc OS). Thus it is easy to have an efficient computer-computer coupling between two computers.

The next step is done by equipping each computer with a small additional interface which is constructed according to telephone principles: each ex-periment can dial another computer. Dialing may be done by hand or by the computer itself. The answer may be either busy or free.

Using latest LSI components like the SIGNETICS 2651 it is possible to achieve asynchronous byte frequencies of several kHz also with cable length of several kilometers. Having in mind that in an operating system environment each couple of computers only can operate in byte frequencies of less than 1 kHz it is useful to connect the computers not like a star but in a general byte-bus form. Simultaneous operations of several computer pairs is then allowed on the same cables. Up to a certain number of activities they do not interfer in time.

A general byte-bus may not only be used to interconnect reader-puncher interfaces of the NOVA computers, but also to connect a line printer as the destination of data. The same may be done with a plotter. These devices are then available for sequential public use of all computers. The NOVA software is flexible enough to feed printers or plotters via the software driver for the paper tape puncher.

An additional feature of the byte-bus is the fact that a computer console input/output may be connected and serviced. This means that all small computer may connect themselves to a bigger central NOVA computer. Thus they do all data and program manipulations on the central computer with all its resources like disc or tape equipment, or greater memory size, or higher computing power.

The status of the byte-bus at the end of the period to be reported is the following:

We have built a first setup. Reliability tests are running since several weeks. The test includes transmission over a twisted pair cable from the institute building to the reactor hall of the FR2. Severe noise is generated according to different method in neighboured twisted pair wire. Problems will arise probably by earth potential shifts during the next thunderstorm.

6. DEVELOPMENT OF MEASURING DEVICES AND TECHNIQUES

6.1 Switched Supply for Chopper Drives

N. Nücker

The time-of-flight instruments at the FR2-reactor are equipped with 1/3 hp hysteresis motors for driving choppers and rotating crystals. Up to now these motors were driven by commercial power amplifiers with 200 Watts or 500 Watts per phase depending on the maximum speed needed. Due to large phase shifts, especially when starting the motors, most of the power will be dissipated in the powertransistors. Flexibility in speed wanted by the experimentalists requires adaptation of the output voltage which may be achieved by large transformators.

In our new concept (Fig.) -we use a switched power supply allowing to adjust the output voltage from 0 V to 90 V with currents up to 7 A. Since the motor coils need not be decoupled from the main line, only small transformers for the voltage and switching control circuits are needed. The motor coils are switched to the output of this powersupply by Darlington transistors with integrated reverse diodes. This technique reduced the heating of the powertransistors to a minimum independent of the current to voltage phase shift.
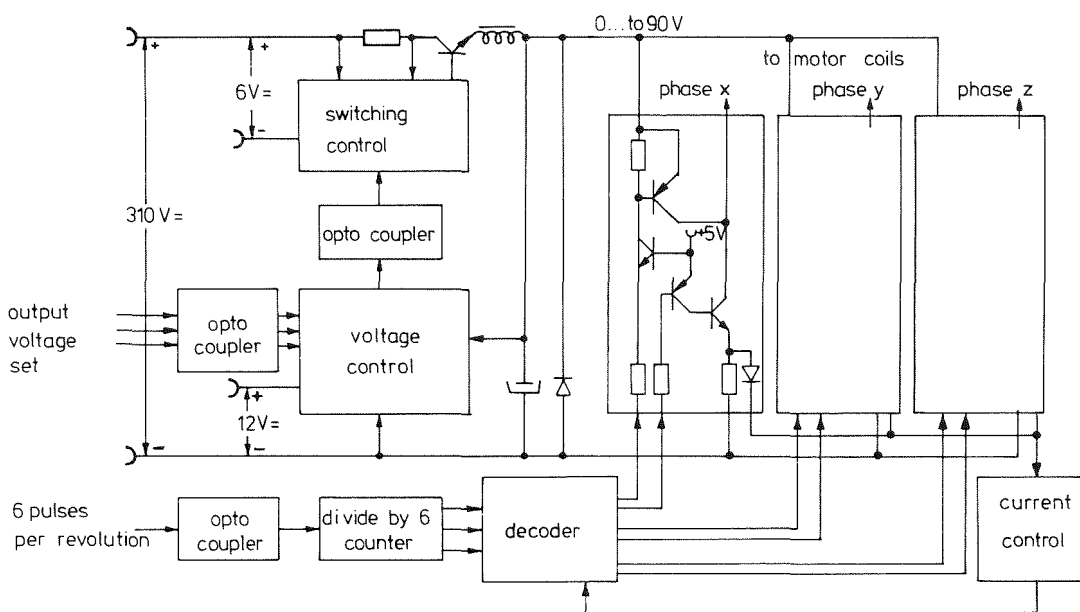
Fig. Switched supply

The digital signals for the speed of the motor and the output voltage are transmitted by optocouplers allowing for decoupled interfaces and computer control.

The small size of the new equipment allows the implementation of two of these in one costume 14 inch frame together with a frequency and phasing control /1/. A considerable reduction in the size, weight, and price is achieved with this new equipment.

Reference

/1/ N. Nücker, in Prog. Rep. Teilinst. Nukl. Festkörperphysik, Ges. f. Kernforschung, KFK 2054, 92 (1974)

6.2   Verwendung von Al-Waben als Abstandshalter für Sollerkollimatoren

(Use of Al-Honeycombs as Spacer-Grids for Soller-Collimators)

K. Weber

Bei der Herstellung von Sollerkollimatoren ist es notwendig, daß die Absorberbleche glatt, parallel und in einem der Divergenz entsprechenden Abstand angeordnet sind. Diese Forderungen wurden bisher nur mit einigem technischem Aufwand (horiz. oder vertikale Verspannung der Bleche) realisiert. Ferner benötigte man als tragendes Element und zur Aufnahme von Blechen und Abstandshalter ein Gehäuse.

Eine Vereinfachung der Kollimatoranfertigung bringt die Verwendung von Al-Waben als Abstandshalter. Sie werden in den Raum zwischen den Absorberblechen (z.B. cadmiertes Nickelblech) gelegt. Der geringe Materialanteil von ca. 1.5 % verursacht nur wenig Intensitätsverlust.

Bei dem Wabenmaterial* handelt es sich um 0.05 mm starkes Al-Blech, das in hexagonaler Geometrie (Bienenwaben) zu Platten zusammengeklebt ist. Es ist in Bild 1 dargestellt.

---

* Dieses Material wurde uns freundlicherweise von der Fa. Messerschmitt-Bölkow-Blohm, München, zur Verfügung gestellt.
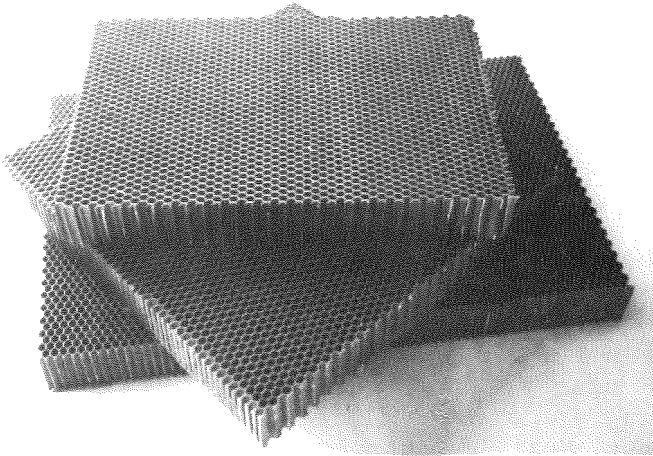
Bild 1

Wabenmaterial aus
Al-Blech

Die Herstellung der Wabenabstandshalter geschieht in folgender Weise:

1. Ausschneiden von ca. 100 x 100 mm großen Stücken,

2. Stauchen auf Materialstärke quer zur Wabenachse,

3. Spannen zwischen zwei ca. 5 mm starke Al-Platten und Sägen auf
   die gewünschte Breite,

4. Auseinanderziehen auf ihre ursprüngliche Form.

Werden die Waben mit den Absorberblechen verklebt (nur dünne Klebeschicht wegen Streuung am Wasserstoff), so lassen sich Kollimatoren ohne Gehäuse (Bild 2) z.B. für Multidetektorspektrometer herstellen. Bei Kollimatoren mit Gehäuse können die Wabenabstandshalter lose zwischen die Absorberbleche gelegt werden, wenn sie anschließend durch Verschrauben oder durch Druckplatten festgehalten werden. Eine gute Anwendungsmöglichkeit finden die Al-Waben auch als Kollimatoreinsatz bei Fermi-Choppern. Große Festigkeit bei geringem Materialaufwand ergeben Kollimatoreinsätze für hohe Drehzahlen bei guter Neutronendurchlässigkeit.
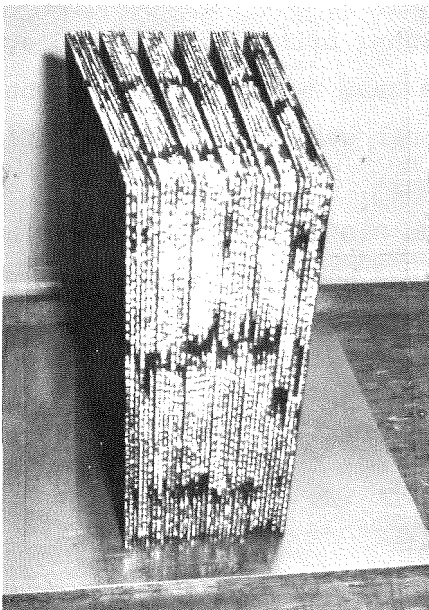
Bild 2

Anordnung von sechs
Kollimatoren ohne Ge-
häuse mit Al-Waben als
Abstandshalter

Bei Verwendung von dünnen Absorberblechen sollten die Al-Waben in einen Al-Rahmen eingesetzt werden (Bild 3), da sich durch das Zuschneiden keine geschlossene Kante ergibt.
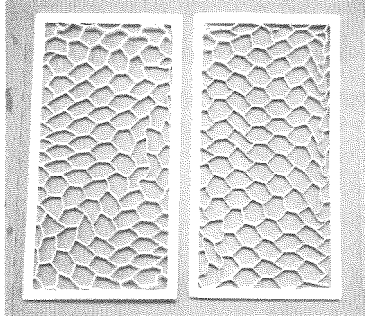
Bild 3

Al-Waben mit Rahmen

6.3 Entwicklung und Anwendung von Sollerkollimatoren variabler Divergenz

(Development and Application of Soller-Collimators with Variable Divergency)

K. Weber

Im Rahmen der Geräteverbesserung wurden für die primäre Kollimation des Neutronenstrahls zwei Versionen von Sollerkollimatoren entwickelt, die es je nach Problemstellung erlauben, ihre Divergenz zu verändern. Damit erhält man die Möglichkeit, Neutronenintensität und Auflösung dem jeweiligen Problem anzupassen.

Bild 1 zeigt eine der beiden Versionen. Drei Sollerkollimatoren herkömmlicher Bauart mit den Divergenzen 40', 30' und 20' sind auf einem Schiebetisch befestigt und können so, je nach gewünschter Kollimation, in den primären Neutronenstrahl gebracht werden. Ferner kann der Kollimator ganz aus dem Strahl gefahren werden, um die größtmöglichste Intensität zu erhalten. Dieses Gerät ist im Primärteil von TAS1 eingebaut.
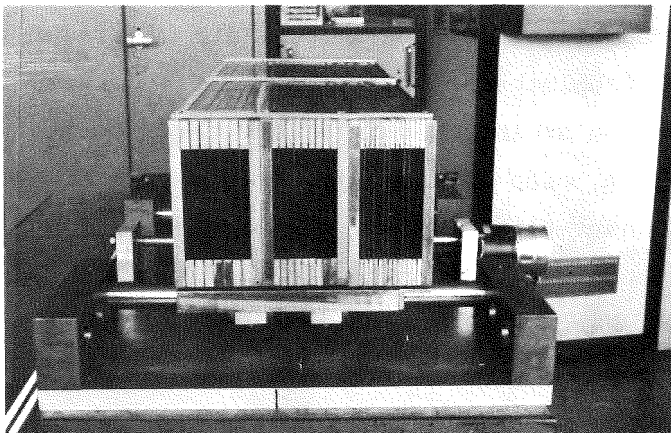
Bild 1

Drei Kollimatoren unterschiedlicher Divergenz

Bild 2 zeigt die zweite Version. Dieser Sollerkollimator besitzt ebenfalls Bleche mit konstantem Abstand und konstanter Länge, der Unterschied zum herkömmlichen Sollerkollimator besteht jedoch darin, daß er ohne Boden und Deckel aufgebaut werden kann. Dies ist möglich durch die Verwendung neuartiger Abstandshalter (Al-Waben), die in den Raum zwischen den Abschirmblechen gelegt werden. Der kleine Materialanteil dieser Al-Waben (1.5 %) verursacht nur einen geringen Intensitätsverlust.
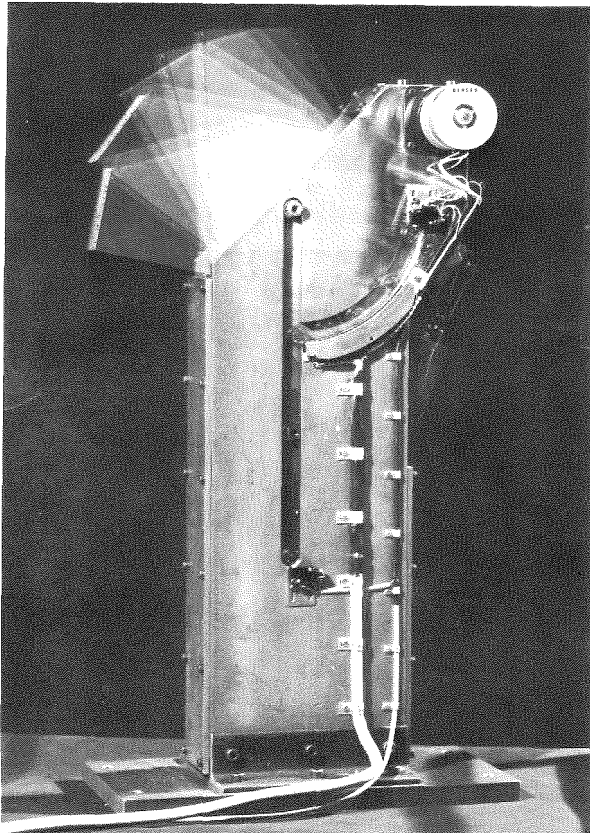
Bild 2

Kollimator mit stufenlos variabler Divergenz

Ein so aufgebauter Kollimator kann im Neutronenstrahl gedreht werden, ohne daß Strukturmaterial den Strahl beeinflußt. Dieses Drehen von der vertikalen in die horizontale Lage bewirkt bei einem Kollimator mit Rechteckformat eine kontinuierliche Veränderung der zur Kollimation beitragenden Blechlängen, was bei einem gleichbleibendem Blechabstand eine stufenlos variable Änderung der Kollimation ergibt. Der in Bild 2 dargestellte Kollimator hat eine Länge von 360 mm, eine Höhe von 160 mm und eine Breite, entsprechend dem primären Neutronenstrahl von 40 mm. Der Blechabstand beträgt 1.5 mm. Die sich daraus ergebende Divergenz kann somit zwischen 32' und 18' stufenlos variiert werden. Ferner erlaubt der Hub-Drehmechanismus ein Absenken des Kollimators aus dem Neutronenstrahl, sowie ein Verschließen des Strahls durch Anbringen einer Abschirmplatte. Die Positionsanzeige erfolgt optisch über elektrische Kontakte.

6.4 Operation of the 3MV van de Graaff-Accelerator

A. Ernst, D. Roller, H. Schreiber, and J. Nadasdy

From April 1977 to March 1978 the accelerator was in operation for 5747 hours. 5058.5 hours were used by the experimentors for the different experimental programs, consisting mainly of

2003.5 hours neutron cross section measurements for the fast breeder program

1197 hours for surface layer analysis techniques like Rutherford backscattering, channelling, proton induced X-rays and specific nuclear reactions

1145.5 hours neutron cross section measurements for astrophysics

680.5 hours experiments concerning the physics of nuclear fission

32 hours ion implantation and production of radiation damage for the fusion reactor program.

During the reported time period, the first experiment using heavy ion beams was performed at the 3OR beamline and a second experiment using heavy ions has been set up. Performance of the accelerator and of the new heavy ion analysing system /1/ - intensity, stability, mass separation - have fulfilled and exceeded all our expectations.

In early summer 1977 during only a few weeks the beamline for pulsed and bunched light ion beams - used for neutron production - was replaced by a beamline system with a new switching magnet, feeding up to five different beamlines and target areas /2/. Now several neutron experiments can be operative and can be prepared at the same time, thereby greatly improving accelerator utilisation. One beamline is used for the proton microbeam /3/, leaving four for neutron production.

Near the end of 1977, the accelerator was upgraded to a maximum terminal voltage of 3.75 MV. - During all the reported period, the work was continued to get closer supervision and control of the accelerator by the associated process computer /4/, /5/.

References

/1/ A. Ernst, this report,following contribution

/2/ A. Ernst, in Annual Report, Teilinst. Kernphysik, Ges. f. Kernforschung,
    KfK 2686 , contribution 7.2.3 (1978)

/3/ D. Heck, in Annual Report, Teilinst. Kernphysik, Ges. f. Kernforschung,
    KfK 2686 , contribution 7.2.4 (1978)

/4/ A. Ernst, this report

/5/ A. Ernst, in Annual Report, Teilinst. Kernphysik, Ges. f. Kernforschung,
    KFK 2379 , contribution 6.2.2 (1976)

6.5   Facilities for Experiments Using MeV Heavy Ion Beams

   A. Ernst

       To enable experiments with heavy ion beams at our 3.75 MV van de Graaff-
accelerator, a new beamline system had to be set up.
       Our old analysing magnet is capable of deflecting a beam with a mass
- energy - product of 12 (a.m.u. • MeV) by 25 degrees. The design for the
heavy ion analysing magnet was a mass - energy - product of 600, while,
as a compromise, a deflecting angle of 15 degrees was regarded as sufficient.
45 degrees was chosen as maximum deflecting angle with reduced mass - energy -
product (table). The new analysing magnet defined by these parameters had to
have a larger bending radius than the old one, so from ionoptical considera-
tions (our old magnet feeds a Mobley bunching system), we could not simply
replace the old magnet, but we had to install the new magnet in addition to
the old one. Due to the large focal distances of the double focusing dipole
magnet, quadrupole focusing was required in addition. For economy reasons,
an upstream position was selected for the quadrupole doublet, which is also
capable of focusing a mass - energy product 600 beam to a distance of 3 meters.
Because of geometrical restrictions, the heavy ion beamlines have to cross
the light ion beamline from the bunching magnet. Three beamlines from the
heavy ion analysing magnet have been put into operation until now (30 L, 15 R,
30 R). Beam quality has surpassed our expectations in every respect. Mass
resolution using Kr^+-ions through the 30 degree port without any object slits

can be seen from figure 2.

Table   Ionoptical parameters of the dipole magnet

Port	Mass-Energy-Product	Bending radius (cm)	Focal distance (cm)
± 15°	600	272	4060
± 30°	200	137	960
± 45°	90	92.5	390
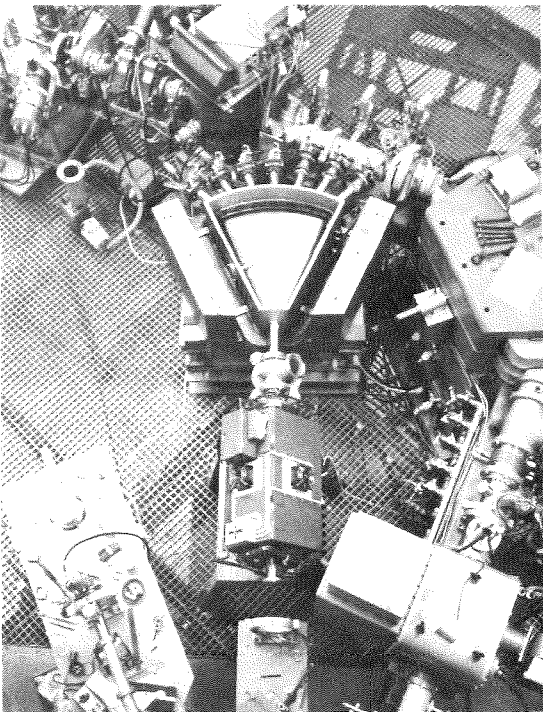
Fig. 1   Analysing system during assembly
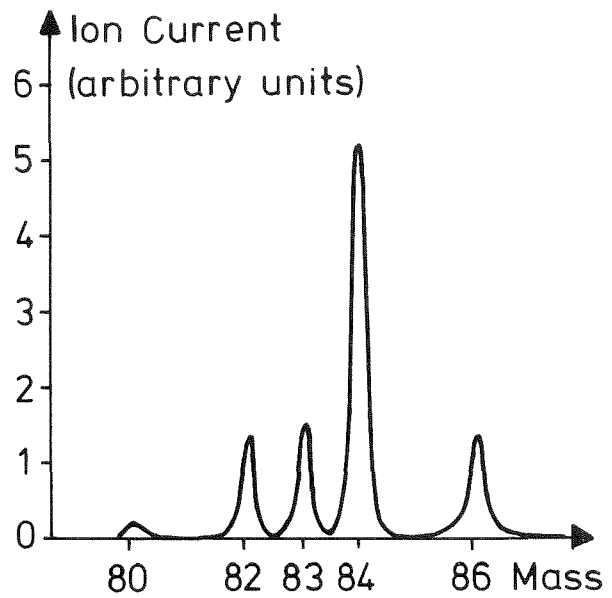
Fig. 2   Analysed Kr^+-beam on a beam profile monitor

6.6   Status Display of the van de Graaff Beam Guidance System on a Colour TV Monitor

A. Ernst

The large extensions to the beamline system of our accelerator done in the past few years /1, 2, 3/ made it desirable to provide the operator with

a schematic diagram of the beamline system with a built-in indication of the status of its components, that can be quickly overlooked. Since the configuration of the beamlines is expected to undergo changes also in the future, and since the instrumentation of the existing beamlines is quite frequently changed, it was decided not to set up a hard wired supervisory panel, but to display a software generated schematic diagram with status indication on a colour monitor instead, thus making changes very easy.

Status signals like beam stopper in or out, valves open or closed, vacuum good or bad,etc., are fed into the computer via CAMAC interrupt registers. The schematic diagram of the beamline system (figure) is stored in the image memory of a CAMAC programmable colour video display driver. The display consists of 64 x 32 characters. The character set consists of the standard ASCII set and up to 256 software defined symbols programmable in a 8 x 9 point matrix. One beamline component is displayed as one user-defined symbol. When the status of a beamline component changes, the computer gets an interrupt and processes the interrupt for example by reading the image memory at the location representing the component, changing the bits defining the foreground colour, and writing the information back.(Green=o.k., beam can pass. Red = beam is affected by status of beamline component.) The background colour of the beamlines gives information on vacuum status and usage of the beamline.(Dark blue=good vacuum, no beam. Light blue=good vacuum, beamline used for beam transport. Black=bad vacuum, no beam. Yellow=bad vacuum in active beamline.)

On this display, the operator can see with one glance where the beam is travelling and where the beam is eventually stopped, and if so, for what reasons. Furthermore, malfunctioning components can be displayed flashing, i.e. the symbol colour is automatically alternated between foreground and background colour about once a second.
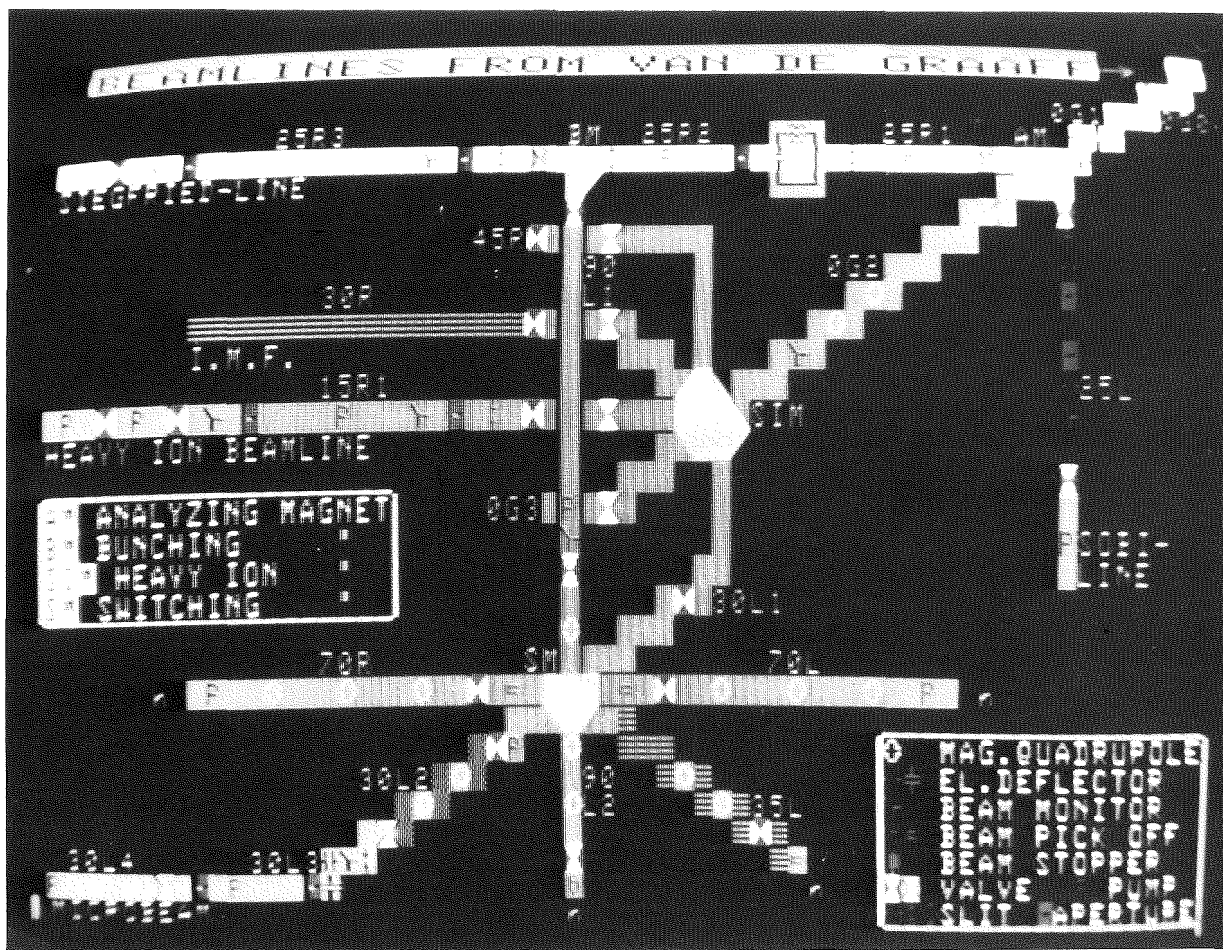
Fig. 1   Beamline status as displayed on colour TV monitor

References:

/1/ A. Ernst, this report, preceding contribution

/2/ A. Ernst, in Annual Report, Teilinst. Kernphysik, Ges. f. Kernforschung, KfK 2686, contribution 7.2.3 (1978)

/3/ D. Heck, in Annual Report, Teilinst. Kernphysik, Ges. f. Kernforschung, KfK 2686, contribution 7.2.4 (1978)

6.7   Automated Sample Changing and Data Acquisition System for Ion Beam
      Material Analysis

M. Conrad, F. Ratzel, H. Hanak, and E.L. Haase

A computer-based data acquisition and sample changing system has been
set up and is now in operation for routine measurements of Rutherford back-
scattering and nuclear reaction spectra at the Van-de-Graaff accelerator.

In brief, the system has the following functions:

i)   To perform all normal functions of a computer-based multichannel
        analyzer including more complex handling of spectra.

ii)   To position the sample holder - nine discrete faces and 23 mm in
        height continuously - for consecutive measurements. This permits
        both scan measurements along samples or the mounting of up to
        five samples per face.

iii)   To permit measurements of up to five samples tilded with respect
        to the beam to increase depth resolution.

iv)   To control by a master program the sequential measurements, storing
        spectra on the disk, plotting them automatically and monitoring the
        status of the measuring system.

I.   The Automatic Sample Changer

     The measurements are carried out under HV or UHV conditions. Therefore
the sample holder shown in Fig. 1 is constructed accordingly, i.e. equipped
with UHV feed-throughs, and conflat gaskets. The sample holder is mounted on
a wheeler stainless steel flange with a diameter of 14". The samples are fixed
to an extended spindle which is bolted to a linear/rotary drive feed through.
The sample holder consists of a nine-sided aluminium prism. To guarantee a
centring rotary motion with a maximum deviation of ± 0.1 mm/rotation, the
spindle is supported by an UHV-bearing in the lower part of the wheeler flange
on the vacuum side.

     There are two special gears, which drive without creast clearance the
respective wheels of the UHV feed-through by stepping motors. On the upper
part of the UHV-feed-through there is a disk fixed whose binary coded holes
determine by slits the nine individual positions of the sample holder.

Vertical Position Measuring Unit

Position Coding Disk

Linear/Rotary Drive UHV Feedthrough

Lifting Magnet for Height Measuring Unit

Wheeler Flange

Sample Head

Step Motor (Position)

Step Motor (Height)
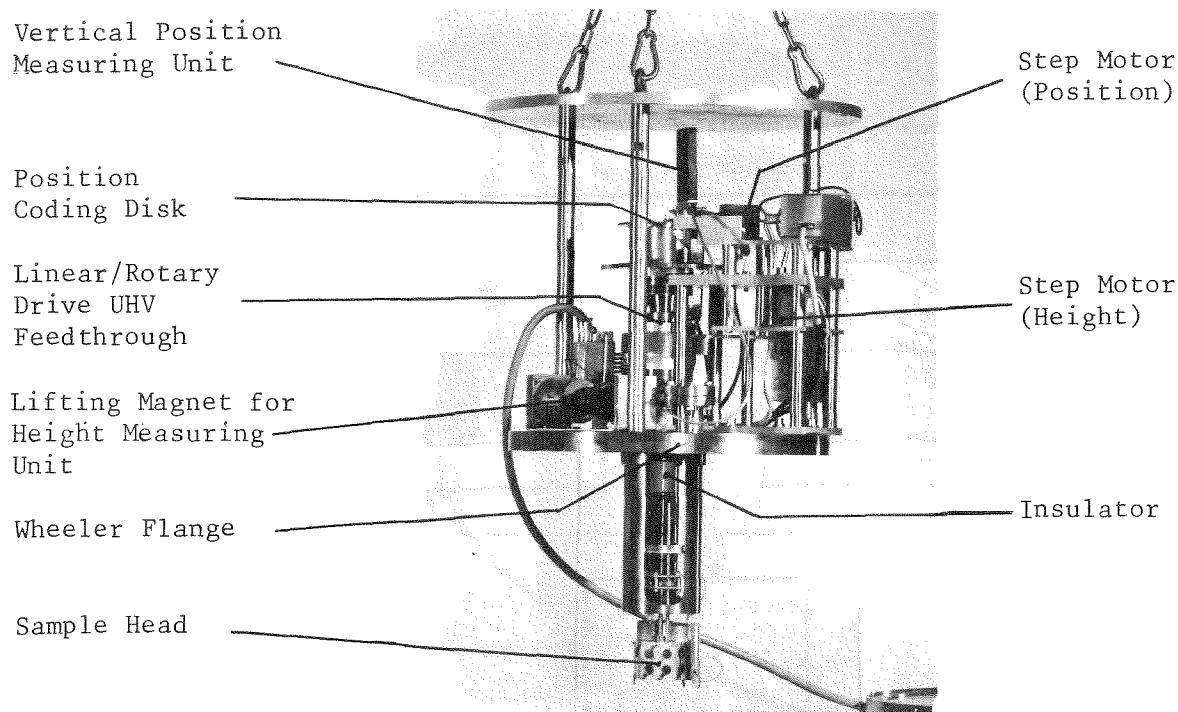
Insulator

Fig. 1   Automatic Sample Changer

The height is adjusted and controlled by a height measuring unit served by a program controlled lifting magnet.The count of this height measuring unit is given to a scaler. An insulated shielding cup is attached around the sample holder for the secondary electron suppression.

II. The Hardware Configuration

Computer control is performed with a NOVA2 minicomputer with 64 kByte memory. Furthermore there is a 32 kByte memory for sequentially accessed data. This external memory can be loaded via DMA. There are also four programmeable interrupt sources to be used in the system. A 10 MByte disk offers adequate storage capacity. A block diagram of the hardware configuration is given in Fig. 2. As soft-ware we used the program system LOLA described elsewhere /1/.

As input/output terminals a Silent 700 ASR, a TV and a Calcomp Plotter 565 are available. Detector signals were handled by the standard electronics described elsewhere /2/. The ADC output is given via DMA to the external memory. Sample positioning and charge counting is done by CAMAC modules. Two BORER step motor drivers control the step motor activity. Positions read are indicated by a CAMAC interrupt register and a CAMAC pattern unit. Counting
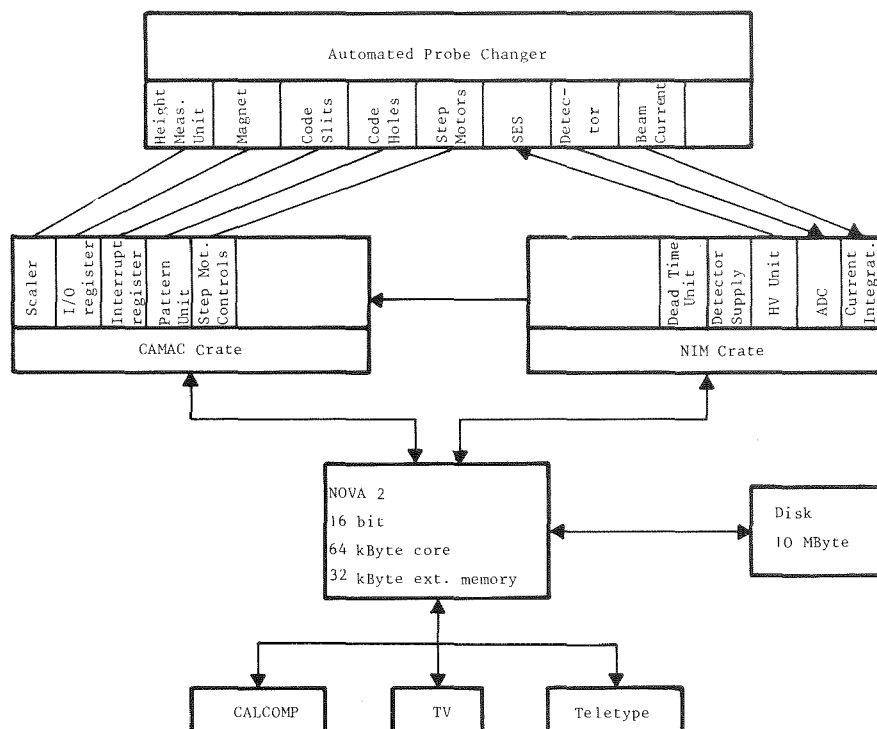
Fig. 2   Schematic system configuration. Abbreviations used: SES: secondary
electron suppression, HV unit: High voltage supply (300 V). The
function of the modules is given in the text.

is done by an scaler. A LAM signal for interrupt handling is produced on
overflow of the scaler. The CAMAC modules all together allow controlled
handling and supervision of all the positioning and measuring processes.

This system has been in operation now for about two months showing
good reliability and accuracy.

References

/1/ M. Conrad, this report, following contribution

/2/ K.-G. Langguth, Ges. f. Kernforschung, KFK 2476 (1977)

6.8   LOLA, a Program System for Measuring and Handling of 1/2 K Spectra

M. Conrad

A new on-line data processing system has been developed for measuring
nuclear reaction and backscattering spectra at the van-de-Graaff accelerator
of the institute. Replacing the old system based on a Nuclear Data analyser a
new data aquisition and spectra evaluation system basing on a NOVA 2 mini-
computer has been installed. Details of the hardware specifications are given
in the preceding report /1/.

Restrictions for program development were given by the limited BASIC
memory size of about 18 K Byte. This requires an elaborated overlay technique.
This is accomplished with only the controlling routines being core resident,
while all the handling both of spectra and hardware is done in overlay programs.

LOLA offers various possibilities for user interaction with the program.
Dialogue can be done either by means of a teletype or by TV combined with a
lightpen interrupt. Interrupts used as program switches can be set either by
CAMAC, lightpen or switchboard.

Although it is necessary to control the program from two stations, there
is only one single teletype available in the system. Therefore much of the
dialogue must be performed via TV and lightpen or interrupt.

At the present status of LOLA the following routines are available:

I.   Live-display of spectra together with full information of measurement
      conditions on TV. Both counts full scale and width of the spectrum-
      display can be changed by interrupts. Four groups containing 512 channels
      can be addressed in the memory.

II.   Marker manipulation is accomplished with two independent markers, showing
      either channel number and counts or channel number and corresponding mass.

III. Sample positioning can be done on nine discrete faces of the sample holder
      and by one millimeter steps in a 20 mm height range.

IV.   Routines for starting a measurement under control of preset charge. It
      is also possible to perform fully automatized a sequence of measurements.

V.   Routines for storing spectra from memory to disk or from disk to memory.
      There is also the possibility to transfer spectra from one to another group
      in the memory.

VI.   Plotting the spectra via a calcomp plotter.

VII. Special routines for handling spectra.

LOLA and it's options are presently successfully employed in routine measurements at the van-de-Graaff accelerator.

Reference

/1/ M. Conrad, F. Ratzel, H. Hanak, and E.L. Haase, this report, preceding
    contribution

Heger, G.
Über die strukturellen Phasenübergänge von perowskitähnlichen Schichten-
strukturen vom Typ $(C_nH_{2n+1}NH_3)_2MeCl_4$
Habilitationsschrift, Philipps-Üniversität Marburg 1977
KFK 2574 (1978)

Hofmann-Kraeft, B.
Messung des partiellen Isotopeneffekts an Vanadiumnitrid
Dissertation, Universität Karlsruhe 1977
KFK 2524 (1977)

Junod, A.; Muller, J.; Rietschel, H.; Schneider, E.
Chaleur specifique et transformation martensitique dans le systeme
$Nb_{1-x}Sn_x$
Journal of Physics and Chemistry of Solids 39, 317 (1978)

Käfer, K.
Phononendispersion und Streugesetz $S(\underline{k}, \omega)$ für ein quasi-eindimensionales
Peierls-System
Dissertation, Universität Karlsruhe 1977
KfK 2630 (1978)

Kaufmann, R.
Monte-Carlo-Rechnungen zur Simulation von Channelling-Experimenten an
V_3Si-Einkristallen
Diplomarbeit, Universität Karlsruhe 1978
KfK 2638 (1978)

Kress, W.; Reichardt, W.; Wagner, V.; Kugel, G.; Hennion, B.
Lattice dynamics of transition metal oxides
Proceedings of the Internat. Conference on Lattice Dynamics, Paris, 77 (1977)

Langguth, K.-G.
Herstellung von supraleitendem Vanadiumkarbid durch Ionenimplantation
Dissertation, Universität Karlsruhe 1977
KFK 2476 (1977)

Lehner, N.; Geick, R.; Heger, G.
On the mechanism of the order-disorder phase transition in the peroviskite-
type layer structures $(C_nH_{2n+1}NH_3)_2MnCl_4$
Proceedings of the Internat. Conference on Lattice Dynamics, Paris, 717 (1977)

Linker G.
Influence of ion bombardement on the superconducting transition temperature
of evaporated vanadium layers
Journal of Nuclear Materials $\underline{72}$, 275 (1978)

Linker, G.
Channeling analysis of radiation disorder in ion implanted vanadium and
molybdenum single crystals
Nuclear Instruments & Methods $\underline{149}$, 365 (1978)

Lombaard, J.M.; Meyer, O.
Channeling studies in carbon implanted NbC-single crystals
Radiation Effects $\underline{36}$, 83 (1978)

Lombaard, J.M.; Meyer, O.
Depth profiling of oxygen in oxidized ceramic Si_3N_4 with the back-
scattering technique
Nucl. Instr. Meth. $\underline{145}$, 347 (1977)

Meyer, O.
Radiation damage and superconductivity in V_3Si single crystals
Journal of Nuclear Materials $\underline{72}$, 182 (1978)

Meyer, O.
Channeling effect studies in V_3Si single crystals
Nuclear Instrument & Methods $\underline{149}$, 377 (1978)

Meyer, O.; Linker, G.; Lombaard, J.M.; Seeber, B.
Application of ion beams for modification and analysis of super-
conducting materials with bcc, Na11 and A15 structure
KfK $\underline{2659}$ (1978)

Müller, W.H.G.; Baumann, F.; Dammer, G.; Pintschovius, L.
Superconductivity in polymeric sulfur nitride $(SN)_x$ at high pressure
Solid State Communications $\underline{25}$, 119 (1978)

Nücker, N.
Phonon density of states of lanthanum in the dhcp and fcc phase
Proceedings of the Internat. Conference on Lattice Dynamics, Paris, 244 (1977)

Nücker, N.; Knorr, K.; Jex, H.
The phonon frequency distribution of KCN
Journal of Physics C: Solid State Physics 11, 1 (1978)

Pintschovius, L.; Currat, R.; Wendel, H.
Acoustic phonons of polysulfur nitride $(SN)_x$
Proceedings of the Internat. Conference on Lattice Dynamics, Paris, 579 (1977)

Pintschovius, L.; Reichardt, W.; Scheerer, B.
Lattice dynamics of TiC
Journal of Physics C: Solid State Physics 11, 1557 (1978)

Rietschel, H.
Mechanismen der Supraleitung bei hoher Übergangstemperatur
Physikalische Blätter 12, 627 (1977)

Roedhammer,P.; Reichardt, W.; Holtzberg, F.
Soft-mode behaviour in the phonon dispersion of YS
Physical Review Letters 40, 465 (1978)

Roedhammer, P.; Reichardt, W.; Weber, W.; Holtzberg, F.
Phonon anomalies in yttrium sulfide
Proceedings of the Internat. Confernce on Lattice Dynamics, Paris, 84 (1977)

Ruebenbauer, K.; Fink, J.; Schmidt, H.; Czjzek, G.; Tomala, K.
An investigation of magnetic ordering in $Gd_xCe_{1-x}Ru_2$ by ^{155}Gd Moessbauer spectroscopy
Physica status solidi (b) 84, 611 (1977)

Schelten, J.; Schmatz, W.
Neutron small angle and diffuse scattering towards applied research
IAEA-204: Neutron Scattering in Applied Research, Vienna (1977)

Schmatz, W.
Disordered structures
in H. Dachs (Ed.), Topics in Current Physics, Vol. 6, 151 (1978)

Schmatz, W.
Großforschungsgeräte in der Festkörperphysik
KfK Nachrichten 10/2, 6 (1978)

Schommers, W.
Correlations in the motion of particles in α-AgI: a molecular dynamics study
Physical Review Letters 38, 1536 (1977)

Schommers, W.
Current-current correlations in α-AgI
Physical Review B: Solid State 17, 2057 (1978)

Schommers, W.
Liquid argon: the influence of three-body interactions on atomic correlations
Physical Review A 16, 327 (1977)

Seitz, E.; Schmatz, W.; Bauer, G.S.; Just, W.
A trigonal distortion field for substitutionally dissolved Bi atoms in Pb
phys. stat. sol. (a) 46, 557 (1978)

Tomala, K.; Czjzek, G.; Fink, J.; Schmidt, H.
Hyperfine interactions in intermetallic compounds between Gd and 3d transition metals
Solid State Communications 24, 857 (1977)

Vetter, J.E.; (Hrsg.); Bauer, W.; Böhme, G.; Borgstedt, U.; Citron, A.; Ehrlich, K.; Eyrich, W.; Grimm, L.; Kaletta, D.; Käppeler, F.; Kapula, H.; Küchle, M.; Mittag, K.; Moritz, J.; Müller, A.; Peppler, W.; Piosczyk, B.; Reichardt, W.; Rusch, D.; Schatz, G.; Schmidt, F.K.; Schneider, J.; Vetter, J.E.; Vogg, H.; Zieher, K.W.;
Vorstudie für eine intensive Neutronenquelle
KFK 2542 (1977)

Ziemann, P.
Änderung der supraleitenden Eigenschaften von Aluminium durch Selbst-ionenbeschuss bei tiefen Temperaturen
Dissertation, Universität Karlsruhe 1977
KFK 2562 (1977)

7.2   CONFERENCE CONTRIBUTIONS AND SEMINARS

Blanckenhagen, von P.; Happel, H.; Knorr, K.
Kristallfelder in $(La,Er)Al_2$ und $(Y,Er)Al_2$
Verhandl. DPG (VI) <u>13</u>, 191 (1978)

Czjzek, G.; Fink, J.; Schmidt, H.; Tomala, K.
Hyperfine interactions in intermetallic compounds of Gd with 3d
transition metals
Internat. Conference on Moessbauer Spectroscopy, Bucharest, Romania,
September 5 − 10 (1977)

Fink, J.; Czjzek, G.; Schmidt, H.; Tomala, K.; Obenshain, F.E.
Local susceptibilities in Pd-Ni alloys by ^{61}Ni-Moessbauer spectroscopy
Internat. Conference on Physics of Transition Metals, Toronto,
August 15 − 19 (1977)

Gauss, Chr.
Metastabile, kristalline Phasen in Pb-Bi Legierungen
Verhandl. DPG (VI) <u>13</u>, 316 (1978)

Geibel, Chr.
Untersuchung der partiellen Debye-Waller-Faktoren von Nb_3Sn
Verhandl. DPG (VI) <u>13</u>, 340 (1978)

Gompf, F.
Vergleich der Phononenzustandsdichten von trigonalem und glasigem Selen
Verhandl. DPG (VI) <u>13</u>, 11o (1978)

Gompf, F.
Comparison of the phonon densities of states of trigonal, vitreous, and
red amorphous selenium
7. Europhysics Conf. on Macromolecular Physics: Structure and Dynamics of
Polymers − Neutron Scattering Experiments and New Theoretical Approaches,
Strasbourg, France, May 23 − 26 (1978)

Guth, H.; Heger, G.
Strukturbestimmung von ß-Eukryptit mit Hilfe von Neutronenbeugung
Verhandl. DPG (VI) <u>13</u>, 168 (1978)

Haase, E.L.
Untersuchungen an der $Nb_3Ge_{1-x}Si_x$ Mischphase.
Verhandl. DPG (VI) <u>13</u>, 340 (1978)

Heger, G.
Strukturuntersuchungen in der orthorhombischen Phase von KCN unter
uniaxialem Druck
Inst. f. Kernphysik, Universität Frankfurt, April 27 (1978)

Käfer, K.
Einfluß der Interkettenkorrelation der Überstrukturphasen eines 1-d-
Peierlssystem auf die $2k_F$-Phononenanomalie
Verhandl. DPG (VI) <u>13</u>, 329 (1978)

Kaufmann, R.; Meyer, O.
Analyse von Strahlenschäden in V_3Si-Einkristallen mit Hilfe der Channelling-
Methode
Verhandl. DPG (VI) <u>13</u>, 339 (1978)

Lehner, N.; Geick, R.; Heger, G.; Wagner, V.; Renker, B.
Unelastische Neutronenstreuexperimente an $(CD_3ND_3)_2MnCl_4$
Verhandl. DPG (VI) <u>13</u>, 110 (1978)

Linker, G.
Channeling analysis of radiation disorder in ion implanted vanadium and
molybdenum single crystals
3. Internat. Conference on Ion Beam Analysis, Washington, D.C., June 27 -
July 1 (1977)

Linker, G.; Meyer, O.
Influence of ion bombardment on the superconducting transition temperature
of evaporated transition metal layers
Internat. Discussion Meeting on Radiation Effects in Superconductivity,
Argonne, ILL., June 13 - 16 (1977)

Mereiter, K.; Preisinger, A.; Guth, H.
Hydrogen bonds in Schlippe's salt: refinements of the crystals structures
of $Na_3SbS_4 \cdot 9H_2O$ by X-ray diffraction and $Nb_3SbS_4 \cdot 9D2O$ by neutron
diffraction
4. European Crystallographic Meeting, Oxford, UK, August 30 - September 3
(1977)

Meyer, O.
Channeling effect studies in V_3Si single crystals
3. Internat. Conference on Ion Beam Analysis, Washington, D.C.;
June 27 - July 1 (1977)

Meyer, O.; Lombaard, J.M.
Channeling studies in carbon implanted NbC and VC single crystals
Internat. Discussion Meeting on Radiation Effects in Superconductivity,
Argonne, Ill., June 13 - 16 (1977)

Meyer, O.
Radiation damage and superconductivity in V_3Si single crystals
Internat. Discussion Meeting on Radiation Effects in Superconductivity,
Argonne, Ill., June 13 - 16 (1977)

Nücker, N.; Daubert, J.; Jex, H.; Knorr, K.; Müllner, M.; Suck, J.-B.
Phononenzustandsdichte von KCN und NaCN
Inst. f. Kernphysik, Universität Frankfurt, April 27 (1978)

Pintschovius, L.
Polyschwefelnitrid, das erste Beispiel eines polymeren Metalls
Herbsttagung DPG, Karlsruhe, September 1978

Pintschovius, L.; Wendel, H.; Currat, R.
Acoustic phonons in polymeric sulfur nitride, $(SN)_x$
7. Europhysics Conference on Macromolecular Physics: Structure and Dynamics
of Polymers - Neutron Scattering Experiments and New Theoretical Approaches,
Strasbourg, France, May 23 - 26 (1978)

Renker, B.; Butt, N.M.
Untersuchungen optischer Phononen im Mischkristall $K_{.5}Rb_{.5}J$
Verhandl. DPG (VI) <u>13</u>, 110 (1978)

Rietschel, H.
Mechanismen der Supraleitung bei hoher Übergangstemperatur
Verhandl. DPG (VI) <u>13</u>, 1087 (1978)

Roedhammer, P.; Pintschovius, L.; Reichardt, W.; Gompf, F.; Christensen, A.N.
Gitterdynamik von Vanadiumnitrid
Verhandl. DPG (VI) <u>13</u>, 315 (1978)

Roedhammer, P.; Reichardt, W.; Holtzberg, F.
Phononenanomalien in den Phononendispersionen von YS und LaS
Verhandl. DPG (VI) <u>13</u>, 315 (1978)

Schmatz, W.
Großforschungsgeräte in der Festkörperphysik
Antrittsvorlesung, Universität Karlsruhe, August 1977

Schommers, W.
Modell zur Beschreibung von Orts- und Zeitkorrelationen in α-AgI
Hauptvortrag auf dem Festkörpertag der Universitäten Göttingen/Clausthal am
24. Juni 1977

Schweiss, B.P.; Renker, B.; Suck, J.B.; Flükiger, R.
Untersuchungen zur Gitterdynamik von Molybdänchalkogeniden
Verhandl. DPG (VI) <u>13</u>, 343 (1978)

Ziemann, P.; Heim, G.; Buckel, W.
Änderung der supraleitenden Eigenschaften von Aluminiumfilmen durch Selbst-
ionenbestrahlung geringer Fluenzen bei tiefen Temperaturen
Verhandl. DPG (VI) <u>13</u>, 309 (1978)

8. LIST OF THE NEUTRON SPECTROMETERS AT THE FR2 AT KARLSRUHE OPERATED BY THE IAK I

DIF 1 : Four circle diffractometer, $\lambda = 1.024$ Å

DIF 2 : Two circle diffractometer, 0.7 Å $\leq \lambda < 2.6$ Å

DIF 3 : Two circle diffractometer, $\lambda = 1.28$ Å or 1.09 Å

DIF 4 : Four circle diffractometer, $\lambda = 0.922$ Å or 2.41 Å

DIF 5 : Four circle diffractometer, $\lambda = 0.89$ Å or 1.26 Å

TAS 1 : Three-axis spectrometer, 13 meV $\leq E_o < 120$ meV

TAS 2 : Three-axis spectrometer, 8 meV $\leq E_o < 64$ meV

TOF 1 : Time-of-flight spectrometer with Fermi-chopper, 140 detectors, thermal neutrons

TOF 2 : Time-of-flight spectrometer with rotating crystal, 60 detectors, cold neutrons

TOF 3 : Time-of-flight spectrometer with Fermi-chopper, 120 detectors, thermal neutrons

TOF 4 : Time-of-flight spectrometer with rotating crystal, 6 detectors, cold neutrons

MAG 1 : Spectrometer for diffuse scattering, 40 detectors, thermal neutrons

MAG 2 : Multipurpose spectrometer, 40 detectors, cold neutrons.

9. STAFF MEMBERS (June 1, 1978)

Head of Institute: W. Schmatz

Professional Staff

Blanckenhagen, P.v.	*Heger, G.*	*Nücker, N.*	*Schommers, W.*
Czjzek, G.	*Jung, V.*	*Pintschovius, L.*	*Schweiß, P.*
Fink, J.	*Käfer, K.*	*Reichardt, W.*	*Suck, J.-B.* *
Geerk, J.	*Linker, G.*	*Renker, B.*	*Weber, W.*
Gompf, F.	*Meyer, O.*	*Rietschel, H.*	
Haase, E.L.	*Nohl, H.*	*Schmidt, H.*	

Technical Staff

Abel, W. [+]	*Hanak, H.* [+]	*Ratzel, F.*	*Schreiber, H.* [+]
Ehret, G. [+]	*Kraatz, M.*	*Richelsen, H.* [+]	*Smithey, R.*
Ernst, A. [+]	*Kuhn, R.* [+]	*Roller, H.* [+]	*Sobiesiak, H.* [+]
Ewert, D.	*Nadasdy, J.* [+]	*Scheerer, B.*	*Weber, K.*

Visiting Scientists

Hussain, T.; Guest from Bangladesh

Klein, S.; Guest from SFB 127,
       Universität Marburg

Lehner, N.; Guest from Würzburg

Research Students

Conrad, M.; Universität Karlsruhe	*Götz, F.; Universität Heidelberg*
Gauß, C.; Universität Karlsruhe	*Kaufmann, R.; Universität Karlsruhe*
Geibel, C.; Universität Karlsruhe	*Schell, G.; Universität Karlsruhe*
Guth, H.; Universität Karlsruhe	*Pflüger, J.; Universität Karlsruhe*

---

* On leave of absence at ILL, Grenoble

[+] Member of infrastructure